Ph.D. dissertation

Experimental studies on the exfoliation and oxidation behavior of few-layers black phosphorus

Juan Fernando Gómez Pérez

Supervisors:

Dr. Ákos Kukovecz

Dr. Zoltán Kónya

Doctoral School of Environmental Sciences

University of Szeged, Faculty of Science and Informatics,

Department of Applied and Environmental Chemistry

Szeged

2019

Table of contents

List of figures

List of tables

List of abbreviations

ω: Angular frequency

AFM: Atomic Force Microscopy

E_b: Binding energy

K_B: Boltzmann constant

E_{be}: Exciton binding energy

E_f: Fermi energy level

NIR: Near Infrared

UV: Ultra Violet

Vis: Visible

T: Temperature

ϑ: Frequency

h: Planck constant

$\hbar$: Reduced Planck constant

λ: Wavelength

ϕ_B: Potential barrier at heterojunctions

c: Speed of light

2D: two-dimensional

XRD: X-ray diffraction

FET: Field Effect Transistor

TMDC: Transition metal dichalcogenide

MWCNT: Multi-wall carbon nanotube

AsEx: as exfoliated (without centrifugation)

TEM: Transmission Electron Microscope

BP: Black phosphorus

BN: Boron nitride

DMSO: Dimethyl sulfoxide

NMP: N-methyl-2-pyrrolidone

CHP: N-cyclohexyl-2-pyrrolidone

DMF: Dimethyl formamide

I. Introduction

Black phosphorous (BP) is the thermodynamically stable allotrope of phosphorous under ambient conditions. It is a layered material that can be exfoliated into a monolayer two-dimensional (2D) material similar to graphene: phosphorene.

The rediscovery of graphene[1] in 2004 opened a new chapter in condensed matter material science. Although interest in layered materials can be traced back to at least three decades[2,3], 2D materials have commanded the attention of researchers from all over the world most intensively during the last decade. It is interesting that although graphene was reported earlier[4], its stability was uncertain and the acceptance of the scientific community for low dimensional materials arrived only 40 years later[5]. Even today, the industrial exploitation of graphene is limited despite its remarkable electronic and mechanical properties due to various difficulties: the lack of standardization, defect control, and production scalability are among the main issues, because the properties of any 2D material depend strongly on the quality (i.e. the number of layers and defects) of the structure. 2D materials offer new opportunities due to their physical and electronic properties: the possibility to tune their bandgap and their large area to volume ratio are the main examples.

Nowadays, more than 500 types of 2D materials can be found in literature[6], but only three mono-element 2D materials have been demonstrated until now: graphene, silicene, and phosphorene. Other monoelements have been predicted (i.e. stanene or tinene from Sn; borophene from B; and antimonene from Sb) but they have not been fully demonstrated at experimental level[5]. The list of 2D materials keeps growing constantly. For example, a new allotrope (blue) of phosphorus was synthesized[7,8] very recently, only two years after it was predicted by computational studies[9].

Graphene is still the most popular 2D material, followed by metallic or semiconducting dichalcogenides. However, in most of the cases their bandgap tuneability is limited to just a few hundred meV (graphene), or reasonably large modulations (1 to 2 eV) for the case of Transition Metal Dichalcogenides (TMDCs)[10]. Current research in 2D materials focuses on graphene, h-BN and TMDCs (i.e. $MoSe_2$, MoS_2, etc.)[11]. However, the absence of an intrinsic bandgap in graphene and the large bandgaps exhibited by most TMDCs reveal new possibilities for the applications of black phosphorus. Generally, black phosphorus is described as a p-type semiconductor with a bandgap of 0.3 eV in bulk state and approx. 2.2 eV for the isolated monolayer. Therefore, unlike other 2D materials, black phosphorus offers opportunities in the infrared part of the spectra (infrared optical sensors[11]) for samples thicker than approx. 5 nm and opportunities in the visible range (e.g. thin-film solar cells[12]) for few-layers systems. This versatility and operational range have no parallel in other 2D materials.

Since 2014, an increasing interest has been observed for black phosphorus[13–15] as shown in **Figure 1**. This renewed interest has been boosted by approaching the performance limits of the Si-based CMOS technology and realizing the limitations of graphene (i.e. the absence of a well-defined bandgap)[16,17]. Different applications have been evaluated at experimental level, for instance: broadband photoresponse FET transistors[18], hydrogen evolution catalyst[19] and sensors for different analytes: NO_2[20–22], NH_3[23], humidity[24–26], Hg^{2+} [27] and biosensors[28]. In some cases the results have surpassed the figures of merit of graphene or MoS_2[29], reinforcing the status of phosphorene as a promising material.
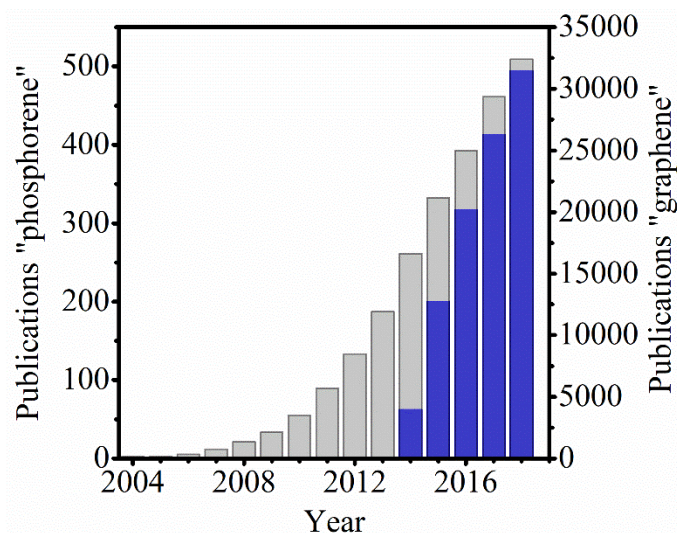
Figure 1. Publications per year for graphene (gray) and phosphorene (blue). Source: ISI Web of Knowledge. Keywords: "graphene" and "phosphorene". Accessed: 14/01/2019

Semiconductors have a long tradition for environmental applications, for instance TiO_2 has proven useful in the photocatalytic degradation of persistent pollutants and disinfection during the last two decades. Currently in the field of 2D materials, van der Waals heterostructures are among the most exciting fields with promising applications in photocatalysis and energy harvesting as they can be tuned for light absorption and enhance the electron-hole stability[30]. Up to date, information on the environmental applications of black phosphorus is still limited, as 80% of the papers published until 2015 were theoretical and issues on stability are yet to be thoroughly addressed.

At present, the number of publications about phosphorene is still very low compared to graphene; however, the annual rate of publications is increasing exponentially as a proof of the interest and technical maturity of the laboratories around the world to work with 2D materials. Unfortunately, black phosphorus suffers of prompt oxidation in comparison with other 2D materials and its stabilization remains unsolved[31]. Recently in the literature, several theoretical papers[32–35] have addressed the oxidation of black phosphorus and the available experimental works encourage bandgap engineering possibilities. Theoretically, black phosphorus passivation is possible with native oxides, but control over the types of oxides

being formed has not been achieved yet, and a better understanding on the oxidation process is required to overcome the hurdles for future applications.

The instability of exfoliated black phosphorus has promoted its functionalization. Functionalized materials take the advantages of dissimilar components to create novel nanostructures[36] and modulate their electronic properties. Additionally, functionalization through different approaches (i.e. covalent, noncovalent, van der Waals heterostructures) has been under research in recent years for the passivation of few-layers BP, but a better understanding of the oxidation processes is required. The signatures of oxidation have been presented in different studies and its effects are not only topographical but electronic as well. The electronic structure modulation caused by oxidation is much larger than the quantum effect confinement, and some groups have theorized on few-layers black phosphorus oxides as a better possibility for future applications[34].

Opportunities for the defects engineering have been pointed out on the basis of computational results. Theoretical works have demonstrated the formation of different types of oxides with interesting properties (e.g. transparent passivation and electronically neutral oxides). Nevertheless, contradictory results on the stability and identification of metastable oxides limit the possibilities for the application of the material.

In this work, I discuss the oxidation of black phosphorus and suggest novel methodologies for the identification of black phosphorus oxides transitions. The results contribute to contemporary literature debates about certain controversies concerning the stability of metastable oxides, the identification of the primary outcome of oxidation and the mechanistic oxidative processes.

II. Theoretical background

II.1 Basic conceptualization

Black phosphorus was first synthesized in 1914 by the Nobel prize winner Percy Williams Bridgman while trying to produce red phosphorus from ordinary white phosphorus at high pressures[37]. In comparison with the other allotropes, the new black phosphorus exhibited a higher density (2.69 g/cm^3) than the white (1.83 g/cm^3) or red (2.05 g/cm^3 – 2.34 g/cm^3) counterparts. Bridgman described the black allotrope as an orthorhombic crystalline structure with oriented flakes stabilized in the AB configuration. Empirically, black phosphorus exhibited higher stability and a fairly good electrical conductivity in contrast with the insulating behavior of the red and white allotropes.

The synthesis process described by Bridgman (1914) requires high levels of pressure and temperature (1.2 GPa and 473 K) that represent a hurdle for the large scale application of black phosphorus. However, recent publications have demonstrated new strategies for the synthesis of the material at lower temperatures, in a vacuum or supported on Ti foils[19,38,39]. The new methods have the potential to reduce production costs, thus representing an important step towards the application of black phosphorus. In order to achieve real-world applications, current efforts are focused on improving the scalability and reproducibility of the synthesis and on gaining better control over the oxidation processes.

Generally, two-dimensional materials (2D materials), quantum wells and superlattices are classified as *thin fims*[5]. This is a purely geometrical definition that requires only the materials's thickness to be between 1 nm and 100 nm[40] However, "real" 2D materials require quantum confinement in the out-of-plane direction, and this condition is usually met only below thicknesses of less than a few nanometres. As a result, 2D materials are interesting not only for geometrical reasons but also because the electron confinement brings a different interaction with electromagnetic radiation than their bulk counterparts.

2D materials can be divided into different groups: semimetals (e.g. graphene and silicene), semiconductors (e.g. phosphorene, transition metal dichalcogenides, transition metal carbides and carbonitrides), and insulators (e.g. hexagonal boron-nitride). But other divisions are also common, for example: black phosphorus as a semiconductor is depicted as a three-fold coordinated crystal in contrast with the four-fold coordinated systems (Si, Ge, diamond, etc.) or the two-fold coordinated (S, Se, Te, etc.)[41].

100 years after the synthesis of black phosphorus by Bridgman (1914), the renaissance of the material in 2014 has been initiated by the possibility of the isolation of monolayers[13,15]. Since then, exfoliated black phosphorus has been categorized as a promising material due to its unique combination of electronic properties. For instance, the work function and electron affinity depend strongly on the exfoliation degree and is possible to find differences higher than 0.5 eV between the monolayer, bilayer and trilayer systems[42].

The electronic structure of exfoliated black phosphorus opens new possibilities to engineer the built-in potentials of heterojunctions for different applications like photodetectors or catalysis (i.e. electron-hole injections), as described by simple mechanistic models in Eq. 1 and Eq. 2.

$$J_{forward} = J_0 \left[exp\left(\frac{eV_T}{k_B T}\right) - 1 \right]$$

Eq. 1

$$J_{reverse} = J_0 \left[exp\left(\frac{-\phi_B}{k_B T}\right) \right]$$

Eq. 2

Here, $J_{forward}$ and $J_{reverse}$ are the current densities in the forward and reverse directions, J_0 is the current density, e is the fundamental charge, ϕ_B is the potential barrier between the metal and the semiconductor, k_B is the Boltzmann constant and T is the absolute temperature.

However, soon it was discovered that exfoliated black phosphorus suffered from prompter oxidation in comparison with other 2D materials[43,44]. As a result, several computational and experimental works were focused on understanding the oxidation process themselves[32,33,45]. The complete understanding is not achieved yet and currently, several groups are working on the passivation and functionalization of few-layers black

phosphorus[45–47] to enhance the stability in environmental conditions. In the following sections, a basic theoretical background is presented to support the characterization results and the selection principles of the characterization techniques utilized during the evaluation of the material.

II.2 Crystalline structure

In the AB stacking configuration, black phosphorus exhibits a symmetry classified as D_{2h} point group and space group Cmce (No. 64). Black phosphorus is present as an orthorhombic C crystalline structure with eight phosphorus atoms in the unit cell. This crystalline structure is preserved from the bulk and down to the monolayer. The lattice parameters according to the supplier (HQ Graphene, The Netherlands) are $a = 0.331$ nm, $b = 1.048$, $c = 0.437$ nm, $\alpha = \beta = \gamma = 90°$ (**Figure 2**). Typically, the P-P bond length is 2.17 Å for the atoms in the zigzag plane and 2.20 Å between the phosphorus atoms linked out-of-plane. The large differences in the lattice constants along the zigzag and the armchair direction give place to a strong in-plane anisotropy that has been predicted as an opportunity of novel electronic devices[36].
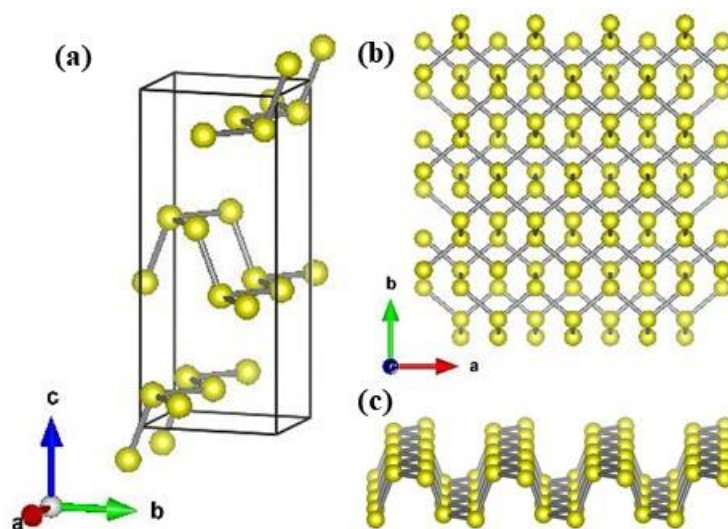
Figure 2. Representation of the crystalline structure of black phosphorus; unit cell (a), top view (b) and monolayer view (c). Drawn in VESTA based on the CIF by Hultgren et al[48].

The interlayer distance in black phosphorous is 0.53 nm as determined from the first diffraction peak in the X-ray diffraction (XRD) pattern corresponding to the (002) plane (**Figure 3**). From an XRD analysis, the *c* lattice parameter is easily calculated by the Bragg equation, however, the preferred orientation of the flakes on the substrate makes it more difficult to measure the other lattice parameters. Thus, in order to analyze the lattice parameters *a* and *b* (oriented in the direction of the *x*-axis and *y*-axis, respectively) it is necessary to measure electron diffraction in a transmission electron microscope (TEM).
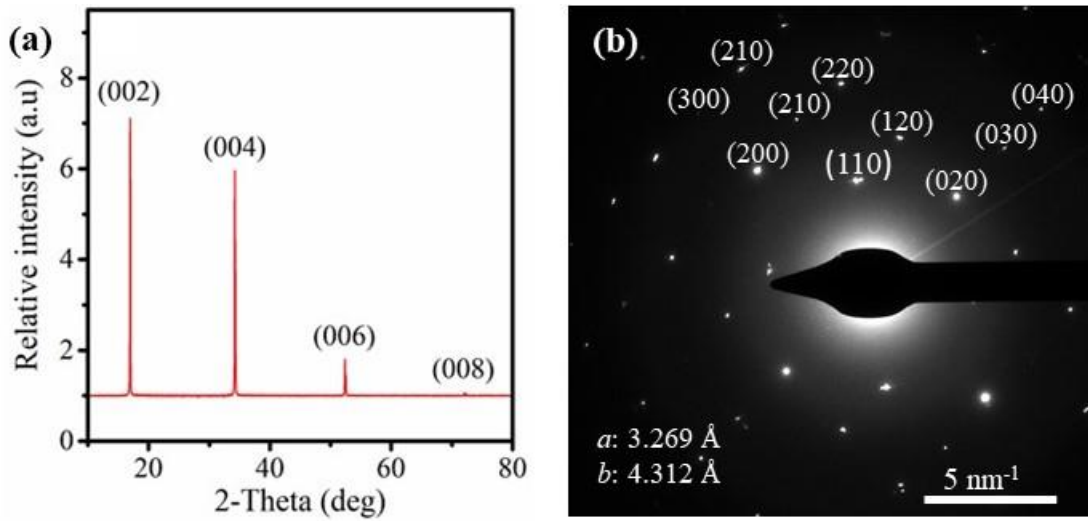
Figure 3. XRD pattern for exfoliated black phosphorus casted on a silicon wafer. CuKα; λ: 1.54 Å. Electron diffraction for exfoliated black phosphorus as measured by TEM.

The lattice thermal expansion of a material is explained by the relationship between the electrostatic potential and the interatomic distance, and the latter is directly related to the modifications of the vibrations at the atomic level. The relationship is described by the Eq. 3.

$$E = \frac{ke^2}{r} + \frac{B}{r^n} + (E_i - E_{ea})$$

Eq. 3

Here *Ei* is the ionization energy, *Ea* is the electron affinity, *n* is the Born exponent, *e* is the fundamental charge, *r* is the interatomic distance and $k = 1/(4\pi E_0) = 9 \times 10^9$ Nm²/C². The lattice vibrations and the electronic structure will be discussed below.

The lattice constants as a function of temperature were calculated for black phosphorus by Villegas et al (2016) (**Figure 4**). The full relaxed calculated constants for the vdW-DF functional are $a = 4.677$ Å, $b = 3.335$ Å and $c = 11.416$ Å, in good agreement with previous results and the calculated values.
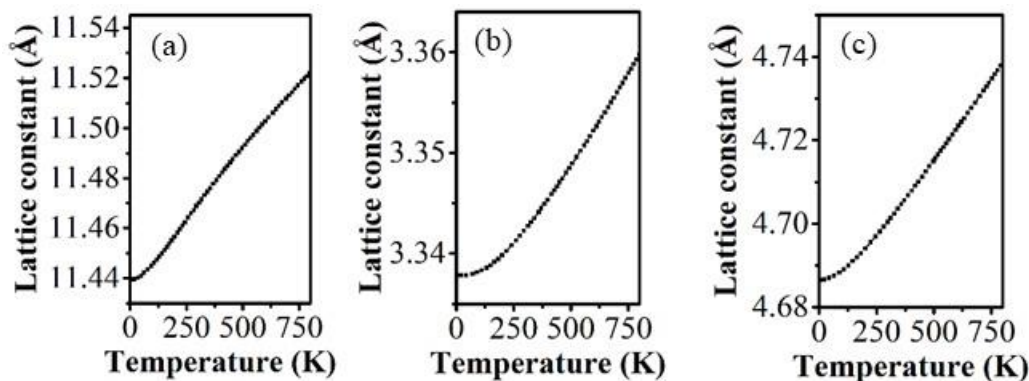
Figure 4. Calculated lattice thermal expansion of black phosphorus. Lattice expansion in the stacking (a), zigzag (b) and armchair (c) directions. Adapted from Villegas et al (2016)[49]

As described by Bridgman (1914) for bulk black phosphorus, the thermal stability of this allotrope is superior to other phosphorus allotropes and it is not ignited in air or under friction[37]. More recently it was found by *in situ* TEM measurements[50] that the exfoliated material start to sublimate at approx. 673 K.

II.3 Lattice vibrations: infrared absorption and Raman scattering

Infrared (IR) absorption and Raman scattering provide fundamental information about the vibrational properties of materials. In typical IR spectroscopy, an infrared photon of suitable energy is absorbed and the target molecule is elevated to an allowed vibrational energy level by the energy of the photon[51]. Raman scattering is caused by the change in the polarizability of a molecule interacting with high intensity light (visible or NIR radiation). While the majority of the molecules will scatter the light elastically (Rayleigh scattering), some are either excited to (Stokes branch) or relaxed from (anti-Stokes branch) a virtual energy level due to the light–matter interaction. The energy of the corresponding vibration is discernible as the difference between that of the elastically scattered photons and the higher (anti-Stokes) or lower (Stokes) energy inelastically scattered ones. The excitation light is

typically a laser source whose wavelength must be balanced carefully between high spectral intensity (proportional with the 4th power of the incident photon energy) and the suppression of undesired fluorescence (more pronounced at higher excitation energies).

Without any external energy supply, the temperature of a material governs the concentration of electrons in the conduction band and holes in the valence band. The higher the temperature, the more intense the vibration of the crystalline structure[52]. Finally, it is important to say that charge carriers (electrons or holes) can change their energy by generating or absorbing phonons[52] and this is a particularly important process for indirect bandgap semiconductors.

In order to describe the vibrational spectra of black phosphorus, the symmetry of the crystalline structure needs to be understood. According to the literature review, BP belongs to the D_{2h} point group[53] and its corresponding phonon dispersion curve is shown in **Figure 5**. Even though six vibrational modes are Raman active according to the selection rules (quadratic functions), only 3 intralayer vibrational modes are visible in commonly used backscattering configurations (red labels). Each vibrational mode can be represented as depicted in **Figure 6**.
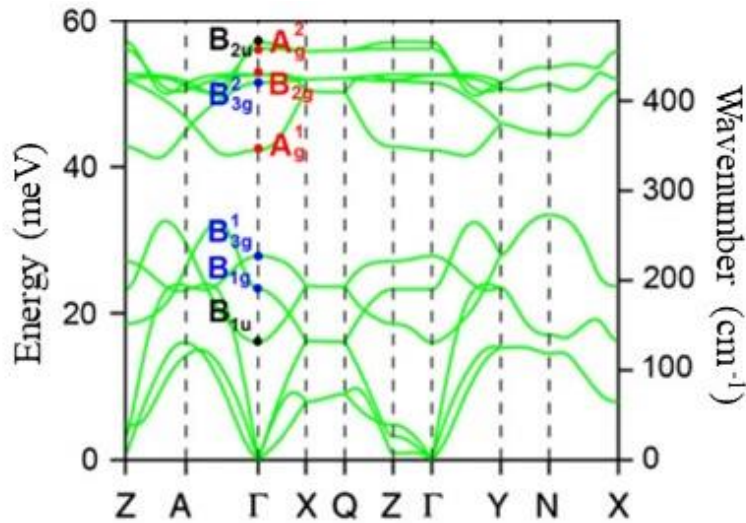
Figure 5. Phonon dispersion curves for black phosphorus. Red and blue are Raman active modes. Black labels are infrared-active modes. Source: Ribeiro et al (2017)[53].

Here, it is important to notice that by tacit agreement, the literature of black phosphorus uses an orientation in which "*the normal of the BP planes is parallel to the y-axis, whereas x and z axes are parallel to the layers*"[31]. This is the reason why is possible to find some disagreements in the notation of some published works. For example, Lee et al (2016) identify the plane (020) with a distance $d_{020} = 5.2$ Å[54], which is most commonly assigned as the plane (002)[55].
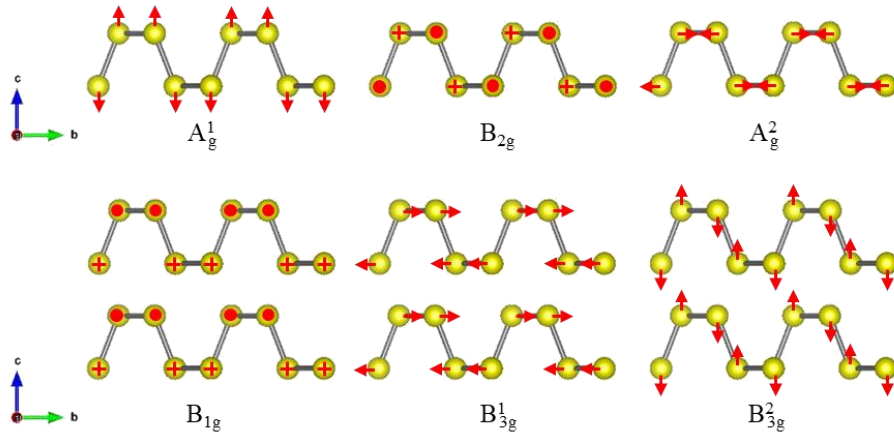
Figure 6. Atom displacements for each Raman active mode.

Besides the intralayer Raman active modes, other bands are visible at lower frequencies but exclusively for multilayer systems and they can be used as an indicator for the exfoliation. These interlayer vibrations at lower wavenumbers are the so-called layer *breathing modes* and they are visible at frequencies below 100 cm^{-1} (**Figure 7**). The breathing modes exhibit shifting depending on the number of layers as proven with samples between 37-layers and bilayers[56,57]. Interestingly, in the bulk phase it is not possible to detect the breathing modes with a Raman spectrometer operated in backscattering configuration because these vibrational modes are not located in the first Brillouin zone.
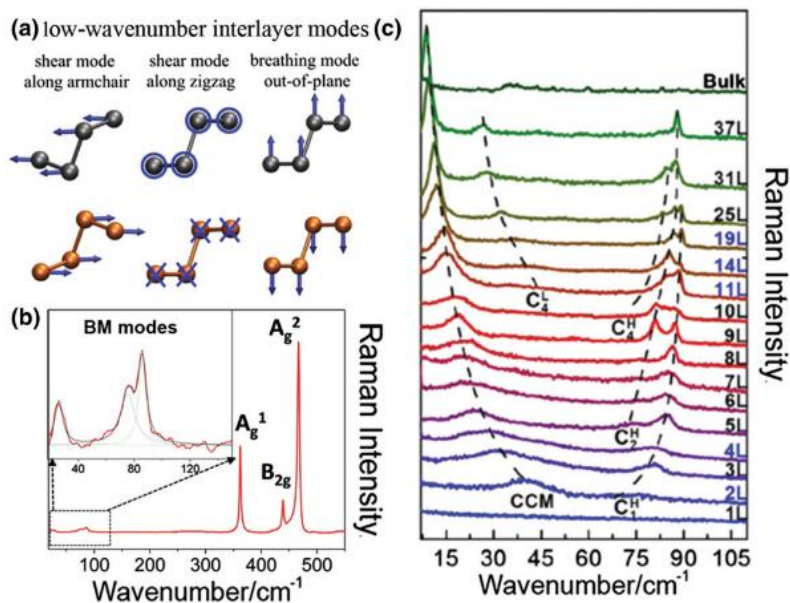
Figure 7. Low-frequency vibrational modes in black phosphorus. Source: Dong et al (2016)[57] and Ribeiro et al (2017)[53]

II.4 Electronic structure

According to quantum mechanics, the energy in semiconducting materials is "quantized" meaning that the electrons' energy is not a continuum but it is allowed only at well-defined levels. In simple terms, every energy level has a density of vacancies and the electrons of the material are placed from lower to higher energy values until all the electrons available in the system are placed in this ordered manner. At a temperature of 0 K the frontier energy level between the occupied and empty states is the so-called *Fermi energy level*. However, when the electrons of the system are allowed to gain energy (i.e. by increasing the temperature or by light irradiation) some electrons are able to occupy higher energy levels than the Fermi level, which explains the conductivity of semiconductors.

In general, materials can be classified as metallic or semiconducting depending on the position of the Fermi energy level within the electronic structure. For semiconductors, it is placed in the so-called *bandgap*, corresponding to a band of forbidden energy levels for the system where electrons cannot be stabilized. The quantization of energy results from the interaction between electrons and the atomic cores, and the bands are formed. Within these

bands, electrons can exchange position but no charge flow is possible unless there is a hole. To generate holes, energy must be added to the electrons in order to reach a different energy band[52]. The highest occupied energy level is at the top of the so-called *valence band*, while the first unoccupied energy level above the Fermi energy level is at the bottom of the so-called *conduction band*.

Black phosphorus is a p-type semiconductor according to the position of the Fermi level in the electronic structure. In this case, the Fermi energy level is closer to the valence band than to the conduction band, and the main charge carriers are the holes. In contrast, graphene behaves like a metal, and the majority of the transition metal dichalcogenides (TMDCs) are either n-type or ambipolar[13]. Black phosphorus, as a p-type semiconductor, represents an exciting new 2D alternative to these materials. The most common method for the determination of the p-type character in black phosphorus is the use of Field Effect Transistors (FET). In a typical experiment, the current-voltage characteristics are measured under the electric fields produced by different back gate voltages[13,58,59].

In one of the earliest computational works for bulk black phosphorus, Takao et al (1981) demonstrated how the electronic structure varies with the environmental parameters. For example, they calculated the pressure dependence of the electronic bandgap ($dE_g/dP = -2.61 \times 10^{-2}$ eV/kbar) using the tight binding approach for bulk black phosphorus, and the prediction was in good agreement with the experimental result (-2.51×10^{-2} eV/kbar)[60]; Similarly, they predicted the temperature dependence only considering the thermal expansion ($dE_g/dT = 6.66 \times 10^{-4}$ eV/deg) and again the result was in good agreement with the experimental values (2.3×10^{-4} eV/deg to 2.8×10^{-4} eV/deg)[60].

More recently, with the increasing interest for 2D materials, several theoretical studies have focused on the electronic structure of the pristine black phosphorus monolayer. Soon after the introduction of black phosphorus to the 2D materials family in 2014, first-principles and *ab initio* calculations predicted the interesting electronic properties of phosphorene even though at that time experimental results were very limited[61,62]. Nevertheless, these theoretical results were accurate enough to predict the *a posteriori* measurements in exfoliated materials

and the fundamental trending relationships between the the number of layers and the electronic structure.

Figure 8 presents an early work by Castellanos-Gómez et al. (2014) that described the electronic structure of exfoliated black phosphorus using DFT calculations[62]. In this figure, the quantization effect on the direct bandgap of monolayers, bilayers, trilayers and bulk BP is depicted and a strong dependence on the number of layers is clearly visible.
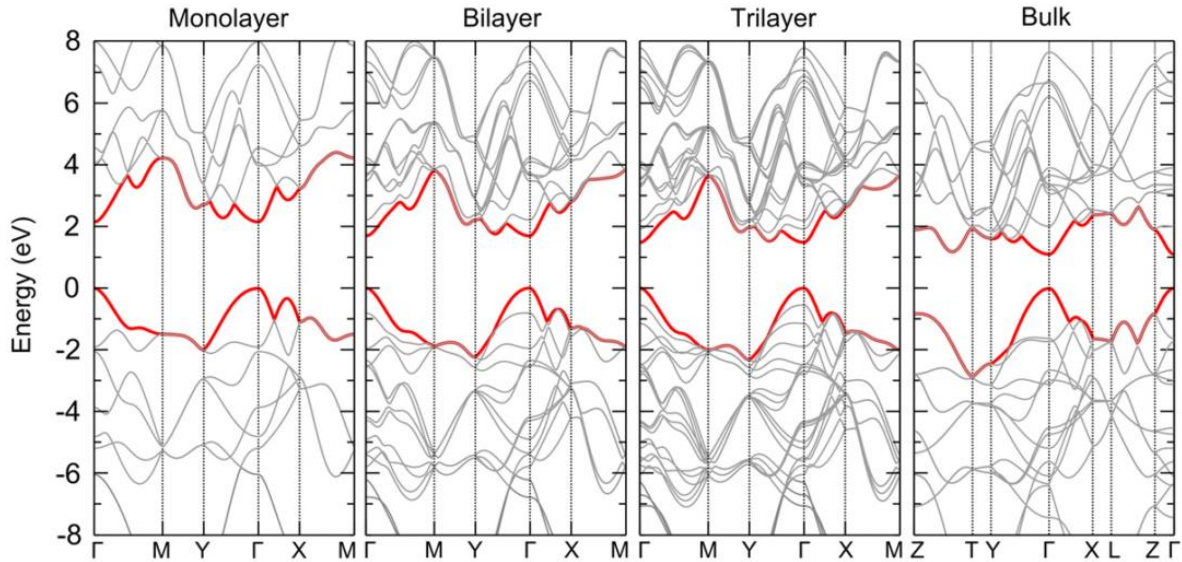
Figure 8. Black phosphorus band structure at all high symmetry points in the Brillouin zone. The energy is scaled with respect to the Fermi energy. Source: Castellanos et al (2014)[62].

The trend shown in **Figure 8** is in excellent agreement with the experimental results. Recently, the large modulation of the electronic structure has been reported by different groups, however, a very comprehensive study reported by Zhang et al (2017) tracked the E_{11} transition (i.e. electronic bandgap) using infrared spectroscopy[63] and recovered the relationship presented in **Table 1**. The results confirm the power law fitting between the number of layers and the electronic bandgap, as expected from theoretical calculations[42,62]. The experimental evidence confirms the computational results and demonstrates the power of the computational studies to predict the electronic properties of exfoliated black phosphorus.

Table 1. Number-of-layers dependence of the bandgap in black phosphorus

Number of layers	Electronic bandgap (eV)	Technique	Ref.
1	~ 2.05	STM, PL	[23,64]
2	~ 1.0	NIR	[63]
3	~ 0.70	NIR	[63]
4	~ 0.60	NIR	[63]
5	~ 0.55	NIR	[63]
6	~ 0.50	NIR	[63]
7	~ 0.45	NIR	[63]
Bulk	~ 0.30	NIR	[63]

Optical bandgaps measured in the laboratory for exfoliated materials are slightly smaller than the theoretical values of the electronic bandgap. One of the reasons to explain the discrepancy is the large *exciton binding energy* (E_{be}) found in black phosphorus[65]. However, the E_{be} is not constant and it can be modified from 0.8 eV down to a few meV by environmental parameters in operating devices[66]. The most generally accepted values for the bandgap of black phosphorus are 0.3 eV for the bulk phase and approx. 2.1 eV for the monolayer. However, for the monolayer is possible to find values calculated or measured between 1.5 eV[42] and up to approx. 2.2 eV[67,68]. Despite the differences, the most interesting agreement between the different studies is the presence of a strong anisotropy and a broad modulation of the electronic structure. This modulation unlocks opportunities for optoelectronics from the near infrared up to the visible range and it has no parallel with another 2D material.

At the experimental level, quantum confinement is yet another important conclusion that tends to be given only minor emphasis in mechanistic considerations. Experimentally, a materal with a thickness of approx. 10 nm exhibits similar properties as its bulk counterpart[31,45,47,69]. This thickness represents a typical value reported for micromechanically exfoliated materials, corresponding to approx. 20 layers. Surprisingly, Woomer et al (2015) reported on micromechanical exfoliation where only 0.06% of a total of 3,538 micromechanically exfoliated flakes were below 5 nm in thickness[65]. The latter indicates that

some of the quantum confinement effects have been overlooked in the currently available literature.

In contrast with the typical indirect bandgaps found for TMDCs, black phosphorus exhibits direct bandgaps from the bulk and down to the monolayer[62,70]. Direct bandgaps are desirable for optoelectronic applications (e.g. light emitting processes or light harvesting) because indirect bandgap materials require both an excitation larger than the gap and a lattice vibration (phonon) for the charge carrier formation and radiative recombination. For other applications, the tunability of the valence and conduction bands is more relevant. For instance, the matching for redox reactions may be improved by engineering of the Schottky barrier or promoting hole injection[42].

Cai et al (2014) reported a more pronounced variation of the valence band than in the conduction band as a result of exfoliation (**Figure 9**)[42]. They highlighted that control over the position of the bands and the type of metal at the contact allows engineering the charge transfer processes in transducer applications. This is relevant in a broad set of applications like catalysis, chemical sensing, light harvesting or batteries as discussed in several recent studies[71–74].
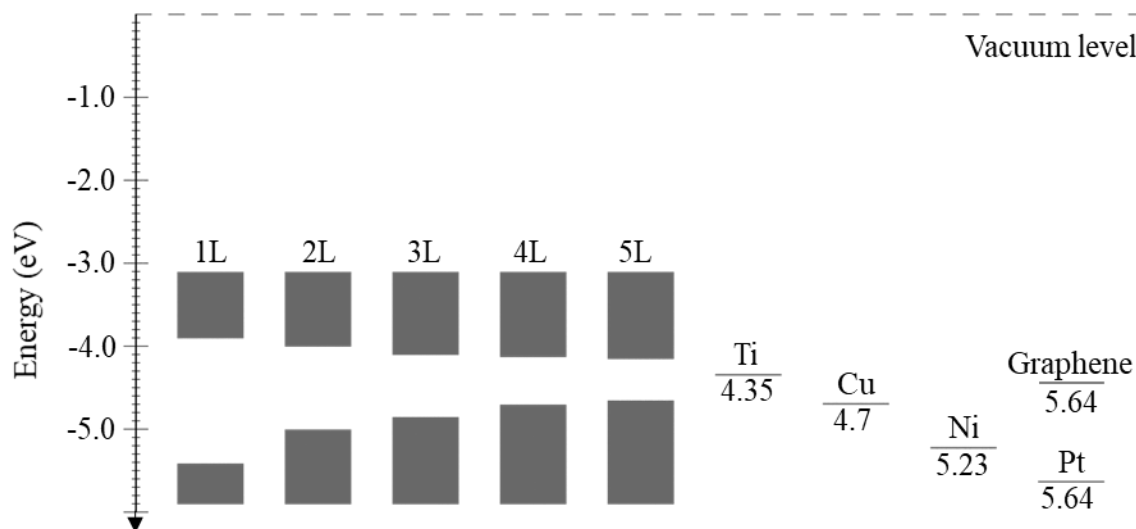
Figure 9. Conduction band minimum and valence band maximum as a function of the number of layers (L) in exfoliated black phosphorus. Adapted from Cai et al (2014)[42]

In FET devices (**Figure 10**), the charge transfer process can be monitored by variations in the potential of the gate and consequently, the electric field passing through the material. For instance, the natural p-doping occurrence of black phosphorus has been proved using FETs[18]. From this set-up it is possible to analyze the type of contact between black phosphorus and a metal, on/off current ratios, and charge-carrier mobility, among others.

Charge carrier mobility is a widely used figure of merit for comparing 2D materials. As a p-type semiconductor, black phosphorus exhibits hole mobilities between $100 - 3,000$ cm^2 V^{-1} s^{-1} [62,68,69], which is higher than in TMDCs but lower than in graphene[10]. This high charge carrier mobility combined with high current on/off ratios (i.e. $I_{ON}/I_{OFF} = 10^2 - 10^5$ [13,68]) explains the growing interest for exfoliated black phosphorus and confirms its position filling the gap in between graphene and TMDCs.
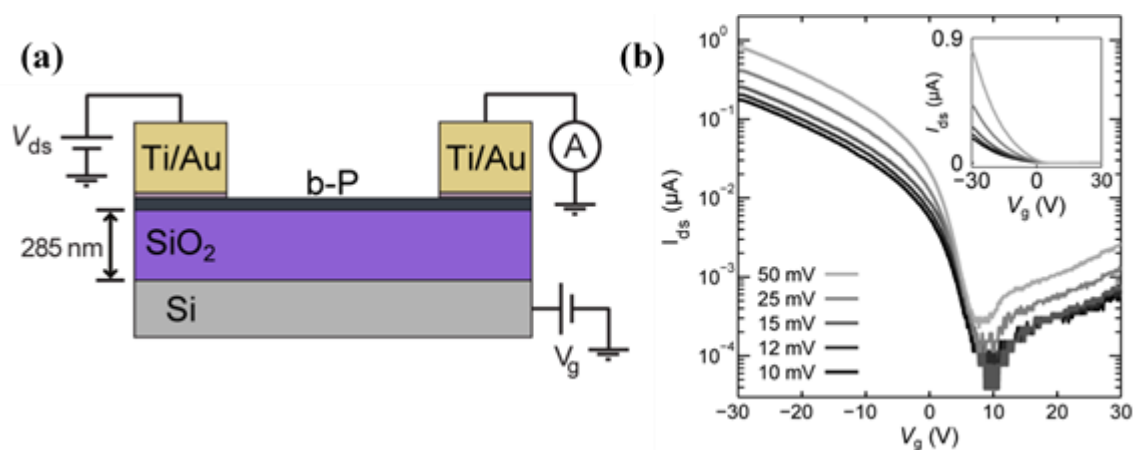
Figure 10. Typical field effect transistor device for the characterization of exfoliated black phosphorus (a). Drain-source currents measured for different drain-source voltages with sweeping gate voltage (-30V to 30V). Source: Bouscema et al (2014)[18]

The evaluation of the figures of merit of black phosphorus in FETs has been useful for the identification of degradation in exfoliated black phosphorus. However, results obtained in different tests should be compared carefully as the quantum confinement is strongly visible between monolayers and up to 4-layers systems. In other words, the comparison between different results should be done using normalization protocols based on oxidation, device configuration, and exfoliation degree. Unfortunately, those normalizing techniques are scarcely discussed in recent studies despite the well-known effect of nanostructure size on

the catalytic activity of nanomaterial-based heterogeneous catalysts. Different results have shown the role of quantum confinement in enhanced selectivity[75], photocatalytic hydrogen evolution, alcohol oxidation and hydrogenation reactions for Pt nanoparticles[76–82].

Optoelectronic devices use the optic and electric properties of semiconductors to tune the relationship between light and electrical current. From the point of view of optoelectronics, metals are good electrical conductors (i.e. allow the motion of electrons) but they "*do not allow light to travel inside*"[52], glasses can accommodate light but are electrical insulators, and semiconductors are able to carry electricity upon light absorption with energy at least as large as the bandgap (Eq. 4),

$$E_{photon} = \frac{hc}{\lambda} = h\vartheta = \hbar\omega \qquad \qquad \text{Eq. 4}$$

where ϑ is frequency, $\omega = 2\pi\vartheta$ is angular frequency, $\hbar = h/2\pi$ is the reduced Planck constant and c is the speed of light.

Beyond the obvious application of these type of devices (e.g. photodetectors) in electronics, the analysis of the photoresponse effect contributes to the understanding of the electron-hole generation process, which is of interest for environmental science in the photocatalytic and electrochemical conversion of pollutants[83]. Photoresponse, as well as photocatalytic processes, are governed by the generation, transport, and recombination of the charge carriers in the structure. Although different mechanisms have been proposed for semiconductors acting as active sensing materials according to their main charge carrier[84], the recombination of the photoexcited electrons and holes is a common problem[85].

II.5 Few-layers black phosphorus oxidation and functionalization

Black phosphorus is easier to oxidize than other 2D materials[43,44]. The energy barrier for the formation of the transition state during the oxidation of phosphorene has been calculated to be the lowest (i.e. 0.1-0.5 eV [32,86]) in comparison with other 2D materials (for instance: graphene (2.2-2.7 eV [87]), MoS_2 (1.6 eV [88]) or h-BN (1.2-2.6 eV [89])). This condition will be a hurdle for the industrial application of black phosphorus unless a deeper understanding of the oxidation of 2D materials and control of the process is achieved[34,90–93].

The main motivation for this type of studies is to avoid the current path of graphene, for which the quality (e.g. defects) and standardization issues have emerged as barriers for industrial application. Currently, several research groups around the world are working on the passivation and functionalization of black phosphorus with promising results [33,67,94,95].

Theoretical and experimental studies agree that degradation slows down when the materials are kept in dark[32,45]. Favron et al (2015)[45], in one of the leading works of the field, demonstrated the influence of ambient parameters (i.e. oxygen concentration, light, and quantum confinement) and explained their results with the Marcus-Gerischer theory (Eq. 5). According to their model, light produces photoexcited electrons in the conduction band, and later the electrons are transferred to the physisorbed oxygen[45,70].

Even though the quantum confinement effect on the oxidation processes has been confirmed experimentally by different groups[45,47,62], it is not usually characterized in theoretical studies as those tend to focus on pristine monolayers. Up to date, computational studies have addressed mainly the oxidation processes of black phosphorus monolayers, while experimentally, 10 nm (~20 layers) has been detected as the limit for the presence of a quantum confinement effect [31,45,47,69].

$$\frac{d\theta}{dt} \propto -\theta \cdot J_{ph} \cdot [O_2] \cdot \exp\left[\frac{\left(\left|E_{g,n}\right|/2 + E_i - E_{F,redox}^0 - \lambda\right)}{4K_BT\lambda}\right] \qquad \text{Eq. 5}$$

Here, J_{ph} is the laser flux, $[O_2]$ is oxygen concentration, E_i is the intrinsic Fermi level, $E_{g,n}$ is the electronic bandgap for n-layers black phosphorus, $E_{F,redox}^0$ is the energy level of the oxygen acceptor state and λ is the renormalization energy of oxygen in water.

In computational works a variety of metastable oxides has been predicted and different types of oxygen bonds were suggested (**Figure 11**), as follows: *dangling oxygen*, when the oxygen atom is chemically bonded on the surface to one single phosphorus atom; *oxygen bridge*, when the oxygen atom is chemically bonded to two consecutive phosphorus atoms on the zigzag ridge, and *interstitial oxygen* when the oxygen atom penetrates the lattice.
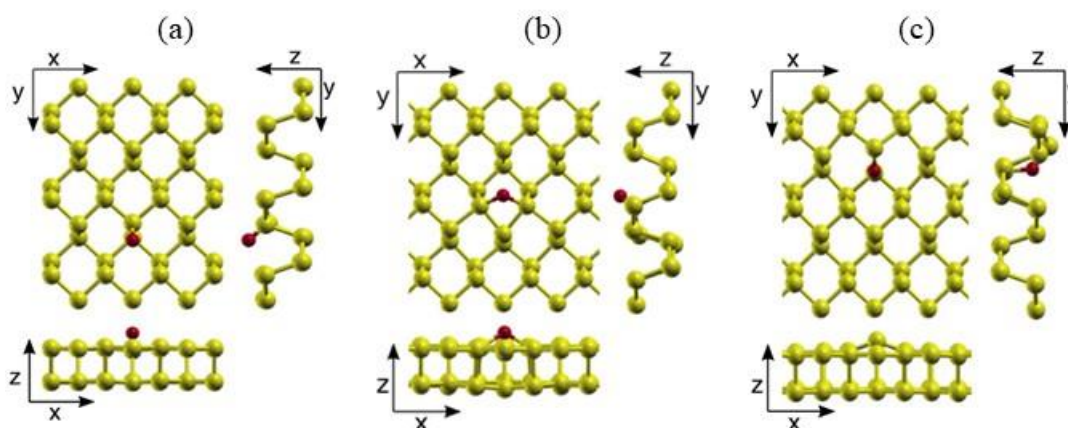
Figure 11. Preferred oxygen (red sphere) positions in black phosphorus oxides: dangling oxygen (a), oxygen bridge (b) and interstitial oxygen (c). Adapted from Ziletti et al (2015)[32]

Ziletti et al (2015) have uncovered in a very comprehensive series of publications[32–34] that the different oxygen bonding positions give rise to different types of oxides: *surface oxides* that correspond to dangling and oxygen bridges, and *planar oxides* that include interstitial oxygen bonds. Another possible oxide type is the *tubular form* which is supposed to have the same enthalpy of formation as the planar forms, however, there is no experimental evidence of its existence in current literature. Regarding the stability of the different types of oxides, Ziletti et al (2015) state *"we can argue than in near-equilibrium conditions the surface forms s-P₄O₂ and s-P₄O₄ will not be the primary outcome of phosphorene oxidation contrary to what has been recently proposed"* in reference to the computational works of Wang et al (2015)[86] and Dai et al (2014)[96], but also from another more recent report of Wang et al (2017)[35].

Large differences are expected for the different types of oxides. As a result, one of the most interesting predictions is the possibility of tuning the bandgap of black phosphorus by controlled oxidation. If successful, it would be possible to produce electronic bandgaps that are truly transparent using planar native oxides (**Figure 12**), and these oxidized layers could protect the underlying layers, keeping the electronic properties of pristine materials. It has been predicted that surface oxides are electronically neutral oxides, meaning that they induce only small transformations of the electronic structure. Therefore, the control and

identification of the different types of oxides are a requisite for bandgap engineering by oxidation.
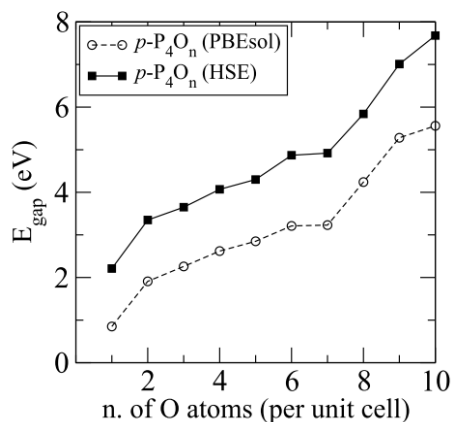
Figure 12. Electronic bandgap energy for planar oxides p-P_4O_n as a function number of oxygen atoms per unit cell. Adapted from Ziletti et al (2015)[34]

From this point of view, the knowledge on the oxidation of exfoliated black phosphorus is closely related with functionalization or doping, as it can expand the limits of the material and create novel nanostructures with integrated properties[36]. For the case of functionalization, the reactivity of black phosphorus becomes an opportunity. A couple of examples are available as the spontaneous reaction for the functionalization with aryl diazonium groups[67], and the lower diffusion barriers for lithium (0.09 eV in the zigzag direction) and sodium (0.04 eV) in comparison with graphene (0.32 eV for Li), silicene (0.20 eV for Li) or MoS_2 (0.28 eV for Na) for application as an anode material in rechargeable batteries[74].

Generally, the functionalization of nanomaterials is achieved by chemical bonding (covalent functionalization) or physical contacts (mixing), and the experience collected with graphene is utilized in the functionalization of phosphorene. Functionalization enables the tailoring of optical and electronic properties[67], and plenty of examples for the functionalization of graphene are available in the literature. For instance, few-layers graphene has been functionalized to improve its electrochemical properties or selectivity towards

glucose and ascorbic acid with Pd nanoparticles (∼30 nm) or capping agents of ionic liquids (BMP–TFSI or BMP–DCA. **Figure 13**), respectively [97,98].

BMP–TFSI   BMP–DCA
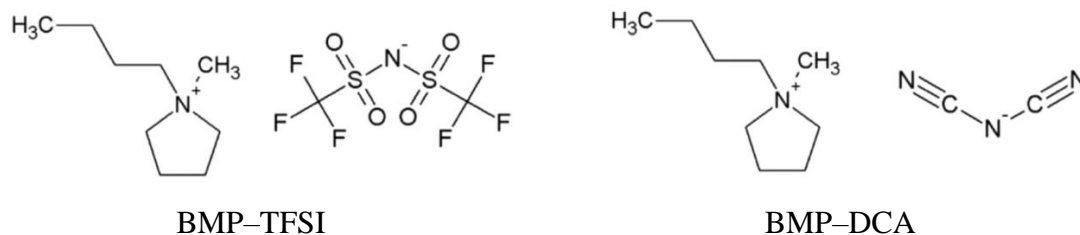
Figure 13. Ionic solvents utilized for enhancing selectivity towards glucose and ascorbic acid. Source: Wang et al (2017)[97]

Enhancing selectivity using ionic liquid coatings in graphene was studied by Kamath and Baker (2012), and according to their predictions, the use of ionic liquids during the exfoliation of graphene produced self-oriented arrays where the cation from the ionic solvent is preferentially adsorbed on the few-layers graphene and the anion is the sensitive part of the target molecules[98].

In the case of heterojunctions, plenty of examples are available in the literature. For instance, the addition of platinum nanoparticles has enhanced the H_2 gas sensing response of WO_3 nanowires[99], the photocatalytic activity of few-layers black phosphorus[29], and the photoresponse of mesoporous nickel oxide[82]. This type of functionalization improves the performance of the device via chemical and electronic sensitization through the electronic band structure modification and/or chemical interactions with the surrounding molecules.

While black phosphorus offers interesting electronic properties, it degrades rapidly in ambient conditions[100]. Functionalization has been proposed to suppress the chemical degradation of exfoliated black phosphorus, but it also modifies the electronic structure of the material. For instance, aryl diazonium substituents have improved the hole mobility and improved the physical stability after ambient exposure, according to topographical AFM measurements[67]. These results suggest that molecules with dangling bonds can directly bond with the exfoliated flakes. In the following sections, a discussion on the signatures of

oxidation and the current studies of functionalization against ambient degradation will be presented.

II.5.1 Signatures of oxidation in exfoliated black phosphorus

Certainly, the means to detect the oxidation have improved with time. Earlier, simple qualitative methods were employed to assess the stability of the exfoliated materials. The most common was the 'bubbles formation' as an indication of oxidation[33,45] by the modification of the natural hydrophobicity of black phosphorus.

A collection of recent studies on the oxidation of black phosphorus is presented in **Table 3**. The effects of oxidation on the exfoliated black phosphorus have been addressed by different strategies. Some of these strategies have been adopted by multiple groups, like for example, the use of the A_g^1/A_g^2 intensity ratio of the Raman-active vibrational modes[45]. However, the precise value of the ratio as a measure of oxidation is blurred and different numbers are found in the literature. Nevertheless, there is a common that the A_g^1/A_g^2 ratio can become a reliable indicator of oxidation over time.

Raman spectroscopy is one of the most popular techniques for the evaluation of exfoliated black phosphorus, but up to date, the results for the Raman response show contradictions[93]. The contradictions may arise from the absence of a formal mechanistic explanation behind the selection of this indicator (A_g^1/A_g^2 ratio), and as a consequence, it is an open question if the trend is caused by physical or chemical sorption, variations in temperature, or simply instrumental parameters like focus size, orientation, laser intensity or wavelength.

X-ray Photoelectron Spectroscopy (XPS) is probably the first option to evaluate the oxidation of the exfoliated materials, however, the precise identification of the phosphorene oxide types has not been achieved yet: Kuntz et al (2017) proposed that the binding energy for the P=O is approx. 131.5 eV[101], but Edmonds et al (2015) assigned the same binding energy to the O-P=O present in planar oxides[33]. The practical implications of their studies are also contradictory. While Edmonds et al (2015) predicted the stability of a passivating layer with native oxides, Kuntz et al (2017) suggest that the by-products of the oxidation

catalyze the degradation, and they have explicitly highlighted the difficulty to design a self-passivating oxide[101].

Similarly, it is not just the experimental identification that is lacking, but the primary product of the oxidation is also unclear. The answer is not trivial, particularly when considering that defects engineering[33,34,102] will be mandatory for any real world applications. One of the most promising applications of black phosphorus is in optoelectronics and the differences in the electronic bandgap are large (see **Table 2**) for surface and planar oxides as demonstrated by Ziletti et al (2015).

Table 2. Bandgap energy calculated with HSE as a function of the number of oxygen atoms per unit cell. Adapted from Ziletti et al (2015)[34]

Type of oxide	Number of oxygen atoms per unit cell	Bandgap (eV)
Surface	2	~ 2.5
	4	~ 2.3
Planar	2	~ 3.4
	4	~ 4.1

Recently, increased surface roughness was suggested to be related with degradation[47,59,67]. and improved AFM techniques are able to determine the phase contrast and lower dielectric constants due to oxidation[103]. However, such studies tend to use micromechanically exfoliated materials with thicknesses larger than 10 nm, and therefore, their results generally do not consider the quantum confinement effect adequately (**Figure 14**).
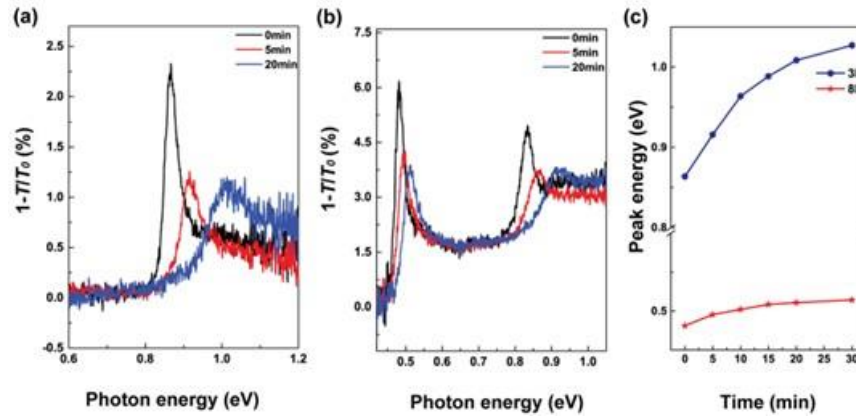
Figure 14. Comparison between a 3-layer and 8-layer black phosphorus as a function of air exposure time. E_{11} transitions for a 3-layer flake after air exposure (a) E_{11} and E_{22} transitions for an 8-layer flake after air exposure (b) and comparison of the E_{11} transitions for a 3-layer and 8-layer flake as a function of time (c). Source: Wang et al (2019)[93]

The effects of oxidation for practical purposes have been reported during the characterization of black phosphorus in FETs. Depending on the device configurations and quantization, the reported charge-carrier mobility for pristine exfoliated black phosphorus ranges between 100 and 3,000 $cm^2\,V^{-1}\,s^{-1}$ [62,68,69]. On the other hand, charge-carrier mobilities between 35 and 40 $cm^2\,V\,s^{-1}$ were reported for oxidized samples [59,62]. Another characteristic behavior is the loss of conductance[47] and the loss of the I_{ON}/I_{OFF} ratio (pristine materials reach values up to 10^5 [13,68], but after oxidation, it is reduced to 600 [62]). However, other studies have shown p-type doping in the material after oxidation, characterized by a higher hole mobility[58], or ambipolar behavior for samples exposed to air[47,62] but also after passivation with h-BN[58,69], surface doping[104], or heterostructures engineering[68].

Another signature of oxidation is provided by photoluminescence (PL). From these experiments, a decay in intensity[69,102,105] was reported that can be related with modifications of the electronic structure. More interestingly, Cao et al (2015) reported that prior to the intensity decay, there was a marked appearance of luminescence during the first stages of oxidation[69]. Similarly, Kang et al (2016) reported the decay of the PL at 908 nm and an increase at 780 nm[105], that could be attributed to a modification of the electronic structure and a band opening that allows radiative recombination at higher energy levels.

Table 3. Resume of studies on oxidation and functionalization of few-layers black phosphorus

Signature of oxidation	Coating		Time of evaluation	Characterization technique	Ref.
	Type	**Thickness**			
Exponential decay of intensity of all Raman vibrations. $A_g^1/A_g^2 > 0.5$ indicates oxidation	Parylene C	300 nm	80 min	Raman spectroscopy	45
Volume increase over time, together with decreased conductance	---	---	---	AFM, FET devices	47
Raman A_g^1/A_g^2 ratio decays	Ionic liquid: BMIM BF$_4$	---	45 days	Raman spectroscopy	31
Photoluminescence appearance and decay	h-BN	1-layer / 2-layer	3 months	PL, FET devices	69
Roughness increment; P=O, P—O stretching modes. p-type doping (atmosph. adsorbates), lower I_{ON}/I_{OFF} ratio	AlO$_x$	~30 nm	14 days	FTIR, AFM, FET devices	59
Smaller dielectric constants Phase spectral contrast (~7.5 µm)	Al$_2$O$_3$	5 nm	---	Infrared (s-SNOM)	103
Photoluminescence intensity decay	P$_x$O$_y$ (O$_2$ Plasma) Al$_2$O$_3$+P$_x$O$_y$	~11 nm 5nm + ~11 nm	6 days 30 days	PL	102
Raman intensity decay	Graphene	3-layer graphene	4 days	Raman spectroscopy	106
Raman intensity decay	MoS$_2$	3-Layer MoS$_2$	21 days	Raman spectroscopy	107
40% higher hole mobility (p-type doping), increased surface roughness	Graphene h-BN	1-layer graphene Few-layer h-BN	8 h, 24h	AFM, FET devices	58
Increased surface roughness	Aryl diazonium: 4-NBD, 4-MBD [b]	---	25 days	AFM, XPS, Raman spectroscopy	91

Signature of oxidation	Coating		Time of evaluation	Characterization technique	Ref.
	Type	Thickness			
Optical absorbance decay, XPS bands at 134 eV (P_xO_y)	Titanium sulfonate	TiL_4@BP: 1.4 nm	3 days	HR-XPS, Optical absorbance, AFM	108
Raman A_g^1/A_g^2 ratio decay	Nonconvalent: Perylene diimide (PDI)	3 - 5 nm	6 months	Raman spectroscopy, AFM	46
Photoluminescence decay at ~909 nm and increases at ~780 nm	SDS	---	1 hour	PL	105
Decay of optical absorbance at 465 nm	Triton X-100 in water [c] $C_{14}H_{22}O(C_2H_4O)_n$	---	600 h	Absorbance	109
Raman shift modulation	PMMA coating [a]	---	19 days [d]	Raman mapping	110
Decreases the charge-carrier mobility and the I_{ON}/I_{OFF} ratio	Sulfur	1 wt% S mixed during the BP synthesis	21 days	FET	17

a. The black phosphorus flake was 35 nm thick, therefore negligible quantum confinement effect; b. The sample thickness for exfoliated materials was 7 nm – 15 nm; c. Liquid phase exfoliation; and d. Storage in dark.

II.5.2 Functionalization of few-layers black phosphorus

In this section, a discussion on the functionalization techniques for exfoliated black phosphorus is presented. In most cases, samples were micromechanically exfoliated but some examples from liquid phase exfoliation are also included. Even though different techniques were utilized (covalent functionalization, passivation by plasma treatment, atomic layers deposition, etc.), the main goal for the functionalization was usually to improve the environmental stability of the exfoliated material[94].

In some of the cases, the thickness of the functionalized top layer was not given. This creates difficulties when comparing functionalization performances. For example, Gamage et al (2016) found that in the case of atomic deposited layers of Al_2O_3 on mechanically exfoliated BP, 5 nm thickness of the passivating layer is not enough to protect the flakes from the environmental degradation and phosphate phases were detected[103].

Uk Lee et al (2016) reported on the TiO_2-exfoliated black phosphorus composite for photocatalysis applications. The results showed a general improvement in comparison with the individual TiO_2 or few-layers black phosphorus: the composite exhibited ten-fold higher apparent rate constants for dyes degradation under visible or ultraviolet illumination[29]. Besides the higher photocatalytic efficiency, higher stability of the black phosphorus composite was reported in biomedical and environmental conditions, in contrast with the few-layer black phosphorus that was easily hydrolyzed to PO_4^{3-}.

An illustrative example of covalent functionalization was the spontaneous functionalization with aryl diazonium chemistry, where the functional group induced controllable p-type doping and improved the FET performance (I_{ON}/I_{OFF} ratio and hole-carrier mobility)[91]. These results demonstrate how the reactivity of the exfoliated black phosphorus may be seized to functionalize exfoliated materials. The thermal stability of the aryl diazonium-functionalized material was evaluated by XPS. The sample was heated up to 623 K in N_2 atmosphere (*ex situ*) and the P-C bond (binding energy: ~132.7 eV) was observable up to 513 K[91]. The functionalization was followed by confocal Raman microscopy, where the A_g^1 vibrational mode decreased with increasing functionalization until the total disruption of the black phosphorus lattice.

Abellán et al (2016) proposed the noncovalent functionalization of BP. After the evaluation of prepared solutions of TCNQ and PDI with several solvents, they concluded THF to be the most appropriate solvent for the noncovalent functionalization of BP with TCNQ. The functionalized flakes exhibited lower A_g^1/A_g^2 ratios than those observed in the control experiments (A_g^1/A_g^2 of 0.4 and 0.6 for the functionalized and control, respectively), but the AFM results were discouraging. The results with PDI are promising with average A_g^1/A_g^2 ratios of 0.8 even after 6 months and thermal stability up to 473 K [46]. Unfortunately, the thickness of the samples was approx. 20 nm, therefore, the quantum confinement effect was not considered.

Several cases of BP passivation with vdW heterostructures are found in the literature[58,69,106,107,111]. The basic idea is to use inert 2D materials to encapsulate the unstable BP. For example, h-BN crystals are impermeable to gases and liquids and have been successfully tested for 3 months of air exposure[69]. Besides the enhancement of the environmental stability, the vdW heterostructures of graphene and exfoliated black phosphorus exhibit high specific capacity, rate capability and cycle life useful for sodium-ion batteries[111].

Most of the experimental studies have been developed with mechanically exfoliated materials. Nevertheless, some examples were reported using surfactants[105,109] or evaluating the passivation capabilities of organic solvents or ionic liquids during the liquid phase exfoliation[23,31,112–114]. This approach offers better scalability and a comparison of different solvents was reported by Hanlon et al (2015)[23]. The results demonstrate the solvent effect on the degradation of exfoliated black phosphorus using the empirical model in Eq. 6 [45]. However, the simple extrapolation of the results in **Table 4** is not possible, and a report on THF-treated flakes cites the same degradation rates as those for untreated samples, while NMP-treated samples exhibit higher environmental stability[31].

$$A_t/A_0 = A_{stable} + A_{unstable}\, e^{-t/\tau} \qquad\qquad \text{Eq. 6}$$

Here, A_t is the relative absorbance at 465nm at time t; A_0 is the relative absorbance at time equals zero; A_{stable} and $A_{unstable}$ represent the absorbance of pristine and

degraded BP nanosheets in suspension, and τ is the observed decay constant of the nanosheets.

Kang et al evaluated different surfactants (SDS, Pluronic F68, and sodium cholate) for the liquid phase exfoliation of black phosphorus, but the XPS results revealed the typical oxidation peaks of black phosphorus[105]. In a similar way, Brent et al evaluated the surfactant Triton X-100 ($C_{14}H_{22}O(C_2H_4O)_n$ where n = 9–10) and reported the formation of a plateau at approx. 500 h during the oxidation process in water[109]. This indicates the formation of a metastable oxide, after which the concentration of PO_4^{3-} by-products was stable until the end of the experiment (800 h) in agreement with other reports[103,109]. Regardless of the oxidation, the addition of surfactants has proven to be useful to enhance the hydrodynamic stability, increase the concentration of exfoliated materials in the suspensions, and extend the observed decay constants of the nanosheets[105,109].

Using another approach, NMP, CHP, THF, and IPA were compared as passivating solvents[31,65]. The conclusion: pyrrolidone-based solvents induce higher environmental stability (BP stability: CHP > NMP > THF, IPA) in exfoliated black phosphorus. In the case of THF, the black phosphorus degradation had the same rates as the unprotected samples[31].

Table 4. Kinetic degradation of black phosphorus in different solvents

Solvent	τ [h]	$\dfrac{A_{unstable}}{(A_{stable} + A_{unstable})}$	Ref
Water[a]	~1	---	45
CHP (glovebox)	300	0.1	23
CHP	190	0.26	23
NMP	275	0.28	23
IPA	115	0.5	23
NaC-H_2O	88	1	23
NMP+Titanium sulfonate	---	0.05[b]	108
1% w/v aqueous Triton X-100	494	0.8	109

[a] Mechanically exfoliated and cleaved sample submerged in deionized water. [b] Result after 72 h.

At the theoretical level, there is an ongoing debate in the contemporary literature on the relative stability of the different types of oxides at near-equilibrium conditions (see **Figure 23**). Somewhat contradictory results have been published regarding the stability

of planar, surface and tubular types of oxides, with works pointing to the higher stability of either the planar[34] or the surface oxide[35,115]. Moreover, the formation of P-O disordered[44] forms and other (e.g. tubular) types of ordered oxides has been predicted but they have not been discussed at the experimental level yet.

In summary, oxygen point defects in few-layers black phosphorus result in electronic structure modifications to an even higher extent than the number-of-layers dependence. At the experimental level, different models have been proposed for the evaluation of oxidation. Most of these models and indicators are developed for the evaluation of functionalization/passivation but lack a fundamental understanding of the oxidation process, as evidenced by the absence of clear limits for the indicators. Additionally, contradictory results have been published on the types of oxides formed under air exposure and the role of these by-products on the passivation. Bandgap engineering and defects engineering have been proposed in theoretical studies as opportunities for the production of novel devices.

III. Aim and scope

My doctoral research was focused on understanding the oxidation processes of few-layers black phosphorus. More specifically, I wanted to contribute to the disputes described in the introduction and theoretical background sections by answering the following questions experimentally.

- What is the topographical effect of replacing high boiling point solvents (NMP) for acetone during the liquid phase exfoliation process?
    - What are the correlations between the topographical and the Raman spectral features?
- How can the oxidation process of few-layers black phosphorus be tracked using Raman spectroscopy?
    - What is the correlation between Raman spectral features and the oxidation of black phosphorus?
    - What is the thermal stability of partially oxidized few-layers black phosphorus?
    - What is the primary outcome of oxidation of few-layers black phosphorus?
- In practical terms, what is the effect of oxidation on the black phosphorus/gold contact typically used in transducer applications?

From the technical point of view, my doctoral work included designing, assembling, testing and operating a new complex measurement set-up for phosphorene research. I coupled a temperature-controlled stage (Linkam, HFS600E) and a source meter (Keithley 2401 or DC supply Keithley 2280) to a confocal Raman microscope (Raman Senterra II, Bruker). The new set up is useful for doing *in situ* Raman spectroscopy under atmosphere–, temperature– and bias– (voltage or current) controlled conditions. I also wrote the code to control each individual system from a single LabVieW surface.

IV. Few-layers black phosphorus: Liquid Phase Exfoliation

IV.1 Introduction

As described in the theoretical background, the limit for the quantum confinement effects in black phosphorus is 10 nm, equivalent to the thickness of approx. 20 layers. From this point onwards and down to the monolayer, an bandgap increase is expected from 0.3 eV up to 2.2 eV[13,23,62]. The trend is well described by a power law, therefore, the most pronounced modulations in the electronic properties are only visible for monolayers, bilayers, and trilayers[42]. The bandgap engineering depends on the exfoliation method, and it is crucial for optical applications, doping and for catalytic or sensing applications. Bandgap engineering through control of the number of layers can be achieved by exfoliation down to the monolayer. Liquid phase exfoliation (LPE) is an interesting method due to its scalability and potential passivation capabilities. Consequently, it is pivotal to improve the knowledge about the solvent – nanomaterials interactions in black phosphorous based systems[116,117].

The exfoliation of 2D materials is possible through several methods. The most common techniques are micromechanical exfoliation and liquid phase exfoliation (**Figure 15**). Woomer et al (2015) analyzed more than 3000 flakes obtained by micromechanical exfoliation and revealed that the yield of flakes with thicknesses lower than 10 nm is extraordinarily low[65]. Their results are verifiable by checking the current literature where the typical thickness values for micromechanically exfoliated materials range between few nanometers to tens of nanometers.

Alternatively, LPE methods followed by centrifugation steps are scalable processes allowing the isolation of few-layers suspensions as a function of the rotational speed. On this regard, it can be said that although micromechanical methods are useful for demonstrative studies[109], the LPE method is more perspectivic from the application point of view.

Some other thickness reduction methods described in the literature are electrochemical exfoliation[118] and laser exfoliation[119]. Electrochemical processes are interesting as they allow the synthesis of black phosphorus from red phosphorus. However, the obtained exfoliated materials exhibit a strong phosphorus pentoxide XPS peak at 134 eV, indicating the presence of the final product of phosphorus degradation. Exfoliation by laser ablation (λ=248 nm) in IPA yielded materials with thickness as low as 7 nm (i.e. the thickness of the reported materials is higher than the expected values with LPE) but no discussion on the oxidation was presented[119].
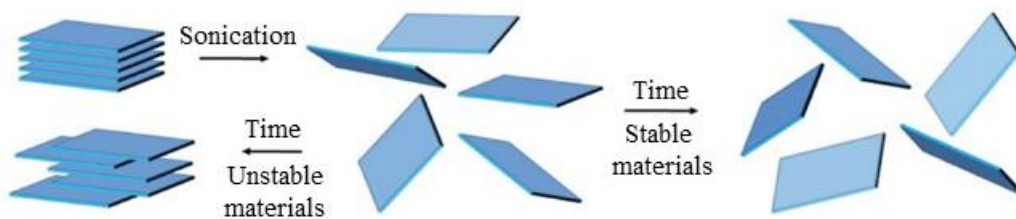
Figure 15. Representation of the Liquid Phase Exfoliation process. Adapted from Nicolosi et al (2013)[120]

The number of layers can determined by different means, with atomic force microscopy (AFM), transmission electron microscopy (TEM) and Raman spectroscopy being the most common techniques. AFM measurements are precise but time-consuming, TEM can be used to check the thickness by simple inspection but is easily biased by the operator, and even though Raman spectroscopy has been used already to evaluate exfoliation processes by measuring the blueshift in the position of the vibrational modes, its applicability for this purpose is still not fully accepted[45,66].

The solvent selection for LPE requires considering several properties such as surface tension, Hildebrand (for nonpolar systems) and Hansen solubility parameters (considering the polar and H-bond interactions)[10]. However, understanding the LPE process is still a challenge as some experimental results are not well explained by the available models[116]. Moreover, besides the solvent's capability for exfoliation, other aspects should also be considered like post-processing, sample characterization and the requirements for the application (e.g. lateral sizes).

For the LPE of black phosphorus in ultrasonication baths, the effect of the dielectric constant is especially interesting as the right solvent can reduce the exciton binding energy (E_{be}) to only a few meV and facilitate the measurement of the electronic bandgap. Woomer et al (2015) described the relationship between the E_{be} and the dielectric constant with the Eq. 7 [65].

$$E_{be} = \frac{-23.79}{\kappa^2 + 15.54\kappa + 14.76} \qquad \text{where } \kappa \text{ is the static dielectric constant.} \qquad \text{Eq. 7}$$

Additionally, several groups have hypothesized on the possibilities of passivation with the solvent during the LPE[23,112], as described in the previous section (see page 28). However, the best passivation results have been achieved by other techniques like vdW heterostructures with h-BN[69], noncovalent functionalization with PDI[46] or passivation with metal oxides[102]. With that said, pyrrolidone functional groups do seem to enhance the ambient stability of exfoliated materials.

Numerous solvents have been tested for the LPE of BP (e.g. CHP[23], DMF[121], DMSO[121], formamide[122]). The most popular one is N-methyl-2-pyrrolidone (NMP) because it yields the highest concentrations[10,112]. The good performance of NMP has been explained by the relatively small difference in surface energy between BP (approx. 60 mNm^{-1} [10,123]) and NMP (approx. 41 mNm^{-1} at 298 K[116]). Nevertheless, other considerations must also be taken into account to evaluate a solvent in LPE processes, for example, the geometrical features of the solvent molecules, the dispersive and polar components of the surface tension[116], and its stability during sonication.

The disadvantages of NMP include poor volatility, water content, wide electromagnetic absorption, by-product formation during sonication, safety issues and postprocessing challenges[105,124]. In fact, Dhanabalan et al. (2017) have stated that "*phosphorene extracted by NMP solution cannot be used directly either in the fabrication of electronic devices or for the optical investigations because its poor volatility*"[10]. Naturally, this problem is also present for other low volatility solvents with high exfoliation efficiencies like N-Cyclohexyl-2-pyrrolidone (CHP)[23].

More recently, Zhang et al (2016)[122] compared several solvents for the exfoliation of black phosphorus and reported zero yields for acetone. However, as demonstrated here, those results are only valid for short sonication periods. At longer sonication periods it is

possible to obtain stabilized BP suspensions with good reproducibility of the particle size and light absorption, and just like in the case of graphene, acetone has certain advantages over other solvents for phosphorene exfoliation[125,126].

Typically, the length of the flakes produced by ultrasonication that are thin enough (i.e. thickness < 10 nm) to exhibit quantum confinement is below 500 nm. Flakes larger than 1 μm tend to consist of many layers, therefore, their investigation is less relevant from the 2D material science point of view, even though some of them may still be considered as thin films. In the case of micromechanical exfoliation it is possible to find examples with lengths in the micrometer scale, but as previously described, the yield is low and the reproducibility is not even considered.

In black phosphorus, it is the flake edges where reactions may start or take place[23,31]. **Table 5** summarizes a literature review on the topographical characteristics of few-layer BP obtained by liquid phase exfoliation. The information in **Table 5** was extracted from Dhanabalan et al (2017)[10] and amended with newer results for the case of ultrasonication and the addition of a new column with the length of the flakes (determined by taking measurements in the published images or extracting the information from the text).

Motivated by the NMP's disadvantages described above, some efforts have been reported in order to exchange the exfoliated BP into other solvents. For example, Guo et al (2015)[127] used saturated NaOH NMP solution and they were able to stabilize BP in water. Li et al (2016) transferred CHP-exfoliated BP into chloroform using centrifugation steps[123], Jiang et al (2015) exchange from NMP to ethanol[128], and Pan et al (2016) made the exfoliation in NMP and then transferred the precipitated flakes (17,000 rpm) into tetrahydrofuran (THF)[129].

In this chapter, the main goal is to obtain few-layers black phosphorus. Additionally, two different aspects are analyzed: *i*) the effects of transferring few-layers BP flakes from NMP suspension to acetone, and *ii*) the applicability of acetone for the direct exfoliation of black phosphorus. These are relevant because acetone stabilizes BP flakes from monolayer and up to 4-layer systems, that is, exactly in the thickness regime where the size-dependent modulation of the electronic properties of black phosphorus (e.g. bandgap, work function, and band positions) is the most pronounced[23,42,65].

Table 5. Topographical characteristics of few-layers black phosphorus produced by LPE methods. Adapted from Dhanabalan et al (2017)[10]: This table has been amended with flake length measurements and new data from recent NMP-based exfoliation reports.

Solvent	Ultra-sonication	Centrifugation	Thickness (nm)	Length (nm)	Ref.
NMP	300W, 4 h	3,000 – 18,000 rpm	0.6 to 10	211.6[b] - 674.3[b]	[127]
NMP	4 h	1,500 rpm, 45 min	3 to 9	< 500	[128]
NMP	200W, 3 h, ice-bath	7,000 rpm, 20 min	1.9 ± 0.9	4.9 ± 1.6	[130]
NMP	90 min	3,000 rpm, 10 min	30 to 60	~ 500	[131]
NMP	300 W, 10 h	1,500 rpm, 10 min	0.6 to 2	< 200	[132]
NMP	-	-	~ 23	~ 700[a]	[133]
NMP	10 h	5,000 rpm, 30 min	0.84 to 4.22	2,000 to 12,000	[111]
NMP	820 W (30%), 24 h, 30 °C	1,500 rpm, 45 min	0.9 to 5	< 200	[134]
NMP	360 W	-	1.71 ± 0.30	1.0 to 2.4	[135]
NMP	300 W, 12 h, Ar atmosphere	7,000 rpm + 15,000 rpm, 20 min	1.5 to 4.5	2.5 to 6.5	[129]
CHP NMP	750 W, 5 h, 2 g L^{-1}	2,000 rpm up to 16,000 rpm, 120 min	9.4 ± 1.3	190 to 620 (2,300)	[23]
Ethanol IPA	400 W, 43 h, RT	4,000 rpm, 60 min	4 to 25	~ 200	[136]
NMP Ethanol	2 h	1,500 rpm, 20 min	5 to 10	100 to 500	[11]
IPA	3 h	1,500 rpm, 20 min	5[a]	~ 2,000[a]	[137]
DMF DMSO	130W, 15 h [10 µg mL^{-1}]final	2,000 rpm, 20 min	0.5 to 40	DMF:190[b] DMSO: 532[b]	[121]
DMF DMSO	12 h	500 rpm, 30 min	26	DMF: 100-150 DMSO: 200-1,200	[26]
Water	8 h, ice-bath	1,500 rpm, 10 min	2	~ 300[a]	[138]
Water	100 W, 30 min	-	< 20	~ 10	[54]

[a] Value derived from the single image shown in the reference. [b] Hydrodynamic size.

IV.2 Experimental

IV.2.1 Production of few-layers BP

Bulk BP crystal was purchased from HQ Graphene (Groningen, the Netherlands) and stored in argon atmosphere. The LPE process was performed in an ultrasonic bath (120 W, 35 kHz) where 4 mg of the bulk BP was added to 10 mL of N-methyl-2-pyrrolidone (NMP, purchased from Molar chemicals) in a glass vial tightly closed with a septum cap and filled with argon. Argon was also bubbled through the NMP before sonication to reduce the dissolved oxygen content. The temperature of the bath was kept constant at 298 K to avoid variations in the surface tension components of the solvent caused by the temperature increment during the ultra-sonication period.

The sonication period in NMP was 1 hour, which is in the lower range in comparison with the values cited in **Table 5**. After sonication, the sample was allowed to settle for 24 h and then the supernatant was collected and centrifuged at 2,000 rpm for 30 minutes. Again the supernatant was collected, flushed with argon and stored for further characterization. This sample was labeled as BP2S. After storing for 7 days at room temperature the sample was centrifuged at 4,000 rpm. The supernatant was labeled as BP4S and the precipitate was suspended using 4 ml of NMP, sonicated for 5 minutes and labeled as BP4P.

IV.2.2 Characterization of the few-layers BP

The selection of acetone as a solvent for LPE was based on preliminary experiments. During the preliminary studies, different solvents (i.e. NMP, acetone, ethanol, and hexane) were tested for the exfoliation of black phosphorus (see **Figure 16**). From the preliminary tests it was detected that for lower sonication periods (i.e. less than 4 hours), the efficiency of exfoliation in the chosen solvents is very low. However, some capability of producing stable suspensions was hinted in acetone, and therefore, it was chosen for evaluation with longer sonication periods (24 hours).
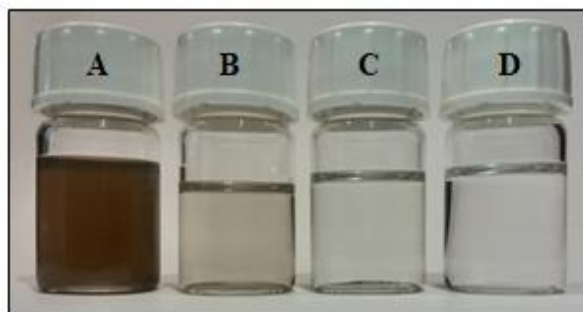
Figure 16. Preliminary evaluation. LPE of black phosphorus in NMP (A), acetone (B), ethanol (C) and hexane (D). Sonication period: 2 hours

The morphology of the few-layers BP was characterized using Atomic Force Microscopy (AFM, SMENA NT-MDT) with a golden silicon probe (NSG30, NT-MDT) in semicontact mode. The sample was drop casted on a mica substrate and dried in vacuum. The thickness and length distributions were determined by measuring 300 individual flakes in 5 images for each sample, in agreement with the methodology utilized by Woomer et al (2015)[65]. Multi-layer black phosphorous was also characterized by powder X-ray diffraction (XRD, Rigaku Miniflex II unit operating with Cu Kα radiation, λ=1.54056 Å).

The quality of the exfoliated materials was examined by transmission electron microscopy (TEM, FEI TECNAI G^2 20 X-Twin) operated at 200 kV accelerating voltage and Raman spectroscopy with a 532 nm wavelength laser with a spectral resolution of 4 cm^{-1} and interferometer resolution of 1.5 cm^{-1} (Bruker Senterra II).

The suspension stability was analyzed using the zeta potentials obtained from Dynamic Light Scattering measurements (DLS, Malvern, Zetasizer-NanoZS) at 633 nm. The electrophoretic mobility was determined, and the zeta potential was calculated using Eq. 8, where ε is the dielectric constant, z is the zeta potential and ɳ is the dynamic viscosity. For this work, we used the Smoluchowsky model assuming the Henry's function $f(ka) = 1.5$.

$$U_E = \frac{2 \, \varepsilon \, z \, f(ka)}{3ɳ} \qquad\qquad \text{Eq. 8}$$

NMP has a dielectric constant of 32.16, refractive index of 1.47 and viscosity of 1.666 mPa s at 25 °C. The utilized BP refractive index of 3.4[139] corresponds to a phosphorene monolayer as calculated from the dielectric constant following the relationship $n^2 = \varepsilon$, where n is the refractive index and ε is the dielectric constant in the direction of the defined plane[140]. Size distributions were calculated from DLS data and reported as hydrodynamic size for comparison with results from other authors, as well as with those obtained in this work from the AFM measurements.

IV.2.3 Solvent transfer

The NMP-exfoliated black phosphorus suspensions were dried in a vacuum chamber for 8 hours without any external source of heating to avoid thermal oxidation. After the NMP evaporation, the vial was refilled with acetone (dielectric constant: 20.7, dynamic viscosity: 0.3111 mPa s, refractive index: 1.356) and vacuum dried once more to remove any NMP residues. Afterwards, the vial was refilled with acetone and bubbled with argon. Finally, the sample was ultrasonicated for 5 minutes and stored ready for characterization.

IV.3 Results and discussion

The zeta potential values of -30 mV, -43 mV and -33 mV corresponding to samples BP2S, BP4S and BP4P, respectively, indicate that all NMP-exfoliated suspensions were stable. Hydrodynamic size distributions obtained by DLS and topographical characterization by semicontact mode AFM are summarised in **Figure 17**.

For the sample BP2S in NMP, the average hydrodynamic size was 180 nm (Z-average, according to DLS measurements) while the peak for distribution by number was at 130 ± 50 nm (**Figure 17a**). After centrifugation at 4,000 rpm, the average flake hydrodynamic size in the supernatant (BP4S NMP) decreased to 90 ± 40 nm, and that of re-suspended precipitate (BP4P NMP) increased to 160 ± 50 nm. These results are in good agreement with the average sizes measured by semicontact AFM insofar as they feature a similar log-normal distribution (**Figure 17a, d**). The mismatch between the highest intensity peaks is most likely due to the geometry of the flake and the assumption made in the Eq. 8 when using Henry's function (i.e. $f(ka) = 1.5$).
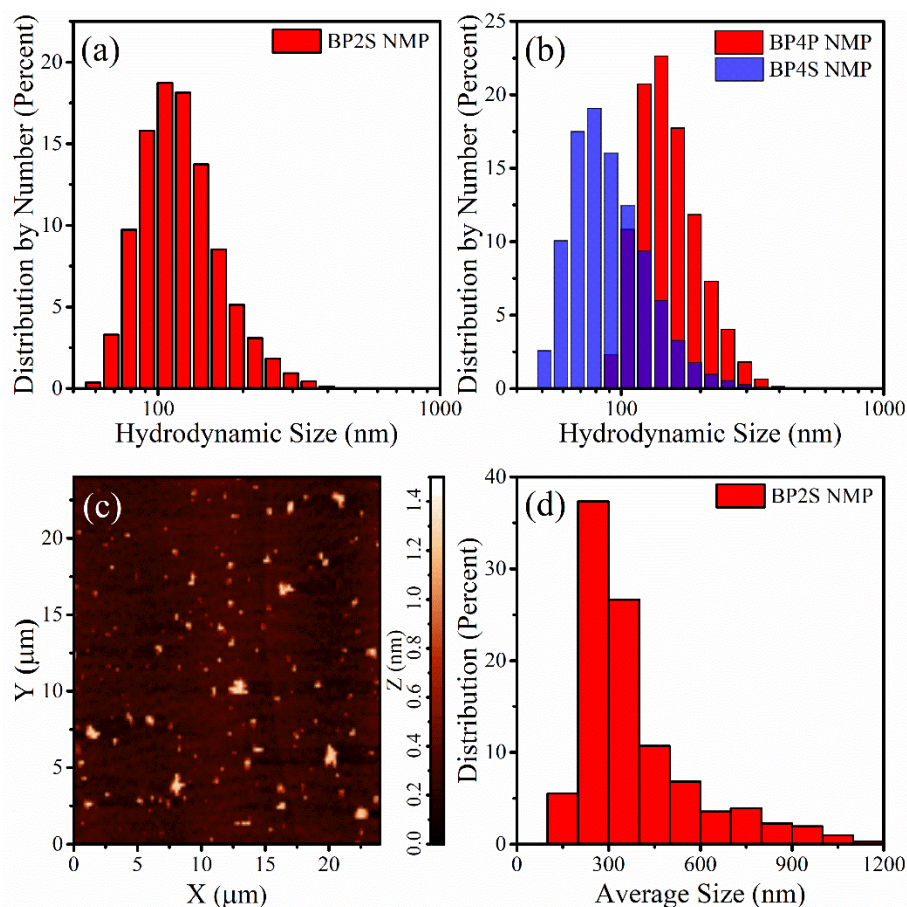
Figure 17. Topographical characterization of few-layer black phosphorus samples produced by liquid phase exfoliation in NMP. Hydrodynamic size distribution as measured by DLS (a). Centrifugation effect on the size distribution (b). Typical AFM image of sample BP2S NMP (c). Average BP flake diameter distribution measured by AFM (d).

The AFM-derived thickness of the flakes produced by LPE and subsequent centrifugation was below 1.5 nm (**Figure 18a-b**). This corresponds to either 3-layer, 2-layer, or monolayer black phosphorus, which are the most interesting systems from the future electronics application point of view[23,42]. Here, it was assumed that peaks below 1.0 nm in the thickness distribution histogram belong to monolayers (theoretical thickness 0.55 nm[10]) considering the error of semicontact mode AFM height measurement, whereas those above 1.0 nm are due to 2-3-layer flakes.

From the AFM measurements, a positive linear correlation between the lateral size of the flakes and their maximum thickness is depicted in **Figure 18c-d**. The comparison between **Figure 18a** and **Figure 18b** indicates that resuspension in acetone shifted the thickness distribution towards thinner BP products. This is explained by the spontaneous segregation that occurred after the NMP-to-acetone solvent exchange: only particles below 500 nm were stabilized in acetone, hence the suspension was enriched in monolayers while the larger particles (mainly bilayers and trilayers) were precipitated.
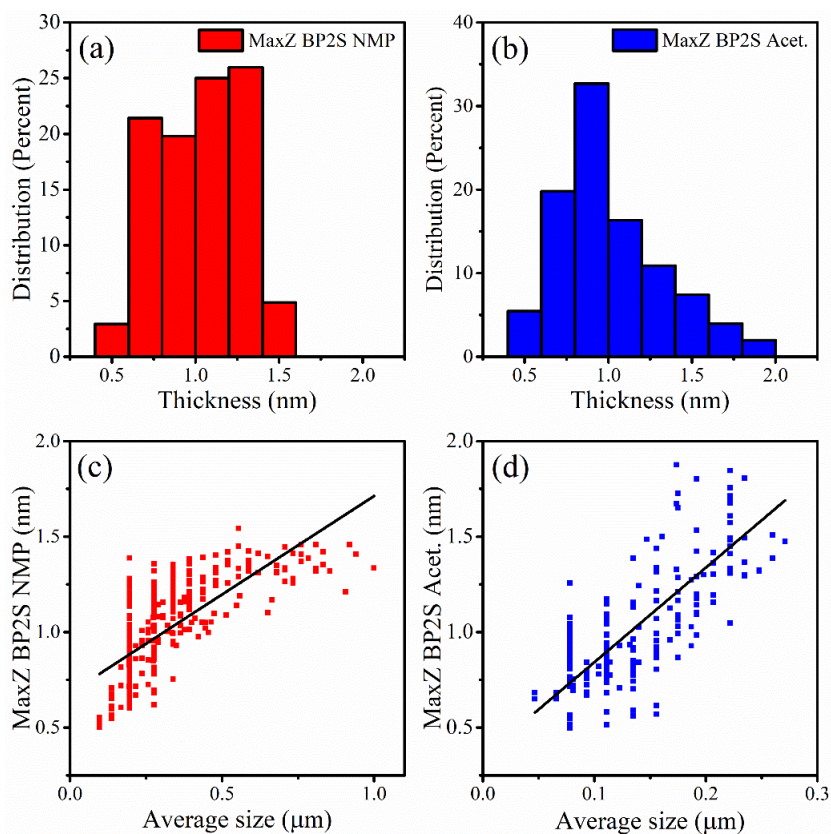
Figure 18. Thickness distribution of the samples BP2S NMP (a) and BP2S Acetone (b). Average size correlation with thickness for the samples BP2S NMP (c) and BP2S Acetone (d). Lines in parts c and d are guides for the eye.

The zeta potential of the flakes resuspended in acetone as described in the experimental section was -29.9 mV (**Figure 19a**). In agreement with the widely accepted ±30 mV zeta potential stability threshold, both the acetone-based and the original NMP-based suspensions

were stable for over 2 weeks at room temperature. The topographical homogeneity improvement effect of acetone was assessed by detailed AFM analysis (**Figure 19b-d**). The average lateral size of monolayers and bilayers in acetone was 100 ± 30 nm and 160 ± 60 nm, respectively. In contrast, the average monolayer in NMP measured 220 ± 70 nm, and the bilayer had an average length of 410 ± 200 nm. While the lateral dimension of flakes stabilized in acetone is a factor of 2 smaller than that of their NMP-suspended counterparts, the size distribution is more tightly controlled in acetone as indicated by the factor of 3 difference in the standard deviation of the flake size.
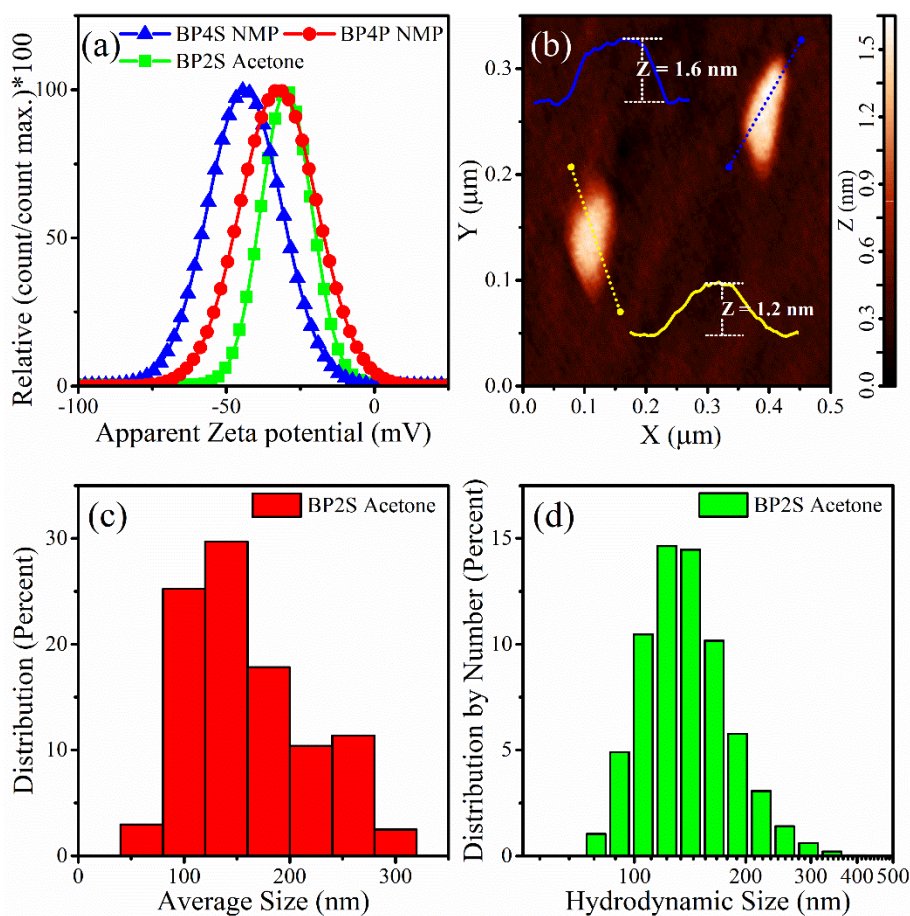
Figure 19. Zeta potential before (BP2S) and after (BP4S) centrifugation (4,000 rpm, 30 min) for the sample in NMP and acetone (a). AFM image from the sample BP2S suspended in acetone, (b) and its corresponding average diameter distribution measured by AFM, (c). Hydrodynamic size distribution for the sample BP2S in acetone (d).

The more uniform size of the acetone-derived few-layers black phosphorus makes it more suitable for separation, for example by centrifugation. Moreover, smaller standard deviations are advantageous e.g. when studying BP chemistry as the reactions may start or run at the edges[23].

To evaluate further the capability of acetone as the solvent for LPE of black phosphorus, the exfoliation was also attempted directly in acetone, using the much longer sonication time of 24 hours (power 120 W; temperature: 298 K). Unlike Zhang et al (2016)[122], we have found it possible to obtain phosphorene flakes by this direct LPE method. The product was very similar to that of the NMP+centrifugation+solvent exchange method described above (BP4S Z-average hydrodynamic size: 96 nm; zeta potential: -38.1 mV). This confirms that the BP flake homogeneity improvement effect is an intrinsic property of using acetone as a solvent.

The effect of acetone in the exfoliation process is most probably due to the considerable mismatch between the surface energy of BP (approx. 60 mNm^{-1} [10,123]) and acetone (23.2 mNm^{-1} at 293 K), which results in the selective stabilization of small flakes and the precipitation of all others. An additional advantage of acetone is that its boiling point (329 K) is significantly lower than that of NMP (475 K), therefore, it facilitates the production of cleaner phosphorene surfaces uncontaminated by remnant solvent molecules and the thermal removal of the residues can be done at significantly lower temperatures.

The optical bandgap was estimated as 2.15 eV from the absorption spectra reported in **Figure 20a** for the acetone-exfoliated sample centrifuged at 4,000 rpm. This matches well both the experimentally measured value for the monolayer (e.g. ~2.1 eV as determined in CHP by Coleman's group[23]) and the theoretical electronic bandgap of 2.15 eV[62]. The agreement between the optical bandgap and the electronic bandgap is explained by the low exciton binding energy that in the case of suspensions in acetone is expected to be only -31.1 meV[65].
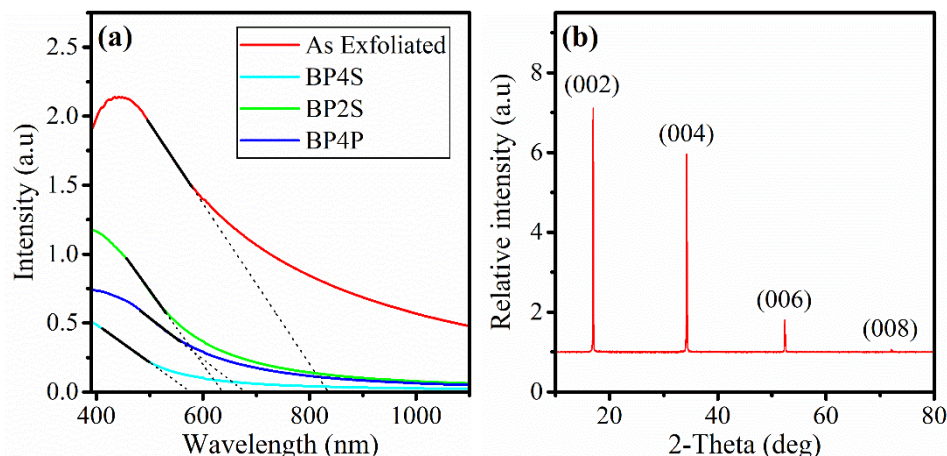
Figure 20. UV-Vis-NIR for black phosphorus (BP) exfoliated in acetone. BP2S: Suspended fraction after centrifugation at 2,000 rpm (30 min). BP4S: Suspended fraction after centrifugation at 4,000 rpm (30 min). BP4P: Precipitated fraction after centrifugation at 4,000 rpm (30 min) (a). XRD pattern for the As Exfoliated materials (b).

The formation of interstitial oxygen bonds results in deformations as large as 90% in comparison with pristine phosphorene[34,141]. Therefore, the stability of the materials exfoliated in acetone was examined in terms of its interplanar spaces. First, according to the XRD pattern (**Figure 20b**), the plane distance calculated from the first and most intense peak is 5.22 Å which corresponds to the size of the monolayer and the lattice constant c = 10.44 Å. This value is in good agreement with the lattice parameters reported previously[142]. In order to examine the other lattice parameters after exfoliation, electron diffraction patterns of several flakes were recorded with a transmission electron microscope (**Figure 21**). The lattice parameters were calculated for the same set of flakes before and after exposure to oxygen (*ex situ*) at 373 K for 20 min, and the results are presented in **Table 6**. The treatment conditions were regulated in a temperature-controlled stage (HFS600E, Linkam).
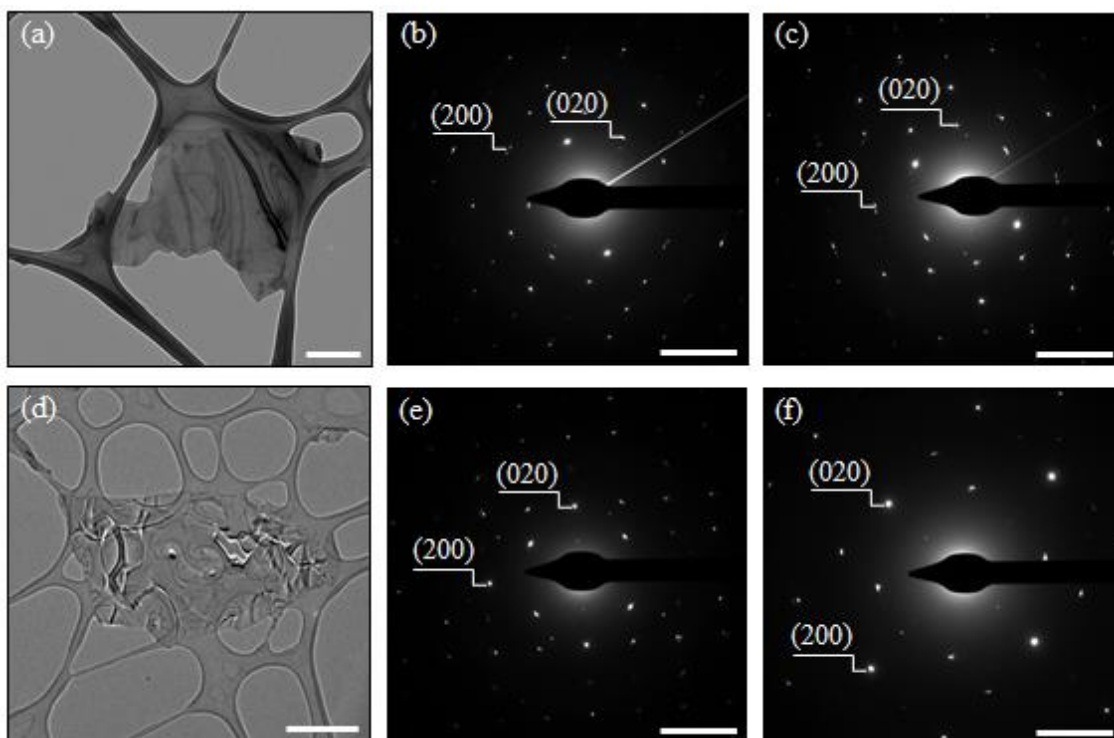
Figure 21. Bright field image of a flake exposed to oxygen flow for 20 min at 373 K. (Bar scale: 500 nm) (a) and its electron diffraction before (Bar scale: 5 nm^{-1}) (b) and after oxygen exposure (Bar scale: 5 nm^{-1}) (c). TEM Image (Bar scale: 1 µm) of a freshly exfoliated BP (d) and its electron diffraction before (Bar scale: 5 nm^{-1}) (e) and after oxygen exposure (Bar scale: 2 nm^{-1}) (f).

The values of the lattice parameters obtained by electron diffraction exhibit variations smaller than 0.05 Å after the oxygen exposure at 373 K (**Table 6**). This indicates the absence of interstitial oxygen bonds at the first stages of oxidation as these types of oxides increase the lattice spacing promoting further oxidation[100,101].

According to some theoretical calculations and XPS measurements[32,33], surface types of oxides are the first to be formed with minimal lattice deformation and their transformation to interstitial oxygen bond requires an activation energy of 0.69 eV[32]. Our results agree with these findings at the lattice level, however, the oxidation process of the exfoliated materials requires further investigation because not only passivation, but also the tuning of the bandgap can be achieved by oxidation.

Additionally, the acetone-exfoliated materials show good thermal stability even after exposure to oxygen flow at 373 K (no defects were observed during TEM examination), allowing thermal pre-treatments of the flakes to remove adsorbed species without inducing undesired degradation processes. Here is important to recall that this is not the case for other types of solvents with higher boiling temperatures as NMP that would require temperatures higher than thermal energy required to start the thermal oxidation of black phosphorus. This will be discussed in the next chapter.

Table 6. Lattice parameters calculated from the electron diffractions in Figure 21

	Lattice parameters (Å)	
	a	*b*
Before treatment	3.29	4.31
After treatment	3.26	4.29

Finally, the acetone-exfoliated materials were examined with *in situ* Raman spectroscopy in a backscattering configuration. The sample was drop casted on a silicon wafer and mounted in the measurement stage. Raman spectra were collected in the temperature range 123.15 K to 423.15 K in argon flow atmosphere and the results are presented in **Figure 22**.
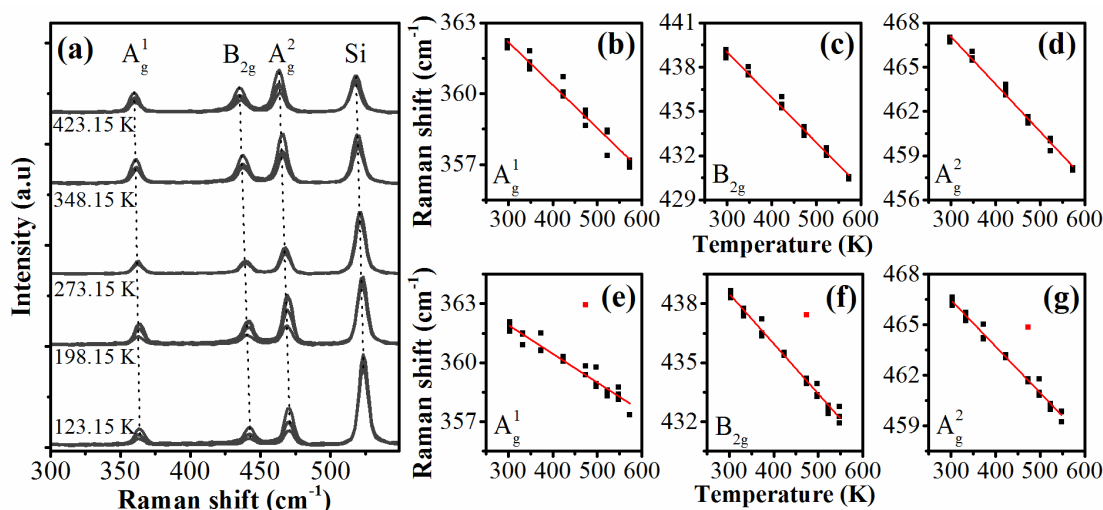
Figure 22. Raman characterization of the acetone-exfoliated materials. Raman spectra at different temperatures for the sample BP4S acetone (a). Raman spectra vs temperature for each vibrational mode for the sample BP4S acetone (b-d) and BP4P acetone (e-g).

Monotonic redshift was observed with increasing temperature for the three vibrational modes (i.e. A_g^1, B_{2g}, and A_g^2) (**Figure 22**), and the linear fitting parameters are shown in **Table 7** for the samples BP4S acetone and BP4P acetone. The slope of the linear fitting is the thermal expansion coefficient, and its values presented here are in the same order of magnitude as those recently reported for mechanically exfoliated samples in a comparable range of temperatures[143,144].

The intercept values shown in **Table 7** are indicators of the quality of the drop-casted materials and the exfoliation process. All three vibrational modes collected from the sample BP4S acetone are blueshifted in comparison with the sample BP4P acetone. Even though random aggregation of the flakes takes place after the drop-casting process, this is a clear evidence that the quantum effects are preserved even after re-aggregation and the vibrational properties are shifted from those of the bulk crystal.

It is worth noting that the results of the thermal characterization for the pristine substrate (i.e. silicon wafer) were -0.0239 cm^{-1} K^{-1} and 527.9 cm^{-1} for the thermal expansion coefficient and the harmonic phonon frequency, respectively. These values are in good agreement with previous reports[145] and validate the methodology for the characterization of the exfoliated materials.

Table 7. Linear fitting parameters for the Raman shift temperature dependence

Sample	Vibrational mode	Slope (cm^{-1}/K)	Intercept (cm^{-1})	R^2
BP4S	A_g^1	-0.01828	367.68	0.96977
	B_{2g}	-0.03056	448.18	0.99173
	A_g^2	-0.03219	476.72	0.99077
BP4P	A_g^1	-0.01464	366.31	0.93909
	B_{2g}	-0.0255	446.16	0.9863
	A_g^2	-0.02752	474.72	0.98645

It appears that the higher surface area to volume ratio of monolayer BP flakes combined with their smaller lateral dimensions allows their stabilization in acetone suspension. Larger bilayer and trilayer particles precipitate spontaneously upon exchanging the solvent to

acetone and can be recovered from the precipitate, if necessary. We suggest that given the relationships between length, thickness and stability reported here, it is possible to fractionate few-layer black phosphorous flakes using an appropriate combination of solvents. This is expected to be useful for optimizing phosphorene flakes for sensoric and catalytic applications, where the position of the valence and conduction bands is as important as the absolute value of the electronic bandgap itself.

IV.4 Conclusion

Liquid phase exfoliation (LPE) is a common technique for the production of 2D materials due to the scalability of the process, but has some disadvantages related to the sorption of the solvent, the oxidation of the sample during storage, and the topographical inhomogeneity of the exfoliated material. N-methyl-2-pyrrolidone (NMP), the most often used solvent for the exfoliation of black phosphorus (BP), has some additional drawbacks like the formation of by-products during sonication and poor solvent volatility.

Few-layers black phosphorus (BP) suspension produced by liquid phase exfoliation in NMP is stable for over two weeks at room temperature with absolute values of zeta potential larger than 30 mV. The produced material shows a positive correlation between flake length and thickness that can be exploited for phosphorene fractionation considering the lower stability of larger flakes. BP flakes exfoliated in NMP can be transferred into acetone. This brings about two important advantages: *i*) it improves the topographical homogeneity of the phosphorene flakes, and *ii*) it facilitates solvent removal without the need for excess heating that could induce BP oxidation. The latter property appears to be particularly useful for phosphorene-based sensor application development. In contrast to available literature wisdom, we were also able to exfoliate black phosphorous directly in acetone by 24-hour sonication. Improved flake uniformity (as compared to NMP) was also observed here, which confirmed that the topographical homogeneity enhancement is an intrinsic property of the acetone – black phosphorous system.

The acetone-exfoliated materials show good stability in suspension and after oxygen exposure in a controlled atmosphere, according to the DLS and TEM measurements. The

thermal expansion coefficients of the BP4S acetone drop-casted sample in the 123.15 K to 423.15 K temperature range were -0.01828 cm^{-1}/K, -0.03056 cm^{-1}/K and -0.03219 cm^{-1}/K for the A_g^1, B_{2g} and A_g^2 vibrational modes, respectively. We suggest that the quantitative value of the thermal expansion coefficient could be used to assess the quality of exfoliated black phosphorous samples.

IV.5 Authorship declaration

This chapter contains published work. No part of this work has been submitted for any other degree or diploma. The published information can be found under the following reference:

J. Gómez-Pérez, Z. Kónya, and Á. Kukovecz, "Acetone improves the topographical homogeneity of liquid phase exfoliated few-layer black phosphorus flakes," *Nanotechnology*, vol. 29, no. 365303, pp. 0–15, 2018.

V. Tracking the oxidation of Black phosphorus in the few-layers regime

V.1 Introduction

Quickly reciting the interesting properties of exfoliated black phosphorus (BP) reminds us why it has emerged as a promising material for electronic and optoelectronic devices[15] recently. It is an anisotropic, p-type semiconductor[58,142] with hole mobility between 100 cm^2 V^{-1} s^{-1} and 1,000 cm^2 V^{-1} s^{-1} [10], on/off ratio at room temperature between 10^2 and 10^5 [58] and tunable direct bandgap between 0.3 eV for the bulk[2] and 2.2 eV for the monolayer[34,62]. BP offers several opportunities for applications: water splitting[146], nanoresonators[35] and gas sensing[147] are just a few examples in literature.

Unfortunately, the prompt oxidation of BP compared with other 2D materials[31,43,53,148–150], is a major obstacle[100,151] for practical applications. This has turned scientific attention towards the understanding of oxidation mechanisms and the development of preventive methods to protect the material[100]. The relevance of the oxidation processes in black phosphorus is such that according to Kuriakose et al (2018): "*there is a general consensus that this rather unique material cannot be translated from the academic laboratories to real-world applications if a reliable solution to this problem is not established*"[100].

Oxidation in BP may cause dramatic structural transformations[32–34,152], but controlled oxidation can be useful to engineer its electronic properties[66,149,153], increase its environmental stability by passivation[33,34,101,154], enhance selectivity[32,115], or enhance the lubrication straight to the superlubric regimes[151]. Moreover, the environmental instability of the exfoliated materials even raises some doubt about the intrinsic properties of few-layers black phosphorus, as some of the published results may have been obtained on partially oxidized materials[69].

The chemisorption of oxygen dimers (O_2) over BP is promoted by visible light and crystal defects, as the potential barriers decrease from values larger than 10 eV in pristine surfaces to less than 6 eV at intrinsic defect sites[155,156]. Experimentally, the effect of light on oxidation has been proven and samples stored in dark show lower rates of degradation[45]. Edmonds et al (2016), working on air-oxidized bulk BP crystal, have demonstrated the presence of several types of oxides[33] in agreement with theoretical studies[34], but phosphorus pentoxide (i.e. $O' - (P_2O_5)_\infty$) is considered to be the most stable oxide form[34,141].

Light, water, and oxygen are environmental parameters required for the oxidation of black phosphorus according to theoretical[32,155] and experimental[45,65,101,157] studies. Favron et al (2015) proved that independently, neither visible light (in a vacuum better than 5×10^{-6} torr), nor oxygen or water are able to induce degradation in black phosphorus detectable by conventional Raman spectroscopy (2×10^4 Wcm^{-2} at λ=532 nm)[45]. Similarly, Woomer et al (2015) confirmed the role of light (λ=460 nm) in oxidation processes by using XPS measurements and oxygen (not dried) exposure. The oxidation was indicated by the broadening of the peak at 133 eV[65].

Kuntz el at (2017) demonstrated the effect of O_2 and H_2O on the oxidation of black phosphorus. Basal surface oxidation was characteristic for oxygen, while water-induced degradation was related to pre-existent defects and edges[101]. They described a detailed deconvolution process for the identification of different types of oxides in the XPS spectra. However, XPS was not sensitive enough to differentiate between the edge and basal oxides and the correlation between the binding energy and the type of oxide is not strong enough for reliable identification. As previously described, Kuntz et al (2017) proposed that the signal corresponding to P=O from surface oxides was located at approx. 131.5 eV, but Edmonds et al (2015) assigned the same binding energy to the O-P=O present in planar oxides[33]. In the same way, both studies seem contradictory in predicting a passivating layer with native oxides, with Kuntz et al suggesting that the by-products of the oxidation catalyze the degradation and highlight the difficulty to design a self-passivating oxide[101].

The oxidation of black phosphorus modifies the electronic properties of the material, but the degree of modification depends on the type of the formed oxide. Different kinds of

modifications are expected: lattice parameters variations[34,141,155,158]; vibrational energy variations due to the presence of oxygen bonding[32]; and electronic properties variations[33], depending on the type of oxide, the degree of oxidation[58] and the local geometry[155].

Theoretical studies[32,34,44,154] predicted the formation of oxygen bonding in dangling, bridging and interstitial configurations (**Figure 23**). Dangling and bridging oxygen bonds are electronically neutral, but the interstitial configurations create levels in the gap[32,153]. Interstitial oxygen is characterized by higher lattice distortions[32]. However, the Coulomb repulsion between oxygen p orbitals is higher for the dangling type of oxides[34], which is the reason why the P=O bonds always point away in different directions from the zigzag ridge where they are chemisorbed[32,34,155].
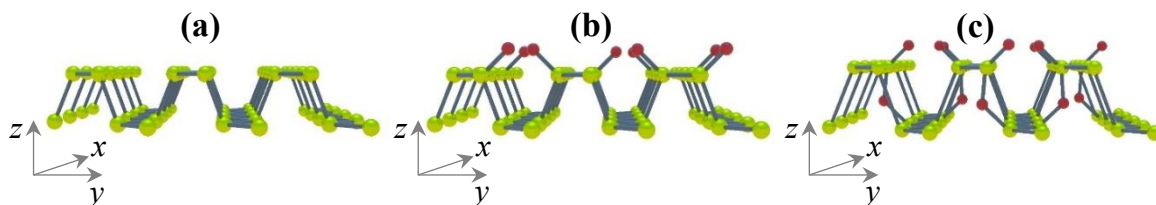
Figure 23. Oxidized black phosphorus forms. Pristine monolayer (a), surface dangling oxygen (red) – BP oxide (b) and interstitial and dangling oxygen configurations (c).

The bandgap engineering of phosphorene has been proposed by different methods: modification of the external conditions (i.e. electric bias, mechanical strain),[146] functionalization,[44] heterostructures,[58] passivation,[31,33,44,45,95] oxidation[34,66,153,154,159] and alterations in the local geometry[66,155] are some examples. For instance: BP controlled oxidation or passivation with h-BN can induce higher hole or electron mobilities, respectively,[58] and oxidation or doping with H_2 and F_2 changes the bandgap from direct to indirect[34,44,153].

In general, some similarities have been highlighted for highly oxidized forms (t-P_4O_{10} and p-P_4O_{10}): the valence and conduction bands always come from the oxygen p orbitals (e.g. in dangling and bridging configurations),[34] the higher occupied levels are degenerate dispersionless states, and the conduction bands are slightly dispersive[34]. These features are of importance as the tuning of the bandgap increases the stability of the material[155] and its

feasibility for applications[101,146]. Theoretically, differences have been emphasized in comparisons between planar and surface oxides: the average binding energy (E_b) of the material depends on the number of oxygens in the unit cell, but the E_b of the surface oxide is lower than that of the interstitial (planar) counterpart by approximately 0.7 eV[34].

As stated by Ziletti et al (2015): *"the issue seems to be how oxidation is detected"*[32]. Conventional Raman spectroscopy has been useful for different purposes in the research of black phosphorus: monitoring exfoliation[31,62,119,160], alkali intercalation[161], annealing[162], photo-oxidation[45], and functionalization/passivation[67,163] are some examples. However, the predicted variety of the oxide species has not been detected to the date by Raman spectroscopy. One of the possible reasons is the thickness of the samples utilized in the characterization with micromechanically-exfoliated samples.

In the following section, a clear correlation between thermal processes and the Raman shift of the A_g^1, B_{2g} and A_g^2 vibrational modes will be established. From the *in situ* Raman evaluation, the calculated thermal expansion coefficients in the 290 K to 485 K temperature range for the A_g^1, B_{2g} and A_g^2 modes are -0.015, -0.027 and -0.028 cm^{-1}/K, respectively. DSC analysis shows an endothermic process centered at 528 K that correlates well with a mass increase detected by TGA. Raman shift temperature dependence was correlated with theoretical lattice thermal expansion and a significant deviation was detected in the stacking direction at the 500 K. Oxidation processes were also correlated with the current-voltage characteristics of few-layers black phosphorus. The activation energy for thermally activated electrical conductance in surface BP oxide was found to be 79.7 meV, approx. 40 times lower than in the planar oxide counterpart. Remarkably, the transition from surface oxide to planar oxide is characterized by an increased electrical resistance between 373 K and 448 K. The high-temperature anomalous increase in electrical resistance is associated with variations in the lattice vibrations and endothermic processes.

V.2 Experimental details

V.2.1 Sample preparation

Bulk black phosphorus crystal was purchased from HQ Graphene (Groningen, The Netherlands) and stored in dark and argon atmosphere. The exfoliation method was ultra-sonication bath (120 W, 35 kHz). 5 mg of bulk BP crystal was added to 13 mL of acetone in a glass vial tightly closed with a septum cap. The mixture was bubbled with argon to flush out the dissolved oxygen from the solvent and the free space inside the vial. The temperature during the sonication bath was kept constant at 298 K and the sonication time was fixed to 24 hours.

After the ultra-sonication period, the sample was allowed 24 hours of sedimentation after which the supernatant was collected and marked as AsEx. This sample was flushed with argon and stored for additional characterization. Another fraction was collected from the sample AsEx and centrifuged at 2,000 rpm for 30 minutes. The supernatant was collected, flushed and stored as BP2S. From the sample BP2S, another fraction was collected and centrifuged at 4,000 rpm for 30 minutes. The supernatant was collected, flushed and labeled as BP4S.

V.2.2 Few-layers black phosphorus characterization

Raman characterization was made with an excitation wavelength of 532 nm and a nominal laser power of 12.5 mW (Bruker Senterra II). The sample was drop-casted on glass microscopy slides or silicon wafers. An ultra-long working distance optical objective (4x) was used in order to keep the scanning area, laser power, and wavelength the same in all measurements. The spectral resolution was set to ~3-5 cm^{-1} and the interferometer resolution was 1.5 cm^{-1}. All the spectra were collected using 3 coadditions of 5 seconds each and taken at random places on the few-layer BP clusters over time.

The thermogravimetric analysis (TA instruments, Q500. TGA) was made using a platinum sample holder in oxidative atmosphere (synthetic air) and a heating ramp of 5 K/min. Differential Scanning Calorimetry (TA instruments, Q20. DSC) was made using an

aluminum sample holder (Pan + Lid) in nitrogen atmosphere and heating ramps of 5 K/min. The baseline was taken with empty sample holders (Pan+Lid) for the DSC measurements.

The absorption spectra in the UV-Vis-NIR region were measured in a spectrophotometer (Hitachi, U-2001) with a sweep speed of 100 nm/min. The scanning window was set between 300 nm and 1100 nm. The samples were placed in a quartz High Precision Cell with a light path of 10 mm (Hellma Analytics).

The hydrodynamic size and zeta potentials of the suspensions were measured by Dynamic Light Scattering (Zetasizer – Nano ZS, Malvern) at λ=633 nm. The refractive index utilized for the few-layers BP was 3.4[139,140]. For acetone, the room temperature refractive index and dynamic viscosity were 1.356 and 0.3111 mPa·s, respectively.

Four-wire connections were used in the current-voltage characteristics measurements at low voltage (i.e. range between -0.5 V and +0.5 V) using a Keithley 2401 sourcemeter. The exfoliated sample (BP AsEx) was drop casted on a gold interdigitated electrode purchased from Micrux technologies (Spain) with a spacing of 5 μm between electrodes (**Figure 24**). This assembly was placed in a closed cell (HFS600E, Linkam) that allows simultaneous temperature control, gas atmosphere control, Raman spectrometry and I–V measurements. The cell was purged with argon and the sample was pre-treated at 398 K for 30 minutes to remove any water and remnant solvent traces. I developed and optimized the protocol for I–V measurements in an independent set of experiments using mesoporous nickel oxide as a model system. While this is considered an integral part of my doctoral work, results are not detailed here so that the topical homogeneity of the thesis is maintained. Rather, NiO results are reported in reference 82.

The thermal activation energy for the electrical conduction was calculated using the Arrhenius model in Eq. 9.

$$R(T) = R_0 \cdot e^{(E_a/K_B T)} \qquad \text{Eq. 9}$$

Here, R is the electrical resistance, E_a is the activation energy, K_B is the Boltzmann constant and T is the temperature. This equation assumes that the changes happen inside the

semiconductor, with higher temperature more and more carriers are activated getting to higher energy levels.
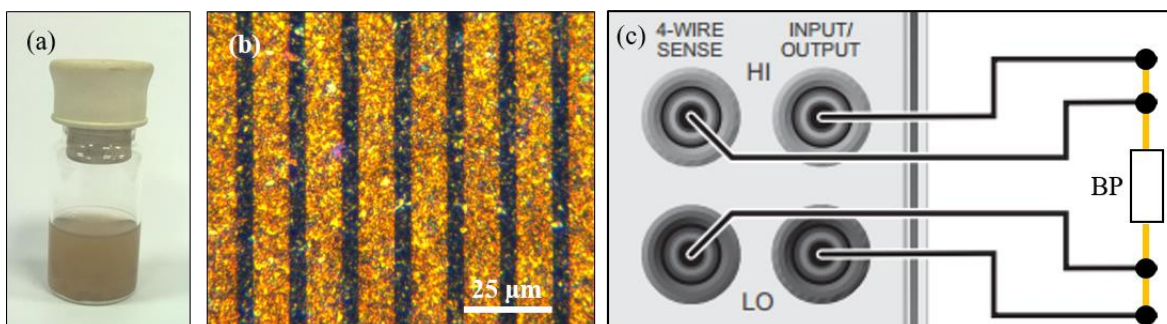
Figure 24. Sample BP AsEx suspension in acetone (a). Micrograph of the sample BP AsEx dropcasted on the interdigitated electrode (b). Four-wire connections to the source meter Keithley 2401. Adapted from the user manual (c).

V.3 Results and discussion

The suspensions produced by the Liquid Phase Exfoliation (LPE) method were characterized by DLS and the results are shown in **Table 8**. All samples were stable with apparent zeta potentials larger than 30 mV. The average hydrodynamic size was controlled by increasing centrifugation speeds. My previous results have confirmed that acetone can be used for the exfoliation of black phosphorus with good reproducibility of the topographical features (size, thickness, and stability). The produced material is easier to handle and clean than that obtained with other solvents as NMP or CHP. In section IV (page 33), the topographical characteristics of the flakes produced with LPE in acetone were discussed[164]. The correlation between AFM measurements and hydrodynamic sizes constitutes an operational advantage at the moment of characterizing the material because DLS is considerably faster than atomic force microscopy and the results are representative for the whole suspension.

The optical bandgaps of the exfoliated materials are shown in **Table 8**. The close match between the optical bandgap of the sample BP4S and the theoretical electronic bandgap of the monolayer (E_g: 2.2 eV[62,165]) is explained by the relationship between the exciton binding energy (-31.1 meV)[65] and the dielectric constant of the medium (acetone dielectric constant,

$\varepsilon = 20.7)$[65]. From these results, we conclude that our suspensions are mixtures of monolayers, bilayers, and trilayers, and their composition shifts towards isolated monolayers with increasing rotational frequency during centrifugation[164]. This is an important characteristic of the sample as it allows collecting Raman spectra with less or no interference from inner flakes in the crystalline structure.

Table 8. Characterization for the exfoliated and centrifuged material

Sample	Hydrodynamic size (nm) [a]	Zeta potential (mV) [a]	Optical bandgap (eV) [b]
As Ex	230	-42.3 ± 0.27	1.48
BP2S	146	-35.8 ± 0.92	1.95
BP4S	96	-38.1 ± 0.32	2.15

a Measured with Dynamic Light Scattering. b Estimated from the UV-Vis-NIR spectra.

V.3.1 Thermal analysis

Thermogravimetric curves for bulk BP in oxidative media (synthetic air) are presented in **Figure 25**. The onset temperature of the mass increase was 630 K (**Figure 25a**). Additionally, two samples were tested at different heating ramps: 5 K/min (**Figure 25a-b**) and 10 K/min (not shown). The weight derivatives show a starting point for the mass increase at approx. 493 K (**Figure 25b**).

The sample decomposition, measured as a mass decrease, was predominant at approx. 703 K (**Figure 25a**). The first derivative peaks were located at approx. 683 K and 753 K, and indicate the temperatures of the greatest rate of mass increase and decrease, respectively (**Figure 25a**). These results are in agreement with those obtained with *in situ* scanning/transmission electron microscopy by Liu et al (2015). In their case, the SAED patterns for exfoliated black phosphorus (thicknesses between 10 and 40 nm) showed decomposition starting at approx. 673 K[50].
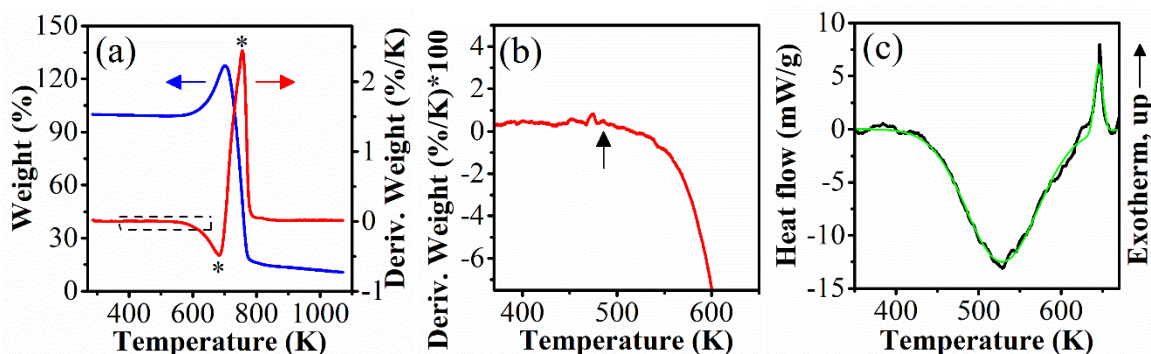
Figure 25. TGA for bulk BP in oxidative media (synthetic air). Onset temperatures are calculated from the lineal extrapolation before and after the inflection point (a). Detail of the region dashed in (a) (heating ramp: 5 K/min) (b); Arrow in (b) indicates a temperature of 493 K. DSC from the bulk starting material (black) and the peak fitting output (green) (Nitrogen media, heating ramp: 5 K/min; aluminum pan and lid).

Two different processes were detected by DSC (**Figure 25c**): an endothermic process centered at approx. 528 K and an exothermic peak centered at approx. 643 K. The endothermic feature was broad (FWHM: 101 K) and started at approx. 423 K. The exothermic peak was 10 times sharper (FWHM: 11 K), had low intensity (approx. 5.2 mW/g) and was detectable at almost the same temperature with the maximum rate of oxygen uptake, as seen from the TGA measurements in oxidative media (**Figure 25a-b**).

Two exothermic processes are have been described in the literature for BP: oxygen chemisorption on black phosphorus[32,44,115,155,159], and the formation of interstitial oxygen bonds[32]. We suppose that our observed exothermic peak relates with oxygen chemisorption as oxygen was available for the sample before it was enclosed in the sample holder of the DSC measurement. The cooling cycle was exothermic (not shown) and can be interpreted as reversibility of the broad endothermic peak shown in **Figure 25c**. The reversibility is later shown by *in situ* Raman spectroscopy.

While the exact nature of the endothermic process is uncertain, it appears safe to exclude the melting-crystallization process since the melting temperatures of black and red phosphorus are 87 3K and 893 K, respectively[166]. Liu et al (2015) reported a thermally-

induced increase in the lattice parameters of exfoliated black phosphorus[50] in the same temperature range as our DSC measurements. On the other hand, Ziletti et al (2015), based on theoretical calculations, reported the binding energies of -1.66 eV and -2.08 eV for interstitial and dangling oxides at PBE level, respectively; and transformation from dangling to interstitial oxygen requires 0.69 eV via oxygen penetration into the lattice[32]. Based on this evidence, we suggest that the endothermic process is caused by the lattice thermal expansion[50] and subsequent formation of interstitial oxygen bonding, as larger and weaker P-P bonds and Coulomb interaction between dangling oxygens favor interstitial oxygen formation. In a second step, the new configuration reduces the Coulomb repulsion[34] and allows higher oxygen incorporation (i.e. mass increase) as observed by TGA (**Figure 25**) giving place to the theoretically predicted planar type of oxides (**Figure 23c**).

Summarizing, we propose that the transitions visible in the thermal analysis evidence the transformations from the surface to the interstitial type of oxides, possibly at intrinsic defects since the thermal energy involved is lower than that necessary for the transition in defect-free surfaces. This confirms that the primary outcome of oxidation are surface oxides (instead of interstitial types) and facilitates the understanding of the Raman spectroscopic results discussed below.

V.3.2 Few-layers black phosphorus oxidation: *in situ* Raman spectroscopy

The following results were obtained from measurements in the backscattering configuration, therefore, only allowed vibrations in the first Brillouin zone are visible. The typical Raman spectrum for the bulk starting material is presented in **Figure 26a**. According to calculated phonon dispersion curves (**Figure 5**), the A_g^1, B_{2g} and A_g^2 vibrational modes are visible in the first Brillouin zone and oscillate along the *z*, *y* and *x* directions, respectively[53,66]. The TEM image presented in **Figure 26** shows a good agreement with the results of DLS characterization in **Table 8** and previous AFM measurements[164].
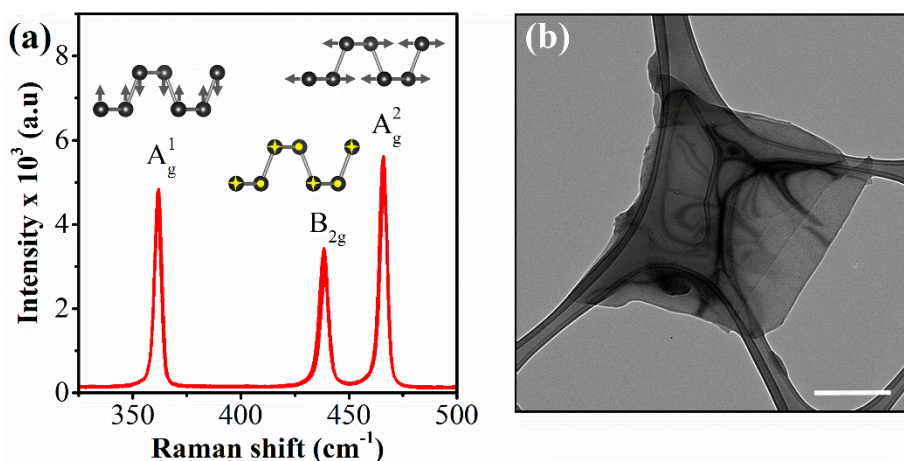
Figure 26. Raman characterization for the bulk starting material and the representation of the visible vibrational modes (a). TEM image of the Few-Layers black phosorus (AsEx). Scale bar: 500 nm.

The following features in the Raman spectra have been identified as signatures of oxidation: decrease of the integrated intensity ratio (A_g^1/ A_g^2)[31,45,53]; decrease of the overall Raman intensity; and the emergence of a broad band between the peaks corresponding to the B_{2g} and A_g^2 vibrational modes. Additionally, the blueshift in the Raman spectra of black phosorus has been related with thermal annealing processes of exfoliated materials (thickness: approx. 15 nm) in a nitrogen ambient and temperatures up to 473 K[162] and the degradation of thick samples (thickness >35nm)[110].

Previously, the correlation between oxygen content and electronic properties has been discussed[34,149]. In addition to the prediction of electrically neutral oxides[32], Malyi et al (2017) stated that oxygen-poor compounds can be considered as "black phosorene modified by oxygen adsorption"[149]. The coexistence of the different types of oxides is expected as their energies are degenerate in relation to the full oxidized forms (P_2O_5)[32,34,159].

Ziletti et al (2015)[32,34] predicted vibrational modes at 1,099 cm^{-1} for dangling oxygen, 574 cm^{-1} and 763 cm^{-1} for interstitial oxygen and no vibrational modes between 500 and 1,000 cm^{-1} for surface oxides. Despite the several studies on monitoring oxidation, those vibrational bands have not been detected with conventional Raman spectroscopy. In **Figure 27** a different approach is presented: FTIR measurements demonstrate the coexistence of

various types of oxides in air oxidized samples. The evaluation of an air oxidized sample (2 months exposure) by infrared spectroscopy in reflection mode revealed the presence of pyrophosphates (P-O-P)[167], phosphonates (POOH)[167], phosphinic acids (RPO(H)OH) and phosphorus pentoxide (P_2O_5)[168,169]. These types of phosphorus-oxygen bonds are present in the previously described black phosphorus oxides as dangling and bridging oxygen bonds (see **Figure 23**). Other weak bands were also detected in the region between 2680 cm^{-1} and 2725 cm^{-1} (not shown) and they were attributed to P-OH bond vibrations[167]. The P=O and P—O stretching modes were detected at ~1200 cm^{-1}, 1386 cm^{-1}, 1417 cm^{-1} and ~880 cm^{-1} [59,169], in partial agreement with predicted P=O stretching mode positions[34].
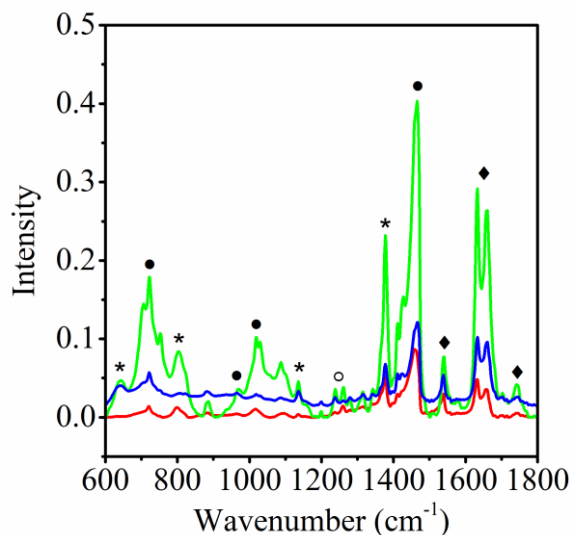
Figure 27. Infrared spectra for 3 different samples of an air-oxidized exfoliated black phosphorus sample. Representative bands for ° phosphonates, • pyrophosphates, ♦ phosphinic acids, and * P_2O_5 are marked.

Edmonds et al (2015) detected bridging and dangling oxygens on the surface of air-oxidized bulk black phosphorus[33]. In agreement with theoretical studies, the electronic properties of black phosphorus were altered by oxidation: at lower levels of oxidation, the work function exhibited small variations of 0.1 eV in comparison with pristine bulk black phosphorus, but at higher states of oxidation, the electronic bandgap had a large modulation (>4.5 eV).

XPS measurements on acetone-exfoliated black phosphorus (AsEx) mounted on a silicon wafer are shown in **Figure 28**. After 21 days of air-oxidation (**Figure 28b**), broadening of the peak at 133.5 eV was visible in agreement with the previous reports[65]. Edmonds et al (2015) used synchrotron-based photoelectron spectroscopy and they reported the appearance of two peaks at 131.5 eV and 132.7 eV associated with bridging and dangling oxygen bonding, respectively[33]. The deconvolution of measurements revealed that the broad peak in the same region (132.4 eV) diminishes with the increasing intensity of the peak corresponding to phosphorus pentoxide (P_2O_5) at 133.5 eV.
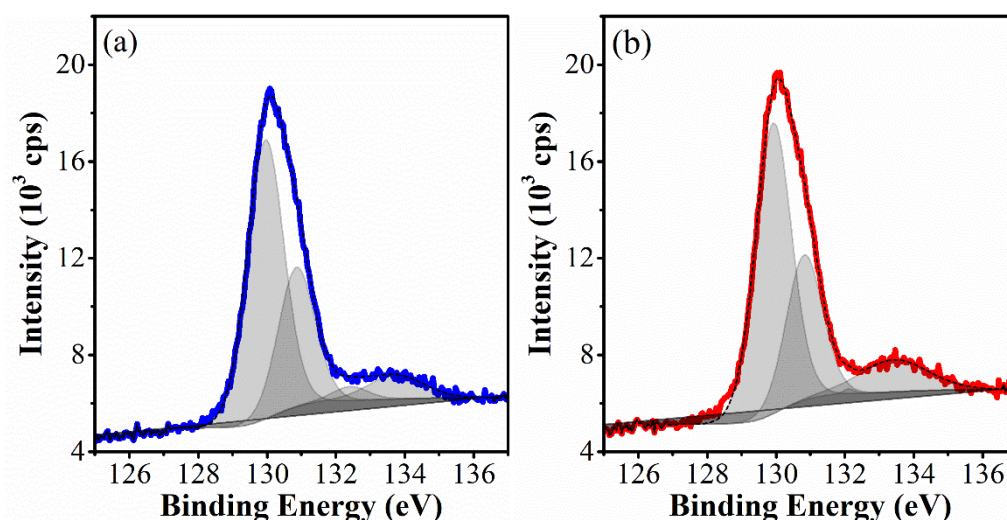
Figure 28. XPS measurements for acetone-exfoliated black phosphorus (AsEx). Starting point (a) and 21 days later (b).

Exfoliated flakes were analyzed by TEM (**Figure 29**) in order to evaluate their crystal structure after controlled oxygen exposure. From the electron diffractions, no major modifications were detected in the zigzag and armchair directions (i.e. lattice constants *a* and *b*) in agreement with the discussion on page 46 and published results[164].
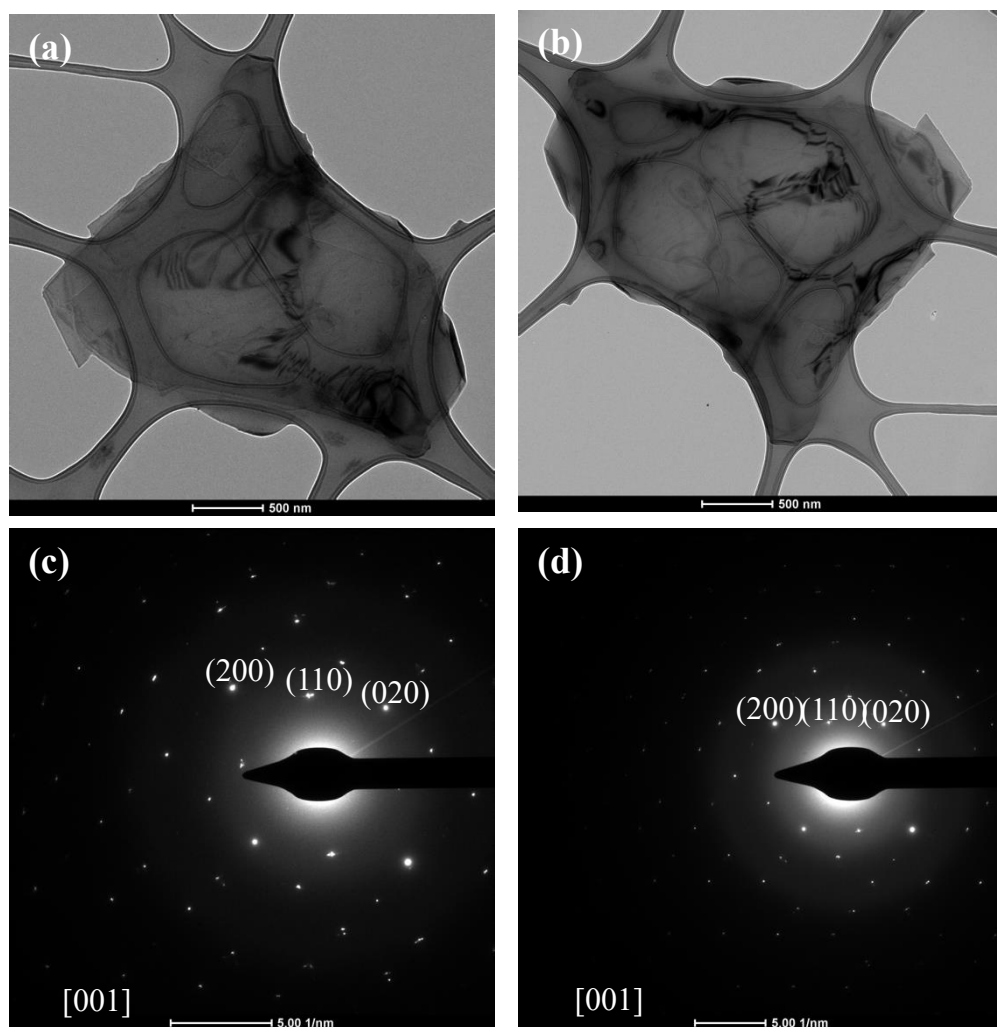
Figure 29. Comparison of lattice constants. TEM image of a flake before (a) and after (b) pure oxygen exposure at 343 K. Electron diffractions from the flake in (a-b) before (c) and after (d) oxygen exposure.

XRD patterns were collected after cycles of oxygen exposure at 523 K (**Figure 30**), but no modifications in the stacking direction were detected. The lattice constants calculated for the exfoliated materials after the oxygen exposure are *a:* 3.3 Å, *b:* 4.3 Å and *c:* 10.8 Å. These results suggest that the surface oxide is the primary outcome of oxidation and they contribute to the literature debate on the stability of the oxidized black phosphorus species in the early stages of oxidation.
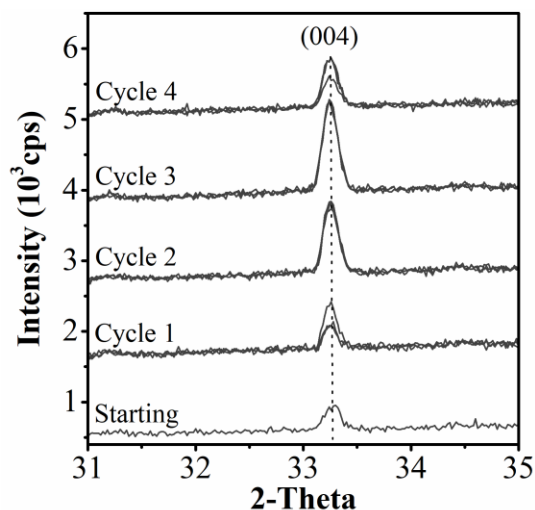
Figure 30. XRD patterns recorded at room temperature from acetone-exfoliated black phosphorus (BP2S) casted on a silicon wafer. Between each consecutive cycle, the sample was heated up to 523 K and cooled down to room temperature. CuKα; λ: 1.54 Å

In the dangling configuration, the oxygen atoms bond to the surface at the zigzag ridge (**Figure 23**) and the P-O bonds in the dangling position form an angle of 44.5° from the surface[32,35,115]. Herein, the differences in electronegativity between P and O atoms polarize the surface[32] with different implications[146] (i.e. "water bubbles" formation[155]). We suggest that the geometry of surface oxides and the induced polarization explain the blueshift detected in some of the samples under evaluation (**Figure 31** and **Figure 33**). Interestingly, monotonic blueshift for the P=O stretching mode has been proposed for the detection of dangling oxygens[34], however, it has not been reported in the literature with conventional Raman spectroscopy.
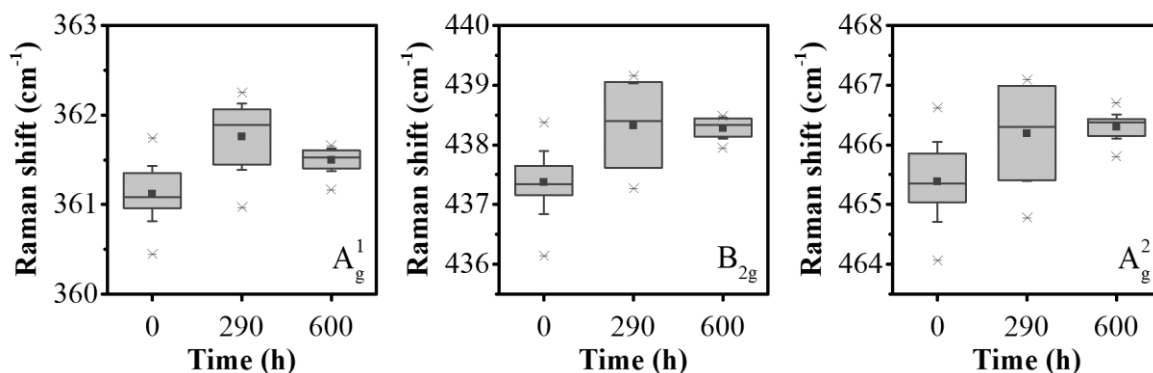
Figure 31. Raman shift aging at room temperature for a sample (BP2S acetone) drop casted on a silicon wafer for each vibrational mode.

Another sample was drop casted on glass and placed in the temperature-controlled probe stage (HFS600E, Linkam) (**Figure 32**). The stage was tightly closed and heated up to 373 K in argon flow (200 mL/min) as pretreatment. After 5 minutes of pretreatment, the argon flow was replaced by oxygen flow set to 10 mL/min. The Raman shift was measured every 30 min (Raman Senterra II, $\lambda = 532$ nm, nominal power = 12.5 mW) and the results are shown in **Figure 33**. The measured blueshift followed a similar trend as seen for air-oxidized samples $A_g^1 < B_{2g} < A_g^2$ but the slopes from the linear fit were approximately 120 times larger for the samples measured in O_2 atmosphere at 373 K than for the air oxidized samples.
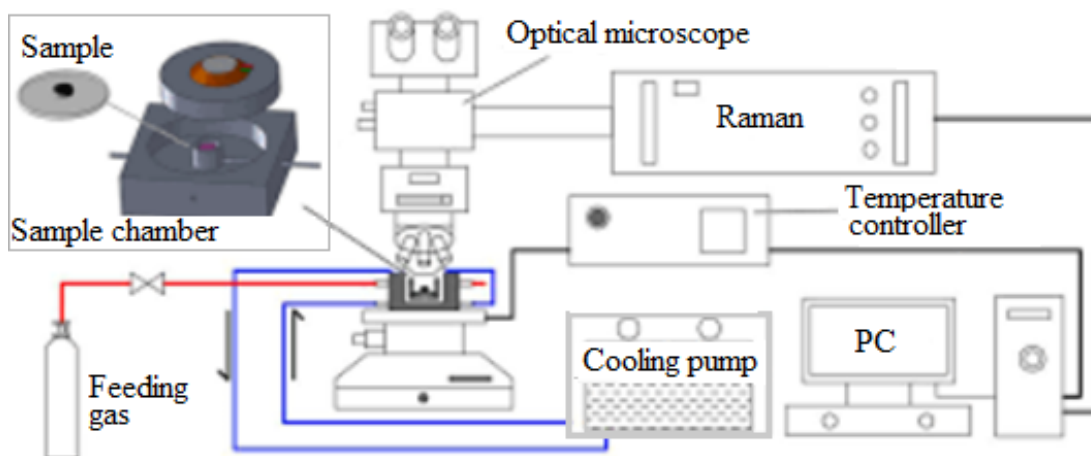
Figure 32. Overview of the purpose-built measurement set up showing the confocal Raman microscope (Senterra II, Bruker) and the sample chamber (HFS600E, Linkam)
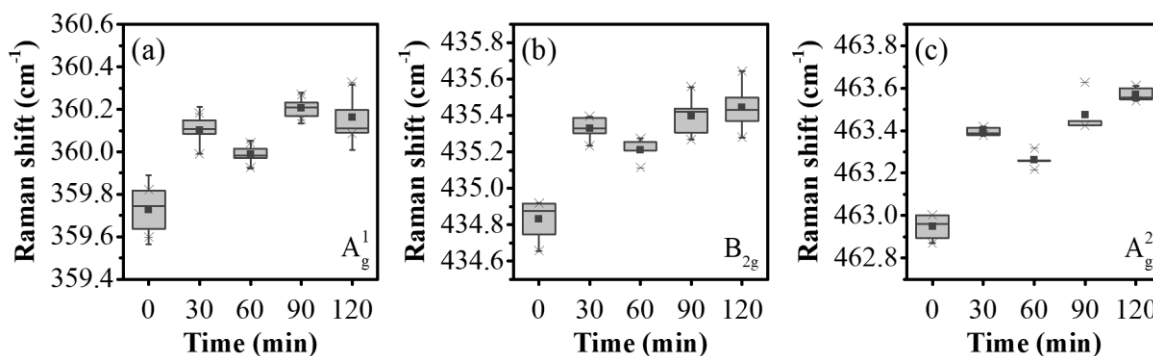
Figure 33. *In situ* Raman shift in oxygen atmosphere at 373 K. A_g^1 (a), B_{2g} (b) and A_g^2 (c) vibrational modes. Linear fitting slopes for the mean values: 0.195 cm^{-1}/h, 0.2586 cm^{-1}/h, and 0.2652 cm^{-1}/h for the A_g^1, B_{2g} and A_g^2 vibrational modes, respectively. The boxes enclose the median between the 25th and 75th percentiles. The square represents the mean value and asterisk represent the max. and min. values.

The blueshift was almost two times larger for the vibrations in the *xy* plane (B_{2g} and A_g^2 modes) than for the vibration in the stacking direction (A_g^1 mode). We attributed these differences to the position of the dangling and bridging oxygen on the few-layers black phosphorus as it has a bonding preference over the zigzag ridge at 44.5° away from the phosphorene surface[32,35].

The linear fitted slopes for the mean values during oxidation at 373 K with 2 h oxygen exposure were 0.195 cm^{-1}/h, 0.2586 cm^{-1}/h and 0.2652 cm^{-1}/h for the A_g^1, B_{2g} and A_g^2 vibrational modes, respectively. The fact that the blueshift was not visible in every analyzed sample might be due to the differences in the number of oxygen atoms per unit cell prior the measurements and the calculations showing that oxygen-poor compounds are almost similar to the pristine counterpart[149].

The temperature dependence of the Raman shift (temperature range: 98.15 K to 673.15) was evaluated for a drop-casted sample (i.e. BP4S acetone) mounted in a temperature controlled probe stage (HFS600E, Linkam) (**Figure 32**). The stage was fed with argon at 200 mL/min rate. The spectra were fitted with Lorentzian functions and the center of the peaks was tabulated against the corresponding temperature. In **Figure 34**, the reciprocal Raman

shift is plotted against temperature (blue squares) and overlaid on the thermal expansion of the lattice constants as calculated by Villegas et al (2016)[49] (black).

For temperatures lower than 493 K, the A_g^1, B_{2g}, and A_g^2 vibrational modes exhibit an excellent agreement with the lattice constants in the stacking, zigzag and armchair directions, and the results agree with previous reports on a 4 nm thick layer[170]. Previously, in page 59 (**Figure 25b-c**) an endothermic process starting at approx. 493 K (220°C) was described, and *in situ* Raman spectroscopy identified this process in the stacking direction (A_g^1 vibrational mode) in **Figure 34a** at the same temperature. This supports our model proposed for explaining the thermal analysis results, but this effect was not visible in thicker layers[170] possibly because the oxidation happens only at the topmost layer[33] and measurements with thicker samples would be masked by the inner layers.

As expected, the dangling to interstitial transition requires an additional expansion in the stacking direction to accommodate oxygen atoms in between two phosphorus atoms in the stacking direction, and this endothermic process can be followed by *in situ* Raman and DSC.
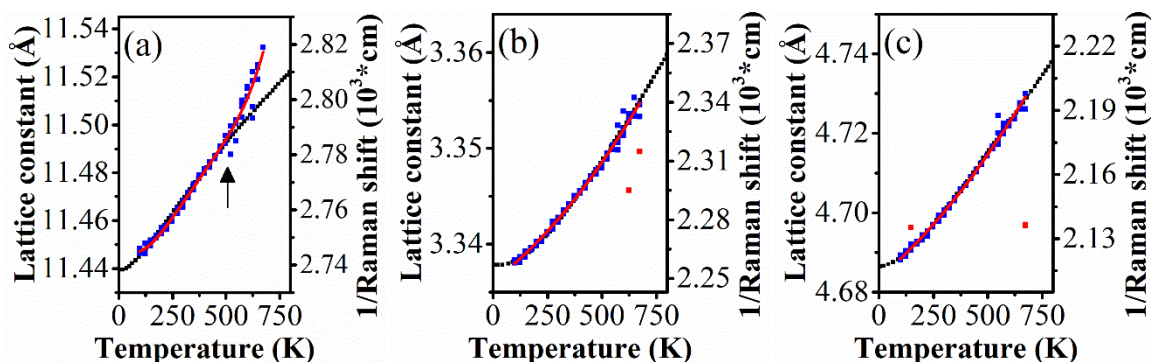
Figure 34. Raman shift temperature dependence for the sample BP4S acetone. Calculated lattice constants of black phosphorus as a function of temperature (black)[49]. Reciprocal of the Raman shift (peak position) for each vibrational mode (blue square). Raman shift temperature dependence in the stacking direction (A_g^1 mode) (a). The black arrow indicates a temperature of 500 K (a), zigzag direction (B_{2g} mode) (b) and armchair direction (A_g^2 mode) (c) of the BP unit cell.

The thermal expansion coefficient and the phonon frequency at 0 K were calculated from the linear fit parameters of the Raman shift temperature dependence (**Figure 34**) in the temperature range 290 K to 485 K (**Table 9**) according to the Grüneisen model in Eq. 10. These results are in good agreement with the previous reports[143,144,171] for evaluations in the temperature range 293 K to 433 K.

$$\omega(T) = \omega_0 + \chi\, T$$

Eq. 10

Table 9. Linear fitting parameters for the Raman shift temperature dependence

Vibrational Mode	Slope (cm^{-1}/K)	Intercept (cm^{-1})	R^2
A_g^1	-0.015	366.4	0.98
B_{2g}	-0.027	446.5	0.99
A_g^2	-0.028	475.3	0.99

The correlation between the lattice expansion and the Raman shift shown in **Figure 34** can be described by the following mathematical model, where $[\omega_0 + \chi\, T\,]$ denotes the Grüneisen model parameters corresponding to each vibrational mode and *a*, *b* and *c* are the lattice constants:

$$a = 25.762 - 0.101 \times [\omega_0(B_{2g}) + \chi\,(B_{2g})T\,] + 1.129 \times 10^{-4} \times [\omega_0(B_{2g}) + \chi\,(B_{2g})T\,]^2$$

$$b = 5.873 - 0.00251 \times [\omega_0(A_g^2) + \chi\,(A_g^2)T\,]$$

$$c = 14.459 - 0.00826 \times [\omega_0(A_g^1) + \chi(A_g^1)\,T]$$

We propose this mathematical model as a baseline to evaluate the modifications of the lattice caused by processes like oxidation or interstitial intercalation/doping in the temperature range 200 K to 450 K for few-layers black phosphorus. The R-square coefficient for the three equations was 0.995, 0.9996 and 0.9995 for the lattice constants *a*, *b* and *c*, respectively.

Additionally, *in situ* Raman evaluations have demonstrated other effects on the Raman spectra of black phosphorus (**Figure 35**). For example, during air exposure it is possible to

find some broad features in the region 3450 cm^{-1} and 2400 cm^{-1} corresponding to -OH and P-H respectively. Even though these spectral features are not always detected and therefore, they may not be ideal oxidation indicators, they could be related to the temporal luminescence visible only at early stages of oxidation[69,105], because both the luminescence and the Raman features disappear at higher oxygen concentrations.
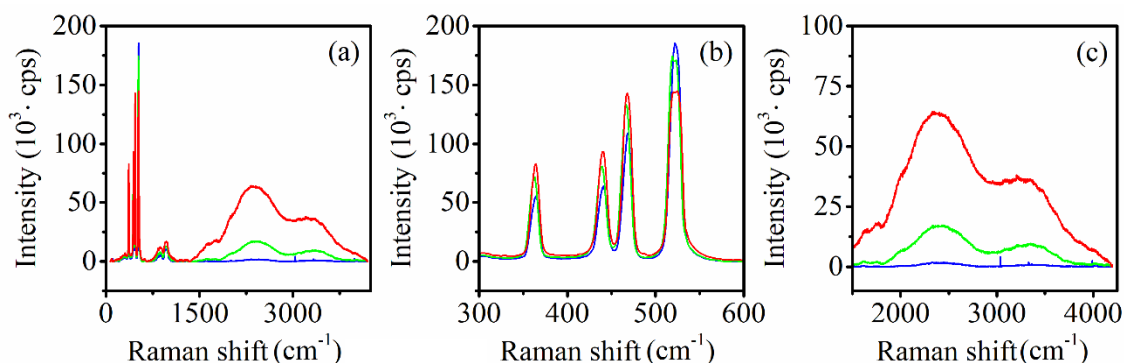
Figure 35. Few-layers black phosphorus oxidation in ambient conditions. Laser power: 2.50 mW. Laser wavelength: 532 nm. Exposure time: 100 s. 3 coadditions. Blue: starting material, t: 0 min; Green: 10 min and red: 20 min after air exposure.

In order to evaluate the reversibility of the spectral shifting, the temperature dependence of the Raman shifts of exfoliated flakes was evaluated in cyclic temperature sweeps. Raman spectra were collected at 373 K and 523 K in several heating-cooling cycles and the results are shown in **Figure 36**. While the variation in the peak positions is somewhat larger than the error of the measurement, this could be due to the aging of the samples. Therefore, the combined independent evidence provided by this Raman data and the XRD measurements discussed above (**Figure 30**) strongly suggests that the thermal process is indeed reversible.
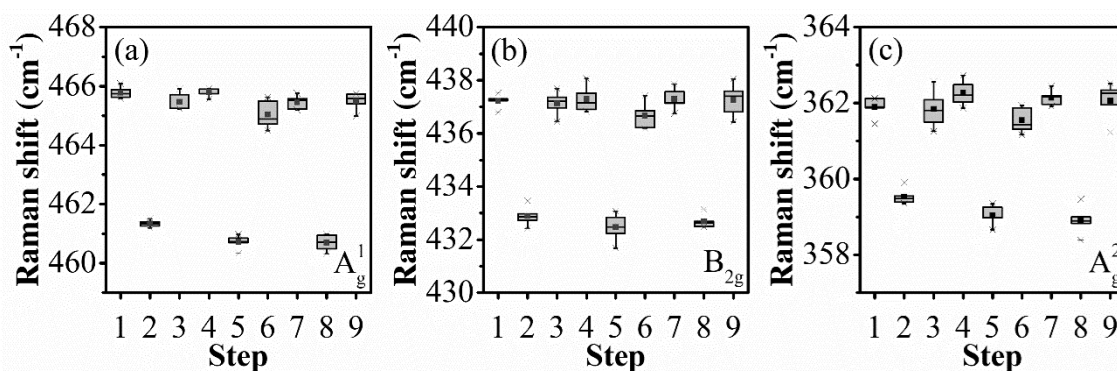
Figure 36. Raman shift temperature dependence on cyclic temperature sweep. Raman shift spectra from steps 1, 3, 4, 6, 7 and 9 were taken at 373 K. spectra from steps 2, 5 and 8 were taken at 523 K. Vibrational modes A_g^1, B_{2g} and A_g^2 are depicted in figure a, b and c, respectively. The boxes enclose the median between the 25th and 75th percentiles. The square represents the mean value and asterisk represent the max. and min. values.

V.3.3 Thermally activated electric conduction

In order to evaluate the effect of the thermal process described in the previous sections, the electrical conductance of exfoliated materials was evaluated. Herein, the relevance of oxidation in black phosphorus is highlighted as it affects the electronic structure (e.g. band position and electronic bandgap) to a higher extent than the number of layers. This has been studied in computational works[34,86] and the anticipated effects have been demonstrated for transducer applications, but some of the predictions are yet to be tested experimentally.

A new exfoliation was executed with the same procedure as previously described and the product was characterized by measuring the light absorption of the black phosphorous suspension because that is correlated with the degree of exfoliation[164]. From the UV-Vis spectra (**Figure 37b**), the electronic bandgap of the suspension was found to be approx. 1.6 eV (i.e. exciton binding energy: -31.1 meV in acetone[65]). However, another absorption edge was detected at approx. 600 nm which corresponds to an optical bandgap of 2.1 eV. These results are in good agreement with the expected value for the bilayers and monolayers[42,62]. The Raman characterization (**Figure 37c**) indicates a ratio $A_g^1/A_g^2 = 0.65$, which indicates a slight oxidation according to recent literature[31,45].
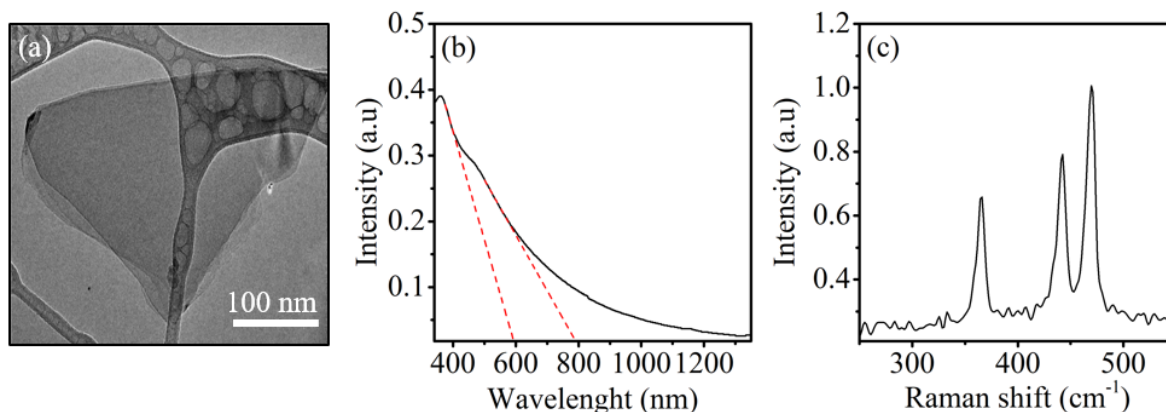
Figure 37. TEM image of a few-layers black phosphorus flake (a). UV-Vis-NIR spectra for the BP AsEx sample suspended in acetone, with dashed lines indicating the observed absorption edges (b). Characteristic Raman spectra for the drop-casted flakes exhibiting the vibrational modes A_g^1 (365.5 cm^{-1}), B_{2g} (442.2 cm^{-1}) and A_g^2 (470.2 cm^{-1}) (c).

According to DLS measurements, the hydrodynamic size of the exfoliated material was 250$\pm$ 60 nm. This value demonstrates the good reproducibility of the suspensions obtained by ultra-sonication in acetone[164]. From the characterization results and based on our previous result[164], we conclude that the new suspension was composed of monolayers, bilayers and up to 4-layer flakes. Here is important to recall that quantum confinement effects are only visible for flakes below 20 layers[63] and this defines the type of contact with the metal electrodes.

The temperature dependent current-voltage characteristics are shown in **Figure 38**. Three different processes can be identified. At low temperatures (i.e. below 373 K), exfoliated black phosphorus exhibits typical semiconductor behavior insofar as its resistance decreases with increasing temperature. At temperatures between 373 K and 448 K the behavior is characterized by an opposite trend ($\Delta R/\Delta T>0$), and above 448 K the electrical resistance decreases again as expected for semiconductors.
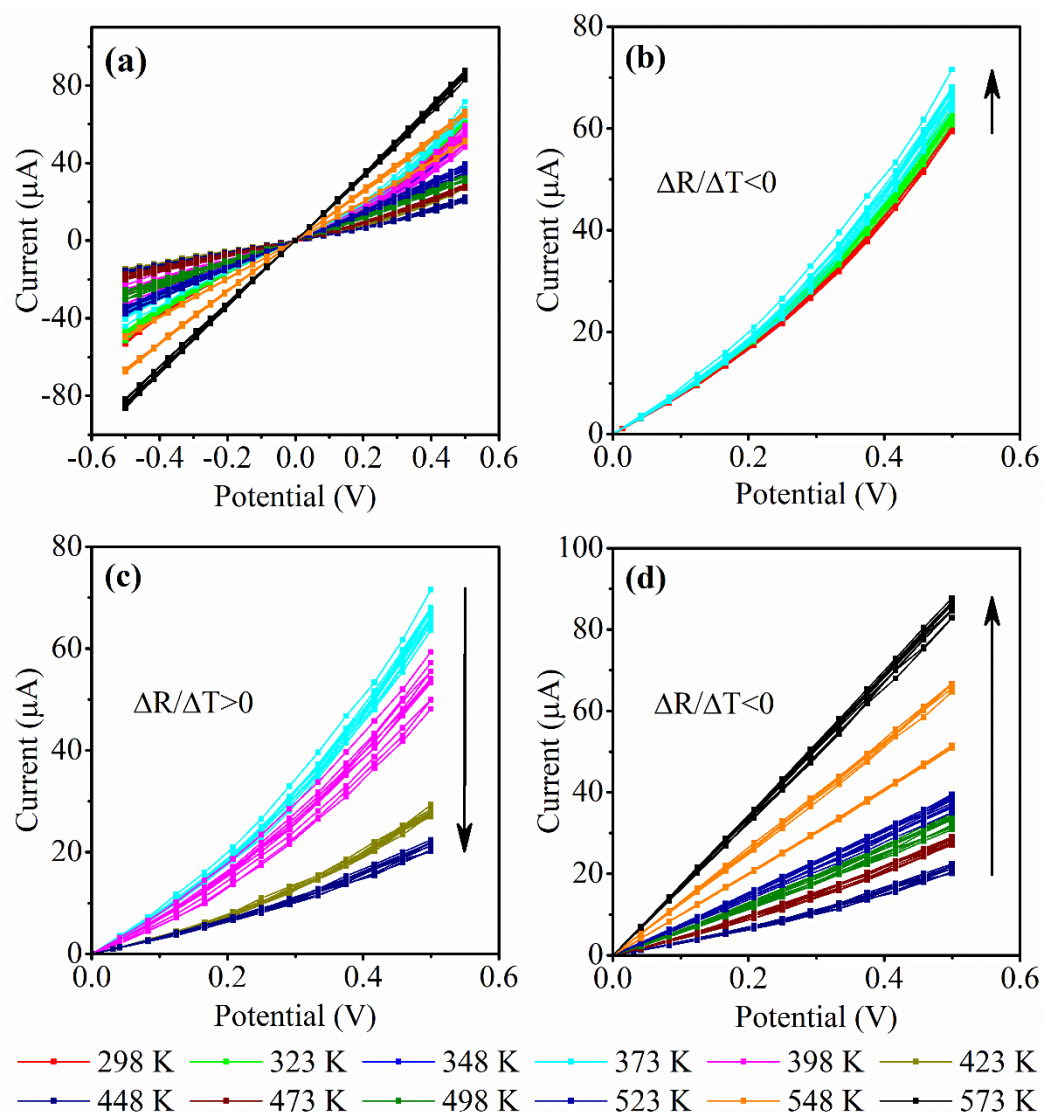
Figure 38. Current-voltage characteristics for black phosphorus. Temperature range 298 K to 573 K (a). Detailed forward bias: Temperature ranges 298 K to 373 K (b), 373 K to 448 K (c) and 448 K to 573 K (d). Arrows indicate the direction of increasing temperature.

The anomalous behavior of the electrical resistance of exfoliated black phosphorus can be interpreted on the basis of the thermogravimetric results presented in **Figure 25**. As described previously, a broad endothermic process starts at approx. 423 K and has been proposed as the oxygen endothermic transition from the surface to the interstitial position identified by a large deformation in the *z*-direction perpendicular to the plane. Correspondingly, the increase of the electrical resistance can be explained by the

reconfiguration process as it is localized at the same temperature as the endothermic process, mass increase by the incorporation of physisorbed oxygen and lattice distortions reported recently[172]. It should be noted that since our I–V measurements were performed in inert (Ar) atmosphere, the oxidation processes most likely used strongly physisorbed oxygen that has not been removed by the initial heat treatment. The formation of metastable oxides and adsorbates was recently reported for materials produced by ultrasonication[59,103,109], but the the oxide types were not identified.

Another informative feature observable during the thermal evaluation of the electrical resistance in **Figure 38** is the change in the contact type between the Ti/Au electrode and the exfoliated black phosphorus. The band alignment between gold and black phosphorus depends on the differences in work function and interface states at the heterojunction. While the work function for gold is approx. 5.4 eV, for black phosphorus it strongly depends on the number of layers (conduction band maximum for 1-layer: 5.43 eV, 2-layer: 4.85 eV, 3-layer: 4.59 eV, 4-layer: 4.46 eV, bulk: 4.35 eV[42,70]) and oxidation[33]. In the early stages of oxidation the oxidation induced work function variations are smaller than 0.1 eV. This is an interesting result because the measurement of the work function is considered to be very sensitive to oxygen and water adsorption, even before topographical variations are detectable[70].
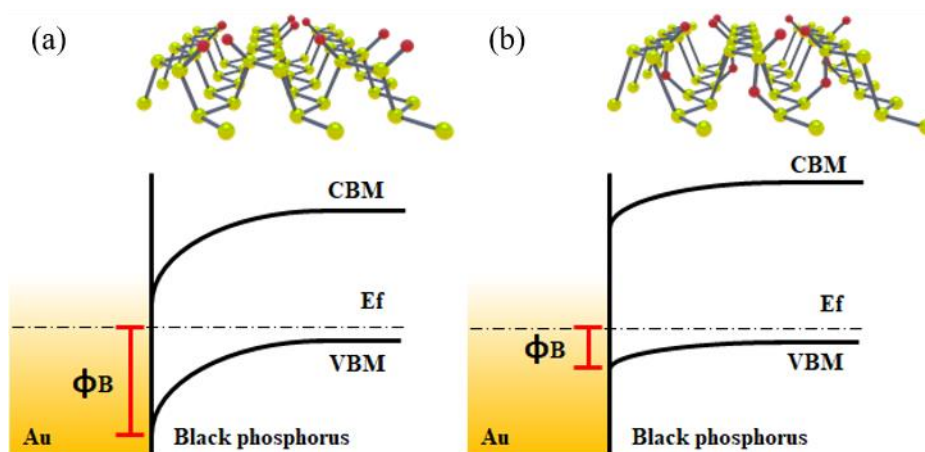
Figure 39. Schematic representations of the Au/black phosphorus junction for black phosphorus surface oxide (a) and planar oxide (b). CBM, VBM, ΦB, Ef correspond to

conduction band minimum, valence band maximum, barrier height and Fermi energy level, respectively.

Even though our exfoliated BP suspension is composed of flakes with different thicknesses, for the mechanistic interpretation we assume the dominance of bilayer flakes based on the optical bandgap measured by UV-Vis spectra (i.e. 1.5 eV is the expected bandgap for bilayers). This assumption is also supported by the slightly rectifying behavior visible at low temperatures where the ideal contact between monolayer black phosphorus and gold should have been purely ohmic. Therefore, it is more realistic to assume a bilayer system, where a Schottky barrier is expected with a slightly rectifying behavior matching the experimental observation perfectly.

On the other hand, at higher temperatures, when the endothermic process was completed, an ohmic contact is clearly visible (**Figure 38d**). This change in contact type indicates a better band alignment and subsequently, charge carriers can flow with lower or no potential barrier between the gold and the exfoliated black phosphorus flakes. This alignment can be explained by two different processes: first, the thermal energy allows the charge carriers to reach higher energy levels, and second, the temperature[49] and the oxidation[33] expand the bands, improving the alignment.

In order to quantify the change in electrical behavior, the activation energy of thermally activated electric conductance was determined. First, the electrical resistance was computed as a function of temperature, then the activation energy was calculated by fitting Eq. 11 to the data in **Figure 41**. Before applying this methodology to exfoliated black phosphorus, I validated it by comparing results obtained for multi-wall carbon nanotubes (MWCNTs) with literature data.

$$\ln R = \ln R_0 + \frac{E_a}{K_B T} \qquad \text{Eq. 11}$$

Here, R is the electrical resistance in ohms, R_0 is the intercept at 0 K, Ea is the activation energy in eV, K_B is Boltzmann's constant and T is the temperature in Kelvin. The activation energy can be calculated as the slope of the linear fitting in the Arrhenius plot.

Validation results obtained for the characterization of MWCNTs (**Figure 40**) are discussed first. The material had a residual catalyst content of 0.6 % (m/m); the external diameters ranged from 6 nm to 35 nm and the internal diameters were between 2.5 nm and 9 nm. The good agreement between our results (Ea = 11.9 meV) and literature data reported for carbon nanotubes (2.67 - 11.2 meV[173]) demonstrates that our experimental setup and evaluation protocol are indeed capable of describing the electrical properties of a material.
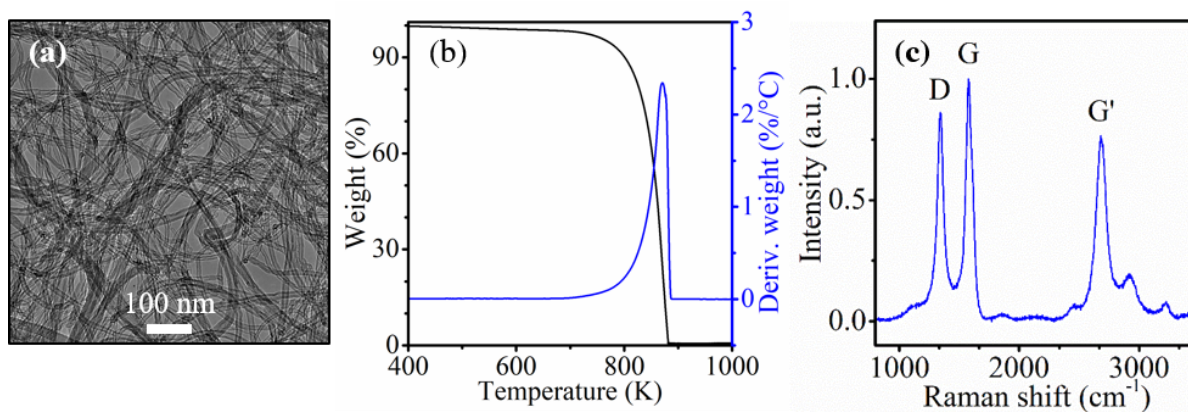
Figure 40. MWCNT characterization: TEM image (a), thermogravimetric analysis (b) and Raman spectra (c)

Interestingly, the *Ea* obtained for exfoliated black phosphorus is in the same order of magnitude as that for single-layer WS_2, however, from **Table 10** it is clear that this value is very sensitive to functionalization as demonstrated by the markedly different value reported for composite WS_2 nanowire-nanoflake hybrids[174].

Three different regions are clearly discernible in **Figure 41**. Based on our current understanding of black phosphorus oxidation, it seems safe to assume that surface oxides and planar oxides dominate the lower (T < 373 K) and the higher temperature range (T > 448 K), respectively. Increasing resistance has been reported as a signature of oxidation in FET devices (**Table 3**), and therefore, the middle transition in the 373 K to 448 K range can be assigned to a thermally activated oxidation process. A similar analysis for pristine black phosphorus flakes is yet to be undertaken in our laboratory because the exfoliation technique needs to be modified.
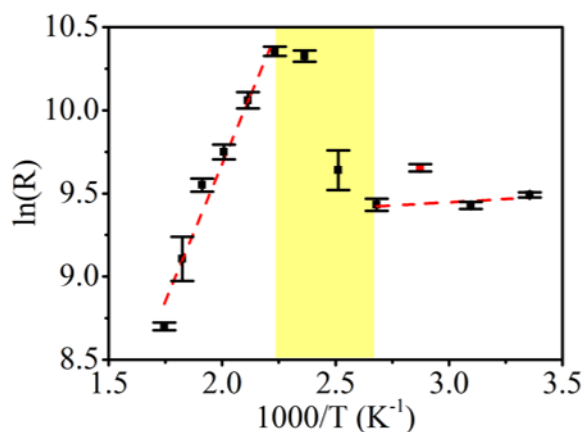
Figure 41. Arrhenius plot representation for the calculation of the activation energy of thermally activated electric conductance. Black squares represent measurement points and their standard deviation taken into account when deriving the data in Table 10, a red square denotes an outlier, and dashed lines indicate the linear fits according to Eq. 11. The transition region is marked in yellow.

Table 10. Activation energies for thermally activated electric conduction processes

Material	Ea (meV)	Ref.
WS$_2$ nanowire-nanoflake hybrids	290	[174]
Single-layer WS$_2$	5 - 85*	[175]
Multi-wall carbon nanotubes	2.67 - 11.2	[173]
Multi-wall carbon nanotubes	11.9	This work
Few-layers BP oxide (surface, low oxidation)	79.7	This work
Few-layers BP oxide (planar)	3,295	This work

* FET: *Ea* depends on V_G. At $V_G = 0$, E_a = c.a. 59 meV

Another sample was evaluated in argon atmosphere (**Figure 42**). This sample corresponds to bulk material that was not properly exfoliated. It was obtained by the self-decantation after the ultrasonication period in acetone. Here is important to recall that black phosphorus layers with thicknesses above approx. 10 nm exhibit an electronic structure similar to the bulk materials[63].
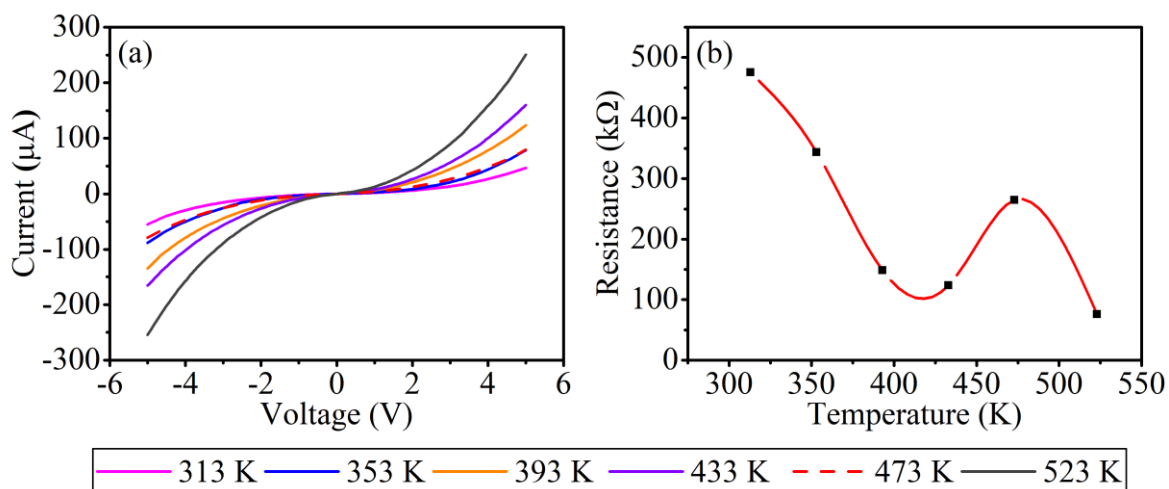
Figure 42. IV characteristics for bulk samples in the temperature range 313 K to 523 K (a). Resistance behavior calculated for the sample in (a) (b).

Unlike the exfoliated materials, the shape of the IV characteristic curves remains practically unaltered for this bulkier sample. However, the electrical resistance consistently shows the behavior discussed previously at approx. 473 K. The differences in temperature may come from the different degrees of exfoliation. Finally, another exfoliated sample was evaluated in a mixture of argon (40 mL/min) and oxygen (10 mL/min) gases flow. The results of the characterization are shown in **Figure 43** and **Figure 44**.

From the Raman characterization it was detected a decay of the intensity for all of the three Raman active vibrational modes, in agreement with the observations of Favron et al (2015)[45]. However, the A_g^1/A_g^2 intensity ratio was always the same ($A_g^1/A_g^2 = 0.52 \pm 0.01$) indifferently from the temperature and the degree of oxidation.
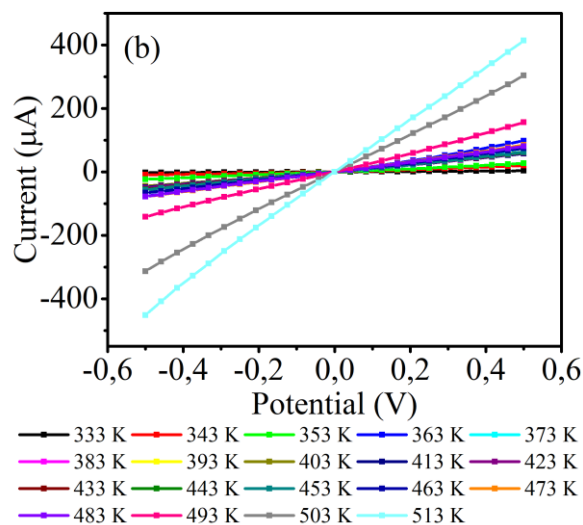
Figure 43. Current-voltage characteristics for acetone-exfoliated black phosphorus in the temperature range 298 K to 573 K in oxygen (10 mL/min)/Argon (40 mL/min) atmosphere in the temperature range 333 K to 513 K (b).
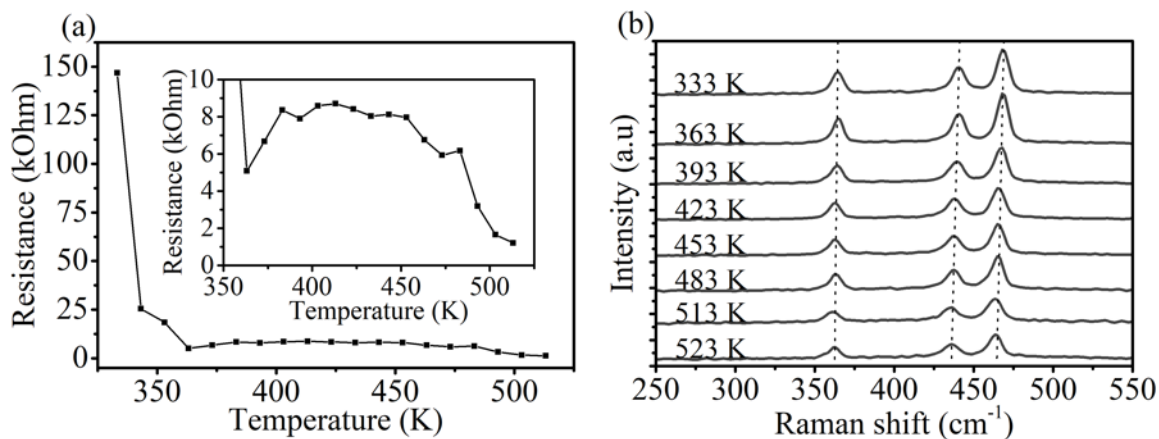
Figure 44. Electrical resistance vs temperature from the sample in fig. 43. Inset: detail of the region between 350 K and 525 K (a). Collection of Raman spectra for the sample in fig. 43 (b)

A recent experimental study has reported only a slight increase in the work function upon exposing BP flakes to ambient air[70]. Theoretical studies published in the last few years[34,115,154,176] predict the monotonic variation of the electronic bandgap with the number of oxygen atoms per unit cell[34]. The surface oxide has been proposed as an electronically

neutral oxide, formed without deformations of the BP lattice structure. The small variations of the work function[70] and the evaluation of the lattice structure[33,164] confirm the formation of electronically neutral oxides, at least during the first 48 h of exposure, and support the idea of the primary formation of surface oxides. The transition from surface to planar oxide is expected to rearrange the electronic structure and therefore, it modifies the positions of the valence and conduction band explaining the results and the variation in the contact type.

Finally, the formation of metastable black phosphorus oxides has been reported for liquid phase exfoliation[103,109]. In this work, we have proved that the electronic structure transformation is caused by oxidation processes and related the results with a recent work[172]. These results support the hypothesis that surface oxides are the primary outcome of the oxidation processes in the few-layers regime, and they serve as the starting point for the transition to planar oxides. The planar oxide was shown to have a larger work function and a different band alignment with gold electrodes as an indication of the transformed electronic structure. These results support the theoretical argument that favors the formation of surface oxide as the primary outcome at the near-equilibrium conditions, at least at lower oxygen concentrations with lower Coulomb interactions.

The use of electrical conductance measurement as fast and simple BP oxidation characterization methodology unlocks the opportunity for the in situ evaluation of functionalized/passivated few-layers black phosphorus nanocomposites. The transition demonstrated above would be possible only in the presence of small dangling substituents less affected by steric effects (i.e dangling oxygen in this case). At least in principle, the absence of such substituents (i.e. in pristine few-layers black phosphorus) would result in a lattice thermal expansion without the deformations measured for the out-of-plane vibrations we detected with *in situ* Raman spectroscopy[172].

Ziletti et al (2015) calculated the bandgap dependence on the number of oxygen atoms per unit cell. For surface oxides, the calculated bandgap was approx. 2.5 eV for 2 or 4 oxygen atoms per unit cell. However, for the planar form (i.e. with the presence of interstitial oxygen) the calculated bandgap exhibited a monotonic increase with the number of oxygen atoms per

unit cell (**Table 2**). Therefore, controlling the type of oxide and the number of oxygen atoms in the unit cell creates opportunities for bandgap engineering in black phosphorus[34].

Earlier, the visual observation of water bubbles formation at the surface of exfoliated BP has been used as the primary experimental indicator of phosphorene oxidation[115]. Here, a quantitative tool for tracking the oxidation of black phosphorus and few-layers black phosphorus by backscattering Raman was shown and correlated with thermogravimetric and electrical resistance measurements.

V.4 Conclusion

Black phosphorus is the most stable allotrope of phosphorus and thermal stabilities have been previously reported up to 823 K[45]. In situ TEM demonstrated that sublimation starts at approx. 673 K which is congruent with our thermal analysis. In this work, we have reported the formation of a new BP oxide phase at temperatures as low as 423 K.

Heat generation and dissipation during FET operation or at high switching speeds in radio frequency applications demand the understanding of the thermal properties of the active materials[177]. The dissipated electric power can raise the temperature to the failure level of the device or alter the electronic properties of the materials. Here we have demonstrated a temperature limit for the application of black phosphorus where the oxidation induces physical and electronic alterations.

Different types of oxides coexist in air-oxidized bulk black phosphorus[33,101]. Theoretical studies provide insightful results: fully oxidized compounds and intermediate states have close binding energy values[34]. Our samples contain several kinds of oxides, and oxygen-poor forms are present even after 28 days of air exposure[33]. Theoretically, oxygen adsorption is an exothermic process and the dangling position is 0.69 eV[32] more energetically favorable than the bridging and interstitial positions. The first stages of oxidation are characterized by slight or no alteration of the Raman spectra, while the temperature dependence of the Raman shift reveals a process in the stacking direction occurring at 493 K. This result was congruent with our reported thermogravimetric analysis.

In situ Raman spectroscopy gave a good match between the lattice constants and theoretical thermal expansion of the unit cell and validated previous theoretical calculations on black phosphorus oxidation. This work unlocks opportunities for applications of bandgap engineering with black phosphorus native oxides. We proposed a simple mathematical model to track deformations in the lattice structure by using the Grüneisen model and fitting the Raman spectral shifts as a function of lattice temperature.

Based on thermal analysis, we reported the decomposition of bulk black phosphorus[50] at approx. 703 K in oxidative media. Additionally, we found an inflection point at approx. 493 K above which oxygen uptake became exponentially more intense. Therefore, this temperature should be considered as the upper operational restriction threshold for the usage of black phosphorus in certain applications. Transitions were visible in DSC measurements at approx. 528 K for heating ramps of 5 K/min and we assigned them to the surface (dangling, bridging) to interstitial oxygen bonding transformations, as confirmed by *in situ* Raman spectroscopy.

Bandgap engineering by native oxides has been proposed recently in theoretical works[34]. Here we have shown for the first time experimentally, how the oxidation processes can improve the band alignment between Ti/Au electrodes and exfoliated black phosphorus for transducer applications.

New evidence on the relative stability of the surface oxide over the planar has been presented. The surface oxides are the primary outcome of the few-layers black phosphorus oxidation and the transition to the planar configuration requires additional energy. The surface to planar transition starts at 373 K in agreement with the thermally activated electric conduction measurements and previous results[172]. This phosphorene oxide transition temperature is yet another operational limit to be considered in future applications of exfoliated black phosphorus, as the electronic structure is modified and can alter the response of transducer applications.

We proved that the activation energy for thermally activated electric conduction a good quantitative measure of oxidation processes[172]. The methodology shown here could be useful

for the evaluation of passivated/functionalized few-layers black phosphorus, as the transition would not be possible in perfectly pristine materials. The activation energy for thermally activated electric conduction for surface oxides (79 meV) was 40 times lower than for planar oxides (3,295 meV).

V.5 Authorship declaration

This chapter contains published work. No part of this work has been submitted for any other degree or diploma. The published information can be found under the following references:

J. Gómez-Pérez, D.G. Dobó, K.L. Juhász, A. Sápi, H. Haspel, Á. Kukovecz, Z. Kónya. Photoelectrical response of mesoporous nickel oxide decorated with size controlled platinum nanoparticles under argon and oxygen gas. Catal Today, vol. 284, pp. 37–43, 2016.

J. Gómez-Pérez, B. Barna, I. Y. Tóth, Z. Kónya, and Á. Kukovecz, "Quantitative tracking of the oxidation of black phosphorus in the few-layers regime," ACS Omega, vol. 3, pp. 12482–12488, 2018.

VI. Summary

My doctoral research work was focused on the exfoliation of few-layer black phosphorous flakes and on understanding their oxidation behavior. My key findings are summarized below by answering the questions put forth in section III (Aim and scope).

- *What is the topographical effect of replacing high boiling point solvents (NMP) for acetone during the liquid phase exfoliation process?*

The selection of the solvent for liquid phase exfoliation has an impact on the quality of the obtained materials. NMP has some disadvantages for the liquid phase exfoliation of black phosphorus, mainly the occurrence of oligomerization by-products that can contaminate the exfoliated materials and its high boiling point that requires high temperatures to remove the residual solvent from the surface of the flakes. While exfoliation with acetone requires longer sonication periods, it makes the removal of the residues possible without exposing the material to dangerously high temperatures where oxidation becomes the most important limitation.

Acetone-exfoliated black phosphorus exhibits optical bandgaps between 1.4 eV and 2.2 eV in agreement with the flake thicknesses in the range of 0.5 nm to 2 nm according to our AFM measurements. There is a linear correlation between the length and thickness of acetone-exfoliated phosphorene flakes that can be exploited for the rapid characterization of suspensions by measuring the hydrodynamic size with DLS. Hydrodynamic size characterization is less time consuming than AFM characterization and more representative than TEM imaging as it yields size distributions beyond the bias of the operator.

- *What are the correlations between the topographical and the Raman spectral features?*

The Raman spectral features applicable for the identification of the few-layers black phosphorus were debated and the blueshift of the Raman-active vibrational modes was not

fully accepted in the literature. In this work, not only the blueshift was confirmed but other distinctive features were described, for instance: thinner samples have higher thermal expansion coefficients calculated for the A_g^1, B_{2g} and A_g^2 vibrational modes (see **Table 7**), and centrifugation induces a blueshift of the harmonic phonon frequency at 0 K in all three vibrational modes. The discrepancy about the blueshift in other reports might have been caused by other external effects like oxidation and mechanical strain between the exfoliated materials and the substrates.

- *How can the oxidation process of few-layers black phosphorus be tracked using Raman spectroscopy?*

Thermogravimetric analysis (TGA and DSC) is widely used to assess the temperature dependence of the oxidation process. However, these techniques are more suitable for bulky materials and less adequate for investigating very thin phosphorene flakes. The newly devised set up depicted in **Figure 32** allows *in situ* Raman measurements during heating or cooling, therefore, it facilitated the investigation of the temperature dependence of the vibrational modes of exfoliated materials. From the temperature dependence of the Raman spectrum it was possible to correlate the oxidation process with anomalous behaviors in the thermal expansion of the lattice. A mechanism based on currently available computational studies for pristine and oxidized materials was proposed to explain the deformations.

The phosphorene oxide transitions demonstrated here are novel in the literature of few-layers black phosphorus and could be exploited as an evaluation tool for assessing the extent of oxidation and functionalization of black phosphorus. The new method relies on the finding that the transition requires the presence of dangling substituents, because otherwise, the thermal lattice expansion would follow the expected trends of pristine materials.

- *What is the correlation between Raman spectral features and the oxidation of black phosphorus?*

Previously, Raman spectroscopy was proposed as a characterization technique to describe the oxidation state of black phosphorus on the basis of various spectral features (i.e. decreased the intensity of the A_g^1/ A_g^2 ratio[31,45,53], diminished overall Raman intensity, and the

emergence of a broad band between the B_{2g} and A_g^2 vibrational modes). Some of the previously described methods do not have appropriate mechanistic support to explain the oxidation processes in few-layers black phosphorus, therefore, a new approach was required for the evaluation of oxidation or functionalization in the few-layers regime.

Taking advantage of the crystallographically oriented vibrational modes and the strong anisotropy of black phosphorus, it was possible to determine the phase transition temperature between surface oxides and planar oxides for the first time in literature. The lattice deformation of few-layers black phosphorus by oxidation was studied in several computational works, but our work[172] was the first experimental study to take advantage of this phenomenon to characterize the oxidation process.

– *What is the thermal stability of partially oxidized few-layers black phosphorus?*

Surface oxides with a low concentration of chemically-bonded oxygen are dominant below 373 K. A higher concentration of chemically bonded oxygen is incorporated with dominance of surface oxide between 373 K and 493 K. At approx. 493 K, the surface to planar oxide transition takes place, which is characterized by lattice deformation in the stacking direction perpendicular to the plane. Planar oxides are present between 493 K and 673 K, then sublimation starts at approx. 673 K. Note that defects and impurities can affect the precise temperature values because they lower the activation energy of oxidation reactions.

– *What is the primary outcome of oxidation of few-layers black phosphorus?*

Our FTIR measurements have confirmed the presence of several types of phosphorus oxides in highly oxidized samples. These results resolve the controversy in recent computational works about assigning the stability of metastable oxides at near-equilibrium conditions. Our results[164,172] suggest that the primary oxidation products are surface oxides because of the smaller to none deformation of the lattice structure upon exposure to oxygen gas and temperature. Additionally, a temperature-controlled transition between the surface and planar oxides may be interpreted as a thermodynamic energy barrier between the two phases, and for lower concentrations, it would be an indication of the relative stability. The

latter is supported by cyclic XRD measurements at room temperature and cyclic *in situ* Raman measurements that demonstrate the reversibility of the surface-planar-surface transitions and provide strong evidence for the higher stability of surface oxides.

- *In practical terms, what is the effect of oxidation on the black phosphorus/gold contact typically used in transducer applications?*

The effect of the phase transition in phosphorene oxides was studied for the gold-exfoliated black phosphorus contact using interdigitated electrodes. The results were coherent with recently published computational works and experimentally demonstrated the correlation between the electrical resistance and the oxidative processes. Furthermore, we proved that the oxidation process is accompanied by an increased electrical resistance, but once the endothermic phase transition is accomplished, the resistance drops as an indicator of the interstitial oxygen formation. This finding creates an opportunity to experimentally verify some recently published computational works regarding the semiconductor-to-metal transitions in few-layers black phosphorus with dangling substituents (Li/Na/Mg)[74].

VII. Összefoglalás

Doktori kutatásaim a néhány rétegű fekete foszfor lemezkék réteghámozásos előállítására és oxidációs tulajdonságaik megértésére irányultak. Legfontosabb eredményeimet a III. fejezetben feltett kérdések megválaszolásával az alábbiakban foglalom össze.

- *Milyen topográfiai hatása van a folyadékfázisú réteghámozási eljárásban használt magas forráspontú oldószer (NMP) acetonra cserélésének?*

A folyadékfázisú réteghámozásnál használt oldószer fajtája hatással van az így nyerhető termékek minőségére. A fekete foszfor réteghámozására használatos NMP fontosabb hátrányai a terméket potenciálisan elszennyező oligomer melléktermékek megjelenésének lehetősége, valamint az, hogy az NMP magas forráspontja miatt csak magas hőmérsékleten távolítható el az összes oldószermaradvány a lemezkékről. Bár az acetonos hámozás hosszabb ultrahangos kezelést igényel, az így nyerhető anyagról az oldószermaradvány eltávolítható anélkül, hogy a terméket az oxidációs határhoz közeli, veszélyesen magas hőmérsékletre kellene felmelegíteni.

Az acetonos réteghámozással készített fekete foszfor optikai tiltott sáv szélessége 1,4 eV és 2,2 eV közötti, ami 0,5 nm és 2,0 nm közötti lemezke rétegvastagságra utal, jó egyezést mutatva az AFM mérések eredményével. Az acetonban réteghámozott foszforén lemezkék hossza és vastagsága között egyenes arányosság van, ami jól kihasználható arra, hogy a lemezkesokaság átlagos méretét a gyors DLS módszerrel határozzuk meg. Ez a hidrodinamikai átmérő mérés kevésbé időigényes az AFM-nél, és reprezentatívabb pl. a TEM-nél, hiszen az utóbbi által szolgáltatott mérteloszlások jellemzően a mérést végző személy válogatási hibájával terheltek.

- *Hogyan függenek össze a topográfiai és a Raman spektroszkópiai tulajdonságok?*

A néhány rétegű fekete foszfor azonosítására alkalmas Raman spektrális jellemzők az irodalomban vita tárgyát képezték, csakúgy, mint a Raman-aktív rezgésekhez tartozó sávok méretfüggő kékeltolódása. Munkámban nem csak ezt a kékeltolódást bizonyítottam, hanem további megkülönböztető jellemzőket is leírtam. Ezek: (i) a vékonyabb minták A_g^1, B_{2g} és A_g^2 rezgési módusainak a vastagabbakénál nagyobb a hőmérsékleti expanziós tényezője, és (ii) centrifugálással a harmonikus fononfrekvencia kékeltolódása idézhető elő mindhárom módus esetében. Véleményem szerint a korábbi munkákban a kékeltolódást illetően tapasztalható diszkrepanciák oxidációnak, vagy a réteghámozott anyag és a szubsztrát közötti mechanikai feszültség hatásának tulajdoníthatók.

- *Hogyan követhető a néhány rétegű fekete foszfor oxidációja Raman spektroszkópiával?*

A termoanalitikát (TGA és DSC) széles körben alkalmazzák az oxidációs folyamatok hőmérsékletfüggésének vizsgálatára, ám ezek a módszerek inkább a tömbfázis jellemzésére valók, és kevésbé megfelelők a nagyon vékony foszforén lemezkékhez. Az 31. ábrán bemutatott új kísérleti elrendezésemmel a Raman méréseket fűtés és hűtés közben, in situ is el tudtam végezni, így segítségével a réteghámozott anyagok rezgési módusainak hőmérsékletfüggése vizsgálhatóvá vált. A Raman spektrum hőmérsékletfüggése alapján sikerült a rács termikus expanziójában tapasztalható anomáliákat az oxidációs folyamatokkal korreláltatni. Az eredeti és az oxidált anyagokra ma elérhető modellszámításokra alapozva sikerült mechanizmust javasolnunk a deformációk magyarázatára is.

Az itt bemutatott foszforén oxidációs átmenetek néhány rétegű fekete foszforra nézve újdonságnak számítanak az irodalomban, és kihasználhatónak tűnnek a fekete foszfor oxidáltsági szintjének és funkcionalizáltságának jellemzésére. Az új módszer lényege, hogy az átmenet a szabad szubsztituensek jelenlétét feltételezi, ugyanis ezek hiányában a termikus rácsexpanzió a kezeletlen anyagokra várt trendet mutatná oxidáció esetén is.

- *Milyen összefüggés van a Raman spektrális jellemzők és a fekete foszfor oxidációja között?*

A Raman spektroszkópiát már korábban is alkalmas technikának vélték a fekete foszfor oxidáltsági állapotának jellemzésére például (i) a csökkenő A_g^1/ A_g^2 arány[31,45,53], (ii) a

csökkenő teljes spektrális intenzitás, és (iii) a B_{2g} és A_g^2 rezgési módok között megjelenő széles új sáv alapján. E módszerek némelyike nem bír kellő elméleti megalapozottsággal a néhány rétegű fekete foszfor oxidációs folyamatainak magyarázata szempontjából, ezért új megközelítést kellett kidolgoznunk az oxidáció és a funkcionalizálás értékelésére. A krisztallográfiailag irányított rezgési módok és a fekete foszfor jelentős anizotrópiájának kihasználásával az irodalomban elsőként tudtuk meghatározni a felületi és a síkbeli oxidok közötti fázisátmenet hőmérsékletét. Az oxidáció okozta rácstorzulást a néhány rétegű fekete foszforban már több számításos munka is vizsgálta, de mi voltunk az elsők[172], akik a jelenséget az oxidációs folyamat jellemzésére tudtuk kísérletileg kihasználni.

    –   *Milyen a részlegesen oxidált néhány rétegű fekete foszfor termikus stabilitása?*

373 K alatti hőmérsékleten a kémiailag kötött oxigént csak alacsony koncentrációban tartalmazó felületi oxidok a jellemzők, majd 373 K és 493 K között a felületi oxid dominanciájának megtartása mellett a kémiailag kötött oxigén koncentrációja nő. Nagyjából 493 K-en megtörténik a felületi oxidból síkbeli oxidba történő fázisátmenet, ami a lemezre normális irányban rácstorzulással jár. 493 és 673 K között a síkbeli oxidok a jellemzők, majd kb. 673 K-en megindul a szublimáció. Megjegyzendő, hogy a hibahelyek és szennyezések jelenléte a pontos hőmérséklet értékeket eltolhatja, mivel azok az oxidációs reakciók aktiválási energiáját csökkentik.

    –   *Mi a néhány rétegű fekete foszfor elsődleges oxidációs terméke?*

Erősen oxidált mintákban FT-IR spektroszkópiás mérésekkel többféle foszfor-oxid jelenlétét is ki tudtuk mutatni. Ezek az eredmények segíthetnek feloldani azokat az irodalmi ellentmondásokat, amelyek egyes friss számításos munkákban az egyensúlyközeli állapotú metastabilis oxidok stabilitásához kapcsolódnak. Eredményeink[164,172] szerint az elsődleges oxidációs termékek felületi oxidok, amik az oxigénnek és emelt hőmérsékletnek kitett fekete foszforban a rács legfeljebb elhanyagolható mértékű torzulása közben keletkeznek.

A tényt, hogy a felületi és a síkbeli oxidot hőmérsékletvezérelt átalakulás választja el egymástól, értelmezhetjük úgy, mint a két fázis között termodinamikai energiagát létének igazolását. A felületi oxidok nagyobb stabilitására a felületi-síkbeli-felületi átmenet

revezibilitása a bizonyíték, amit ciklikus XRD és in situ Raman spektroszkópiai mérésekkel is igazoltunk.

- *Mik az oxidáció lehetséges gyakorlati hatásai a fekete foszfor / arany rendszerben?*

A foszforén oxidok fázisátalakulásának az elektromos vezetőképességre gyakorolt hatását az arany – réteghámozott fekete foszfor kontaktuson tanulmányoztuk fésűelektróda elrendezésben. Eredményeink összhangban voltak a legfrissebb elméleti munkákkal, és kísérletileg igazolták, hogy az elektromos ellenállás és az oxidatív folyamatok összefüggenek. Megmutattuk továbbá, hogy az oxidációt először növekvő elektromos ellenállás kíséri, majd az endoterm folyamat végeztével az elektromos ellenállás lecsökken, így jelezve az intersticiális oxigén kialakulását. Ennek alapján lehetséges lesz kísérletileg bizonyítani azt a mostanában publikált elméleti feltételezést, hogy a néhány rétegű fekete foszforban Li/Na/Mg szubsztituensekkel megvalósítható a félvezető–fém átmenet[74].

VIII. Acknowledgment

First, I want to thank my family for the support and understanding during the whole process. Without their patience and emotional support, everything would have been much more difficult.

I want to thank prof. Kónya Zoltán and prof. Kukovecz Ákos for receiving me in their group. Thanks for the academic and personal support during the last four years.

I want to thank my colleagues at the Department of Applied and Environmental Chemistry for the teachings and friendships that kept me motivated and allowed me to grow as a person and as a researcher.

Finally, I want to thank Colciencias for the scholarship.

IX. References

1. Novoselov KS, Geim AK, Morozov SV, Jiang D, Zhang Y, Dubonos SV, et al. Electric field effect in atomically thin carbon films. *Science*. **2004**,*306*(*5696*),666–9.

2. Harada Y, Murano K, Shirotani I, Takahashi T, Maruyama Y. Electronic structure of black phosphorus studied by X-ray photoelectron spectroscopy. *Solid State Commun*. **1982**,*44*(*6*),877–9.

3. Takahashi T, Shirotani I, Suzuki S, Sagawa T. Band structure of black phosphorus studied by angle-resolved ultraviolet photoemission spectroscopy. *Solid State Commun*. **1983**,*45*(*11*),945–8.

4. Badami DV. X-Ray studies of graphite formed by decomposing silicon carbide. *Carbon N Y*. **1965**,*3*(*1*),53–7.

5. Iacopi F, Boeckl JJ, Jagadish C. Semiconductors and semimetals. 2D materials. 1st ed. Jagadish C, Weber ER, editors. Cambridge, USA: Elsevier Inc.; 2016.

6. Gibney E. 2D or not 2D. *Nature*. **2015**,*522*(*7556*),274–6.

7. Golias E, Krivenkov MS, Varykhalov AY, Sánchez-barriga J, Rader O. Band Renormalization of Blue Phosphorus on Au (111). *Nano Lett*. **2018**,*18*(*111*),6672–6678.

8. Zhang JL, Zhao S, HAn C, Zhunzhun W, Zhong S, Sun S, et al. Epitaxial Growth of Single Layer Blue Phosphorus: A New Phase of Two-Dimensional Phosphorus. *Nano Lett*. **2016**,*16*(*8*),4903–4908.

9. Zhu Z, Tománek D. Semiconducting Layered Blue Phosphorus : A Computational Study. *Phys Rev Lett*. **2014**,*112*,176802–5.

10. Dhanabalan SC, Ponraj JS, Guo Z, Li S, Bao Q, Zhang H. Emerging Trends in Phosphorene Fabrication towards Next Generation Devices. *Adv Sci*. **2017**,*1600305*.

11. Lu SB, Miao LL, Guo ZN, Qi X, Zhao CJ, Zhang H, et al. Broadband nonlinear optical response in multi-layer black phosphorus: an emerging infrared and mid-infrared optical material. *Opt Express*. **2015**,*23*(*9*),11183–94.

12. Dai J, Zeng XC. Bilayer phosphorene: Effect of stacking order on bandgap and its potential applications in thin-film solar cells. *J Phys Chem Lett*. **2014**,*5*(*7*),1289–93.

13. Liu H, Neal AT, Zhu Z, Luo Z, Xu X, Tománek D, et al. Phosphorene: An Unexplored 2D Semiconductor with a High Hole. *ACS Nano*. **2014**,*8*(*4*),4033–41.

14. Nilges T. Expressway to partially oxidized phosphorene. *Proc Natl Acad Sci U S A*.

2018,201804079.

15. Ling X, Wang H, Huang S, Xia F, Dresselhaus MS, Lau J. The renaissance of black phosphorus. *Pnas*. **2015**,*112*,4523.

16. Peng LM, Zhang Z, Wang S, Liang X. A doping-free approach to carbon nanotube electronics and optoelectronics. *AIP Adv*. **2012**,*2*(*4*),0–14.

17. Lv W, Yang B, Wang B, Wan W, Ge Y, Yang R, et al. Sulfur-Doped Black Phosphorus Field-Effect Transistors with Enhanced Stability. *ACS Appl Mater Interfaces*. **2018**,*10*(*11*),9663–9668.

18. Buscema M, Groenendijk DJ, Blanter SI, Steele GA, Van Der Zant HSJ, Castellanos-Gomez A. Fast and broadband photoresponse of few-layer black phosphorus field-effect transistors. *Nano Lett*. **2014**,*14*(*6*),3347–52.

19. Tian B, Tian B, Smith B, Scott MC, Lei Q, Hua R, et al. Facile bottom-up synthesis of partially oxidized black phosphorus nanosheets as metal-free photocatalyst for hydrogen evolution. *Proc Natl Acad Sci*. **2018**,*115*(*17*),4345–50.

20. Abbas AN, Liu B, Chen L, Ma Y, Cong S, Aroonyadet N, et al. Black phosphorus gas sensors. *ACS Nano*. **2015**,*9*(*5*),5618–24.

21. Lee G, Kim S, Jung S, Jang S, Kim J. Suspended black phosphorus nanosheet gas sensors. *Sensors Actuators, B Chem*. **2017**,*250*(*2017*),569–73.

22. Cui S, Pu H, Wells SA, Wen Z, Mao S, Chang J, et al. Ultrahigh sensitivity and layer-dependent sensing performance of phosphorene-based gas sensors. *Nat Commun*. **2015**,*6*,8632.

23. Hanlon D, Backes C, Doherty E, Cucinotta CS, Berner NC, Boland C, et al. Liquid exfoliation of solvent-stabilized few-layer black phosphorus for applications beyond electronics. *Nat Commun*. **2015**,*6*,8563.

24. Late DJ. Liquid exfoliation of black phosphorus nanosheets and its application as humidity sensor. *Microporous Mesoporous Mater*. **2016**,*225*(*2016*),494–503.

25. Yao Y, Zhang H, Sun J, Ma W, Li L, Li W, et al. Novel QCM humidity sensors using stacked black phosphorus nanosheets as sensing film. *Sensors Actuators, B Chem*. **2017**,*244*(*2017*),259–64.

26. Yasaei P, Behranginia A, Foroozan T, Kim K, Khalili-araghi F, Salehi-khojin A. Stable and selective humidity sensing using stacked black phosphorus flakes. *ACS Nano*. **2015**,(*10*),9898–905.

27. Li P, Zhang D, Jiang C, Zong X, Cao Y. Ultra-sensitive suspended atomically thin-layered black phosphorus mercury sensors. *Biosens Bioelectron*. **2017**,*98*(*June*),68–75.

28. Chen Y, Ren R, Pu H, Chang J, Mao S, Chen J. Field-effect transistor biosensors with

two-dimensional black phosphorus nanosheets. *Biosens Bioelectron*. **2017**,*89*(*2017*),505–10.

29. Uk Lee H, Lee SC, Won J, Son BC, Choi S, Kim Y, et al. Stable semiconductor black phosphorus (BP)@titanium dioxide (TiO2) hybrid photocatalysts. *Sci Rep*. **2015**,*5*,1–6.

30. Rahman MZ, Kwong CW, Davey K, Qiao SZ. 2D phosphorene as a water splitting photocatalyst: fundamentals to applications. *Energy Environ Sci*. **2016**,*9*(*4*),1513–4.

31. Abellán G, Wild S, Lloret V, Scheuschner N, Gillen R, Mundloch U, et al. Fundamental Insights into the Degradation and Stabilization of Thin Layer Black Phosphorus. *J Am Chem Soc*. **2017**,*139*(*30*),10432–40.

32. Ziletti A, Carvalho A, Campbell DK, Coker DF, Castro Neto AH. Oxygen defects in phosphorene. *Phys Rev Lett*. **2015**,*114*(*4*),26–9.

33. Edmonds MT, Tadich A, Carvalho A, Ziletti A, O'Donnell KM, Koenig SP, et al. Creating a stable oxide at the surface of black phosphorus. *ACS Appl Mater Interfaces*. **2015**,*7*(*27*),14557–62.

34. Ziletti A, Carvalho A, Trevisanutto PE, Campbell DK, Coker DF, Castro Neto AH. Phosphorene oxides: Bandgap engineering of phosphorene by oxidation. *Phys Rev B*. **2015**,*91*,085407.

35. Wang C-X, Zhang C, Jiang J-W, Rabczuk T. The Effects of Vacancy and Oxidation on Black Phosphorus Nanoresonators. *Nanotechnology*. **2017**,*28*,135202.

36. Lei W, Liu G, Zhang J, Liu M. Black phosphorus nanostructures: Recent advances in hybridization, doping and functionalization. *Chem Soc Rev*. **2017**,*46*(*12*),3492–509.

37. Bridgman PW. Two New Modifications of Phosphorus. *J Am Chem Soc*. **1914**,*36*(*7*),1344–63.

38. Tiouitchi G, Ali MA, Benyoussef A, Hamedoun M, Lachgar A, Benaissa M, et al. An easy route to synthesize high-quality black phosphorus from amorphous red phosphorus. *Mater Lett*. **2019**,*236*(*October*),56–9.

39. Wang S, Chen N, Jiang Q, Dai L, Xu L, Zhang H. Facile Synthesis of Black Phosphorus: an Efficient Electrocatalyst for the Oxygen Evolving Reaction. *Angew Chemie Int Ed*. **2016**,*55*(*44*),13849–53.

40. Haick PH. Nanotechnology and Nanosensors. Introduction to Nanotechnology. Haifa, Israel: Technion. Israel Institute of Technology; 2013. 129 p.

41. Yu P, Cardona M. Fundamentals of semiconductors. Physics and materials properties. 4th ed. 2010.

42. Cai Y, Zhang G, Zhang Y-W. Layer-dependent band alignment and work function of few-layer phosphorene. *Sci Rep*. **2014**,*4*(*2016*),6677.

43. Wang G, Pandey R, Karna SP. Physics and chemistry of oxidation of two-dimensional nanomaterials by molecular oxygen. *Wiley Interdiscip Rev Comput Mol Sci*. **2017**,*7*(*e1280*).

44. Boukhvalov DW, Rudenko AN, Prishchenko DA, Mazurenko VG, Katsnelson MI. Chemical modifications and stability of phosphorene with impurities: a first principles study. *Phys Chem Chem Phys*. **2015**,*17*(*23*),15209–17.

45. Favron A, Gaufres E, Fossard F, Phaneuf-L'Heureux A-L, Tang NY-W, Levesque PL, et al. Photooxidation and quantum confinement effects in exfoliated black phosphorus. *Nat Mater*. **2015**,*14*(*8*),826–32.

46. Abellán G, Lloret V, Mundloch U, Marcia M, Neiss C, Görling A, et al. Noncovalent Functionalization of Black Phosphorus. *Angew Chemie - Int Ed*. **2016**,*55*(*47*),14557–62.

47. Island JO, Steele GA, Zant HSJ Van Der, Castellanos-Gomez A. Environmental instability of few-layer black phosphorus. *2D Mater*. **2015**,*2*(*1*).

48. Hultgren R, Gingrich NS, Warren BE. The atomic distribution in red and black phosphorus and the crystal structure of black phosphorus. *J Chem Phys*. **1935**,*3*(*6*),351–5.

49. Villegas CEP, Rocha AR, Marini A. Anomalous Temperature Dependence of the Band Gap in Black Phosphorus. *Nano Lett*. **2016**,*16*(*8*),5095–101.

50. Liu X, Wood JD, Chen KS, Cho E, Hersam MC. In situ thermal decomposition of exfoliated two-dimensional black phosphorus. *J Phys Chem Lett*. **2015**,*6*(*5*),773–8.

51. Lewis IR, Edwards HG. Handbook of Raman Spectroscopy. From the research laboratory to the process line. Lewis IR, Edwards HG, editors. New York: Taylor & Francis Group, LLC; 2001. 1049 p.

52. Piprek J. Semiconductor Optoelectronic Devices. Introduction to physics and Simulation. Academic Press; 2005. 234 p.

53. Ribeiro HB, Pimenta MA, de Matos CJS. Raman spectroscopy in black phosphorus. *J Raman Spectrosc*. **2017**,(*2017*),76–90.

54. Lee HU, Park SY, Lee SC, Choi S, Seo S, Kim H, et al. Black Phosphorus (BP) Nanodots for Potential Biomedical Applications. *Small*. **2016**,*12*(*2*),214–9.

55. Lee S, Yang F, Suh J, Yang S, Lee Y, Li G, et al. Anisotropic in-plane thermal conductivity of black phosphorus nanoribbons at temperatures higher than 100 K. *Nat Commun*. **2015**,*6*,1–7.

56. Ling X, Liang L, Huang S, Puretzky AA, Geohegan DB, Sumpter BG, et al. Low-Frequency Interlayer Breathing Modes in Few-Layer Black Phosphorus. *Nano Lett*. **2015**,*15*(*6*),4080–8.

57.   Dong S, Zhang A, Liu K, Ji J, Ye YG, Luo XG, et al. Ultralow-Frequency Collective Compression Mode and Strong Interlayer Coupling in Multilayer Black Phosphorus. *Phys Rev Lett*. **2016**,*116*(*8*),087401.

58.   Doganov RA, O'Farrell ECT, Koenig SP, Yeo Y, Ziletti A, Carvalho A, et al. Transport properties of pristine few-layer black phosphorus by van der Waals passivation in an inert atmosphere. *Nat Commun*. **2015**,*6*,6647.

59.   Wood JD, Wells S a, Jariwala D, Chen K, Cho E, Sangwan VK, et al. Effective Passivation of Exfoliated Black Phosphorus Transistors against Ambient Degradation. *Nano Lett*. **2014**,*14*(*12*),6964–6970.

60.   Takao Y, Morita A. Electronic structure of black phosphorus: Tight binding approach. *Phys B+C*. **1981**,*105*(*1–3*),93–8.

61.   Tran V, Soklaski R, Liang Y, Yang L. Tunable Band Gap and Anisotropic Optical Response in Few-layer Black Phosphorus. *Phys Rev B*. **2014**,*235319*(*June*),1–6.

62.   Castellanos-Gomez A, Vicarelli L, Prada E, Island JO, Narasimha-Acharya KL, Blanter SI, et al. Isolation and characterization of few-layer black phosphorus. *2D Mater*. **2014**,*1*(*2*),025001.

63.   Zhang G, Huang S, Chaves A, Song C, Özçelik VO, Low T, et al. Infrared fingerprints of few-layer black phosphorus. *Nat Commun*. **2017**,*8*,14071.

64.   Liang L, Wang J, Lin W, Sumpter BG, Meunier V, Pan M. Electronic Bandgap and Edge Reconstruction in Phosphorene Materials. *Nano Lett*. **2014**,*14*(*11*),6400–6.

65.   Woomer AH, Farnsworth TW, Hu J, Wells RA, Donley CL, Warren SC. Phosphorene: Synthesis, Scale-Up, and Quantitative Optical Spectroscopy. *ACS Nano*. **2015**,*9*(*9*),8869–84.

66.   Lu J, Yang J, Carvalho A, Liu H, Lu Y, Sow CH. Light-Matter Interactions in Phosphorene. *Acc Chem Res*. **2016**,*49*(*9*),1806–15.

67.   Ryder CR, Wood JD, Wells SA, Yang Y, Jariwala D, Marks TJ, et al. Covalent functionalization and passivation of exfoliated black phosphorus via aryl diazonium chemistry. *Nat Chem*. **2016**,*8*,597–602.

68.   Li L, Yu Y, Ye GJ, Ge Q, Ou X, Wu H, et al. Black phosphorus field-effect transistors. *Nat Nanotechnol*. **2014**,*9*(*5*),372–7.

69.   Cao Y, Mishchenko A, Yu GL, Khestanova E, Rooney AP, Prestat E, et al. Quality Heterostructures from Two-Dimensional Crystals Unstable in Air by Their Assembly in Inert Atmosphere. *Nano Lett*. **2015**,*15*(*8*),4914–21.

70.   Kim M, Kim H, Park S, Kim JS, Choi HJ, Im S, et al. Intrinsic correlation between electronic structure and degradation: from few layers to bulk black phosphorus. *Angew Chemie Int Ed*. **2019**,*131*.

71. Bai L, Wang X, Tang S, Kang Y, Wang J, Yu Y, et al. Black Phosphorus/Platinum Heterostructure: A Highly Efficient Photocatalyst for Solar-Driven Chemical Reactions. *Adv Mater*. **2018**,*30*(*40*).

72. Cho SY, Lee Y, Koh HJ, Jung H, Kim JS, Yoo HW, et al. Superior Chemical Sensing Performance of Black Phosphorus: Comparison with MoS2 and Graphene. *Adv Mater*. **2016**,*28*,7020–8.

73. Zhou S, Liu N, Zhao J. Phosphorus quantum dots as visible-light photocatalyst for water splitting. *Comput Mater Sci*. **2017**,*130*(*2017*),56–63.

74. Sibari A, El Marjaoui A, Lakhal M, Kerrami Z, Kara A, Benaissa M, et al. Phosphorene as a promising anode material for (Li/Na/Mg)-ion batteries: A first-principle study. *Sol Energy Mater Sol Cells*. **2018**,*180*(*March*),253–7.

75. Zhang J, Liu X, Neri G, Pinna N. Nanostructured Materials for Room-Temperature Gas Sensors. *Adv Mater*. **2015**,795–831.

76. Sapi A, Liu F, Cai X, Thompson CM, Wang H, An K, et al. Comparing the Catalytic Oxidation of Ethanol at the Solid–Gas and Solid–Liquid Interfaces over Size-Controlled Pt Nanoparticles: Striking Differences in Kinetics and Mechanism. *Nano Lett*. **2014**,*14*(*11*),6727–30.

77. Wang H, Sapi A, Thompson CM, Liu F, Zherebetskyy D, Krier JM, et al. Dramatically Different Kinetics and Mechanism at Solid/Liquid and Solid/Gas Interfaces for Catalytic Isopropanol Oxidation over Size- Controlled Platinum Nanoparticles. *J Am Chem Soc*. **2014**,*136*,10515–20.

78. Hailiang W, An K, Sapi A, Liu F, Somorjai GA. Effects of Nanoparticle Size and Metal/Support Interactions in Pt-Catalyzed Methanol Oxidation Reactions in Gas and Liquid Phases. *Catal Letters*. **2014**,*144*(*11*),1930–8.

79. Wang H, Wang Y, Zhu Z, Sapi A, An K, Kennedy G, et al. Influence of Size-Induced Oxidation State of Platinum Nanoparticles on Selectivity and Activity in Catalytic Methanol Oxidation in the Gas Phase. *Nano Lett*. **2013**,*13*(*6*),2976–9.

80. Pushkarev V, An K, Alayoglu S, Beaumont S, Somorjai G. Hydrogenation of benzene and toluene over size controlled Pt/SBA-15 catalysts: Elucidation of the Pt particle size effect on reaction kinetics. *J Catal*. **2012**,*292*,64–72.

81. Kmetykó Á, Mogyorósi K, Gerse V, Kónya Z, Pusztai P, Dombi A, et al. Photocatalytic H2 Production Using Pt-TiO2 in the Presence of Oxalic Acid: Influence of the Noble Metal Size and the Carrier Gas Flow Rate. *Materials (Basel)*. **2014**,*7*(*10*),7022–38.

82. Gómez-Pérez J, Dobó DG, Juhász KL, Sápi A, Haspel H, Kukovecz Á, et al. Photoelectrical response of mesoporous nickel oxide decorated with size controlled platinum nanoparticles under argon and oxygen gas. *Catal Today*. **2016**,*284*,37–43.

83. Balázs Réti, Major Z, Szarka D, Boldizsár T, Horváth E, Magrez A, et al. Influence of

TiO2 phase composition on the photocatalytic activity of TiO2/MWCNT composites prepared by combined sol–gel/hydrothermal method. *J Mol Catal A Chem*. **2016**,140–7.

84.   Choi JM, Byun JH, Kim SS. Influence of grain size on gas-sensing properties of chemiresistive p-type NiO nanofibers. *Sensors Actuators, B Chem*. **2016**,*227*(*2016*),149–56.

85.   Shen GH, Hong FCN. Ultraviolet photosensors fabricated with Ag nanowires coated with ZnO nanoparticles. *Thin Solid Films*. **2014**,*570*(*PB*),363–70.

86.   Wang G, Pandey R, Karna SP. Phosphorene oxide: Stability and electronic properties of a novel two-dimensional material. *Nanoscale*. **2015**,*7*(*2*),524–31.

87.   Wang J, Wei L, Zhang L, Jiang C, Siu-Wai Kong E, Zhang Y. Preparation of high aspect ratio nickel oxide nanowires and their gas sensing devices with fast response and high sensitivity. *J Mater Chem*. **2012**,*22*(*17*),8327.

88.   Kc S, Longo RC, Wallace RM, Cho K. Surface oxidation energetics and kinetics on MoS2 monolayer. *J Appl Phys*. **2015**,*117*(*13*).

89.   Zhao Y, Wu X, Yang J, Zeng XC. Oxidation of a two-dimensional hexagonal boron nitride monolayer: A first-principles study. *Phys Chem Chem Phys*. **2012**,*14*(*16*),5545–50.

90.   Van Druenen M, Davitt F, Collins T, Glynn C, O'Dwyer C, Holmes JD, et al. Covalent Functionalization of Few-Layer Black Phosphorus Using Iodonium Salts and Comparison to Diazonium Modified Black Phosphorus. *Chem Mater*. **2018**,*30*(*14*),4667–74.

91.   Ryder CR, Wood JD, Wells SA, Yang Y, Jariwala D, Marks TJ, et al. Covalent functionalization and passivation of exfoliated black phosphorus via aryl diazonium chemistry. *Nat Chem*. **2016**,*8*,597–602.

92.   Wild S, Lloret V, Vega-Mayoral V, Vella D, Nuin E, Siebert M, et al. Monolayer black phosphorus by sequential wet-chemical surface oxidation. *RSC Adv*. **2019**,*9*(*7*),3570–6.

93.   Wang F, Zhang G, Huang S, Song C, Wang C, Xing Q, et al. Electronic structures of air-exposed few-layer black phosphorus by optical spectroscopy. *Phys Rev B*. **2019**,*99*(*7*),075427.

94.   Wild S, Fickert M, Mitrovic A, Lloret V, Neiss C, Vidal-Moya JA, et al. Lattice Opening Upon Bulk Reductive Covalent Functionalization of Black Phosphorus. *Angew Chemie Int Ed*. **2019**,.

95.   Marcia M, Hirsch A, Hauke F. Perylene-based non-covalent functionalization of 2D materials. *FlatChem*. **2017**,*1*,89–103.

96.   Dai J, Zeng XC. Structure and stability of two dimensional phosphorene with O or NH

functionalization. *RSC Adv*. **2014**,*4*(*89*),48017–21.

97. Wang CH, Yang CH, Chang JK. High-selectivity electrochemical non-enzymatic sensors based on graphene/Pd nanocomposites functionalized with designated ionic liquids. *Biosens Bioelectron*. **2017**,*89*(*2017*),483–8.

98. Kamath G, Baker G a. In silico free energy predictions for ionic liquid-assisted exfoliation of a graphene bilayer into individual graphene nanosheets. *Phys Chem Chem Phys*. **2012**,*14*,7929–33.

99. Mohl M, Dombovari A, Szabó M, Järvinen T, Pitkänen O, Sápi A, et al. Size-dependent H2 sensing over supported Pt nanoparticles. *J Nanosci Nanotechnol*. **2019**,*19*(*1*),459–64.

100. Kuriakose S, Taimur A, Balendhran S, Bansal V, Sriram S, Bhaskaran M, et al. Black phosphorus: Ambient degradation and strategies for protection. *2D Mater*. **2018**,*5*.

101. Kuntz KL, Wells RA, Hu J, Yang T, Dong B, Guo H, et al. Control of Surface and Edge Oxidation on Phosphorene. *ACS Appl Mater Interfaces*. **2017**,*9*(*10*),9126–35.

102. Pei J, Gai X, Yang J, Wang X, Yu Z, Choi D, et al. Producing air-stable monolayers of phosphorene and their defect engineering. *Nat Commun*. **2016**,*7*,1–8.

103. Gamage S, Li Z, Yakovlev VS, Lewis C, Wang H, Cronin SB, et al. Nanoscopy of Black Phosphorus Degradation. *Adv Mater Interfaces*. **2016**,*3*(*12*),1600121.

104. Zhang X-A, Ping Hu W, Neto AHC, Zhong S, Wu J, Chen W, et al. Surface transfer doping induced effective modulation on ambipolar characteristics of few-layer black phosphorus. *Nat Commun*. **2015**,*6*(*1*).

105. Kang J, Wells SA, Wood JD, Lee J, Liu X. Stable aqueous dispersions of optically and electronically active phosphorene. *Proceeding Natl Acad Sci*. **2016**,*113*(*42*),11688–93.

106. Kim J, Baek SK, Kim KS, Chang YJ, Choi EJ. Long-term stability study of graphene-passivated black phosphorus under air exposure. *Curr Appl Phys*. **2016**,*16*(*2*),165–9.

107. Son Y, Kozawa D, Liu AT, Koman VB, Wang QH, Strano MS. A study of bilayer phosphorene stability under MoS2-passivation. *2D Mater*. **2017**,*4*(*2*).

108. Zhao Y, Wang H, Huang H, Xiao Q, Xu Y, Guo Z, et al. Surface Coordination of Black Phosphorus for Robust Air and Water Stability. *Angew Chemie - Int Ed*. **2016**,*55*(*16*),5003–7.

109. Brent JR, Ganguli AK, Kumar V, Lewis DJ, McNaughter PD, O'Brien P, et al. On the stability of surfactant-stabilised few-layer black phosphorus in aqueous media. *RSC Adv*. **2016**,*6*(*90*),86955–8.

110. Alsaffar F, Alodan S, Alrasheed A, Alhussain A, Alrubaiq N, Abbas A, et al. Raman Sensitive Degradation and Etching Dynamics of Exfoliated Black Phosphorus. *Sci*

Rep. **2017**,*7*(*44540*),1–9.

111. Sun J, Lee H-W, Pasta M, Yuan H, Zheng G, Sun Y, et al. A phosphorene–graphene hybrid material as a high-capacity anode for sodium-ion batteries. *Nat Nanotechnol*. **2015**,*10*(*11*),980–5.

112. Kang J, Wood JD, Wells SA, Lee JH, Liu X, Chen KS, et al. Solvent exfoliation of electronic-grade, two-dimensional black phosphorus. *ACS Nano*. **2015**,*9*(*4*),3596–604.

113. Lee M, Roy AK, Jo S, Choi Y, Chae A, Kim B, et al. Exfoliation of black phosphorus in ionic liquids. *Nanotechnology*. **2017**,*28*(*12*).

114. Zhao W, Xue Z, Wang J, Jiang J, Zhao X, Mu T. Large-Scale, Highly Efficient, and Green Liquid-Exfoliation of Black Phosphorus in Ionic Liquids. *ACS Appl Mater Interfaces*. **2015**,*7*(*50*),27608–12.

115. Wang G, Slough WJ, Pandey R, Karna SP. Degradation of phosphorene in air: understanding at atomic level. *2D Mater*. **2016**,*3*(*025011*).

116. Shen J, He Y, Wu J, Gao C, Keyshar K, Zhang X, et al. Liquid Phase Exfoliation of Two-Dimensional Materials by Directly Probing and Matching Surface Tension Components. *Nano Lett*. **2015**,*15*(*8*),5449–54.

117. Bergin S, Sun Z, Rickard D, Streich P. Multicomponent solubility parameters for single-walled carbon nanotube− solvent mixtures Cited by me. *ACS Nano*. **2009**,*3*(*8*),2340–50.

118. Ambrosi A, Sofer Z, Pumera M. Electrochemical Exfoliation of Layered Black Phosphorus into Phosphorene. *Angew Chemie - Int Ed*. **2017**,*56*(*35*),10443–5.

119. Suryawanshi SR, More MA, Late DJ. Laser exfoliation of 2D black phosphorus nanosheets and their application as a field emitter. *RSC Adv*. **2016**,*6*(*113*),112103–8.

120. Nicolosi V, Chhowalla M, Kanatzidis MG, Strano MS, Coleman JN. Liquid Exfoliation of Layered Materials Liquid Exfoliation of Layered Materials. *Science (80-)*. **2013**,*340*(*June*),72–5.

121. Yasaei P, Kumar B, Foroozan T, Wang C, Asadi M, Tuschel D, et al. High-Quality Black Phosphorus Atomic Layers by Liquid-Phase Exfoliation. *Adv Mater*. **2015**,*27*(*11*),1887–92.

122. Zhang Y, Wang H, Luo Z, Tan HT, Li B, Sun S, et al. An Air-Stable Densely Packed Phosphorene–Graphene Composite Toward Advanced Lithium Storage Properties. *Adv Energy Mater*. **2016**,*6*(*12*),1–9.

123. Li D, Esau A, Jussila H, Ye G. Black phosphorus polycarbonate polymer composite for pulsed fiber lasers. *Appl Mater Today*. **2016**,*4*,17–23.

124. Yau HC, Bayazit MK, Steinke JHG, Shaffer MSP. Sonochemical degradation of N-

methylpyrrolidone and its influence on single walled carbon nanotube dispersion. *Chem Commun*. **2015**,*51*(*93*),16621–4.

125. Wei L, Chen F, Wang H, Zeng TH, Wang Q, Chen Y. Acetone-induced graphene oxide film formation at the water-air interface. *Chem - An Asian J*. **2013**,*8*(*2*),437–43.

126. Yi M, Shen Z, Zhang X, Ma S. Achieving concentrated graphene dispersions in water/acetone mixtures by the strategy of tailoring Hansen solubility parameters. *J Phys D Appl Phys*. **2013**,*46*(*2*),025301.

127. Guo Z, Zhang H, Lu S, Wang Z, Tang S, Shao J, et al. From Black Phosphorus to Phosphorene: Basic Solvent Exfoliation, Evolution of Raman Scattering, and Applications to Ultrafast Photonics. *Adv Funct Mater*. **2015**,*25*(*45*),6996–7002.

128. Jiang T, Yin K, Zheng X, Yu H, Cheng X-A. Black phosphorus as a new broadband saturable absorber for infrared passively Q-switched fiber lasers. *ArXiv*. **2015**,*4458*(*2014*),8.

129. Pan L, Zhu XD, Sun KN, Liu YT, Xie XM, Ye XY. Molecular level distribution of black phosphorus quantum dots on nitrogen-doped graphene nanosheets for superior lithium storage. *Nano Energy*. **2016**,*30*(*September*),347–54.

130. Zhang X, Xie H, Liu Z, Tan C, Luo Z, Li H, et al. Black phosphorus quantum dots. *Angew Chemie - Int Ed*. **2015**,*54*(*12*),3653–7.

131. Zheng X, Chen R, Shi G, Zhang J, Xu Z, Cheng X, et al. Characterization of nonlinear properties of black phosphorus nanoplatelets with femtosecond pulsed Z-scan measurements. *Opt Lett*. **2015**,*40*(*15*),3480–3.

132. Luo Z-C, Liu M, Guo Z-N, Jiang X-F, Luo A-P, Zhao C-J, et al. Microfiber-based few-layer black phosphorus saturable absorber for ultra-fast fiber laser. *Opt Express*. **2015**,*23*(*15*),20030.

133. Kong L, Qin Z, Xie G, Guo Z, Zhang H, Yuan P, et al. Black phosphorus as broadband saturable absorber for pulsed lasers from 1 μ m to 2.7 μ m wavelength. *Laser Phys Lett*. **2016**,*13*(*4*),045801.

134. Brent JR, Savjani N, Lewis EA, Haigh SJ, Lewis DJ, O'Brien P. Production of few-layer phosphorene by liquid exfoliation of black phosphorus. *Chem Commun*. **2014**,*50*(*87*),13338–41.

135. Gu W, Yan Y, Pei X, Zhang C, Ding C, Xian Y. Fluorescent Black Phosphorus Quantum Dots as Label-free Sensing probes for Evaluation of Acetylcholinesterase Activity Fluorescent Black Phosphorus Quantum Dots as Label-free Sensing probes for Evaluation of Acetylcholinesterase Activity. *Sensors Actuators B Chem*. **2017**,*250*(*2017*),601–7.

136. Mu H, Lin S, Wang Z, Xiao S, Li P, Chen Y, et al. Black Phosphorus-Polymer Composites for Pulsed Lasers. *Adv Opt Mater*. **2015**,*3*(*10*),1447–53.

137. Zhang B, Lou F, Zhao R, He J, Li J, Su X, et al. Exfoliated layers of black phosphorus as saturable absorber for ultrafast solid-state laser. *Opt Lett*. **2015**,*40*(*16*),3691–4.

138. Wang H, Yang X, Shao W, Chen S, Xie J, Zhang X, et al. Ultrathin black phosphorus nanosheets for efficient singlet oxygen generation Ultrathin black phosphorus nanosheets for efficient singlet oxygen generation. *J Am Chem Soc*. **2015**,*137*(*35*),11376–11382.

139. Yang J, Xu R, Pei J, Myint YW, Wang F, Wang Z, et al. Unambiguous identification of monolayer phosphorene by phase-shifting interferometry. *arXiv*. **2014**,1412.6701.

140. Nagahama T, Kobayashi M, Akahama Y, Endo S, Narita S. Optical Determination of Dielectric Constant in Black Phosphorus. *J Phys Soc Japan*. **1985**,*54*(*6*),1096–2099.

141. Stachel D, Svoboda I, Fuess H. Phosphorus Pentoxide at 233 K. *Acta Crystallogr Sect C Cryst Struct Commun*. **1995**,*51*(*6*),1049–50.

142. Keyes RW. The electrical properties of black phosphorus. *Phys Rev*. **1953**,*92*(*3*),580–4.

143. Zhang S, Yang J, Xu R, Wang F, Li W, Ghufran M, et al. Extraordinary photoluminescence and strong temperature/angle-dependent raman responses in few-layer phosphorene. *ACS Nano*. **2014**,*8*(*9*),9590–6.

144. Luo Z, Maassen J, Deng Y, Du Y, Garrelts RP, Lundstrom MS, et al. Anisotropic in-plane thermal conductivity observed in few-layer black phosphorus. *Nat Commun*. **2015**,*6*,1–8.

145. Widulle F, Ruf T, Konuma M, Silier I, Cardona M, Kriegseis W, et al. Isotope effects in elemental semiconductors: A Raman study of silicon. *Solid State Commun*. **2001**,*118*(*1*),1–22.

146. Hu W, Lin L, Zhang R, Yang C, Yang J. Highly Efficient Photocatalytic Water Splitting over Edge-Modified Phosphorene Nanoribbons. *J Am Chem Soc*. **2017**,*139*(*43*),15429–36.

147. Sofer Z, Bouša D, Luxa J, Mazanek V, Pumera M. Few-layer black phosphorus nanoparticles. *Chem Commun*. **2016**,*52*(*8*),1563–6.

148. Xiao KJ, Carvalho A, Castro Neto AH. Defects and oxidation resilience in InSe. *Phys Rev B*. **2017**,*96*(*5*),1–8.

149. Malyi OI, Sopiha K V., Draxl C, Persson C. Stability and electronic properties of phosphorene oxides: from 0-dimensional to amorphous 2-dimensional structures. *Nanoscale*. **2017**,*9*(*7*),2428–35.

150. Guo Y, Zhou S, Bai Y, Zhao J. Oxidation Resistance of Monolayer Group-IV Monochalcogenides. *ACS Appl Mater Interfaces*. **2017**,*9*(*13*),12013–20.

151. Wu S, He F, Xie G, Bian Z, Luo J, Wen S. Black Phosphorus: Degradation favors

lubrication. *Nano Lett*. **2018**,*18*(*9*),5618–27.

152. Han C, Hu Z, Carvalho A, Guo N, Zhang J, Hu F, et al. Oxygen induced strong mobility modulation in few-layer black phosphorus. *2D Mater*. **2017**,*4*(*2*),021007.

153. Nahas S, Ghosh B, Bhowmick S, Agarwal A. First-principles cluster expansion study of functionalization of black phosphorene via fluorination and oxidation. *arXiv*. **2015**,1–7.

154. Carvalho A, Castro Neto AH. Phosphorene: Overcoming the oxidation barrier. *ACS Cent Sci*. **2015**,*1*(*6*),289–91.

155. Utt KL, Rivero P, Mehboudi M, Harriss EO, Borunda MF, San Juan AAP, et al. Intrinsic defects, fluctuations of the local shape, and the photo-oxidation of black phosphorus. *ACS Cent Sci*. **2015**,*1*(*6*),320–7.

156. Kistanov AA, Cai Y, Zhou K, Dmitriev S V, Zhang Y-W. The role of H2O and O2 molecules and phosphorus vacancies in the structure instability of phosphorene. *2D Mater*. **2017**,*4*(*1*),015010.

157. Hu Z, Li Q, Lei B, Zhou Q, Xiang D, Lyu Z, et al. Water-Catalyzed Oxidation of Few-Layer Black Phosphorous in a Dark Environment. *Angew Chemie - Int Ed*. **2017**,*56*(*31*),9131–5.

158. Lü T-Y, Feng H, Zhang Y, Lu Y, Zheng J-C. Regulate the polarity of phosphorene's mechanical properties by oxidation. *Comput Mater Sci*. **2017**,*139*(*2017*),341–6.

159. Drissi LB, Sadki S, Sadki K. Half-oxidized phosphorene: band gap and elastic properties modulation. *J Phys Condens Matter*. **2016**,*28*(*14*),145501.

160. Lu W, Nan H, Hong J, Chen Y, Zhu C, Liang Z, et al. Plasma-assisted fabrication of monolayer phosphorene and its Raman characterization. *Nano Res*. **2014**,*7*(*6*),853–9.

161. Abellán G, Neiss C, Lloret V, Wild S, Chacón-Torres JC, Werbach K, et al. Exploring the Formation of Black Phosphorus Intercalation Compounds with Alkali Metals. *Angew Chemie - Int Ed*. **2017**,*56*(*48*),15267–73.

162. Ling Z-P, Zhu J-T, Liu X, Ang K-W. Interface Engineering for the Enhancement of Carrier Transport in Black Phosphorus Transistor with Ultra-Thin High-k Gate Dielectric. *Sci Rep*. **2016**,*6*,26609.

163. Galceran R, Gaufres E, Loiseau A, Piquemal-Banci M, Godel F, Vecchiola A, et al. Stabilizing ultra-thin black phosphorus with in-situ-grown 1 nm-Al2O3 barrier. *Appl Phys Lett*. **2017**,*243101*(*111*),1–5.

164. Gómez-Pérez J, Kónya Z, Kukovecz Á. Acetone improves the topographical homogeneity of liquid phase exfoliated few-layer black phosphorus flakes. *Nanotechnology*. **2018**,*29*(*365303*),0–15.

165. Wang X, Jones AM, Seyler KL, Tran V, Jia Y, Zhao H, et al. Highly anisotropic and

robust excitons in monolayer black phosphorus. *Nat Nanotechnol*. **2015**,*10*(*6*),517–21.

166. Brazhkin V V., Zerr AJ. Relative stability of red and black phosphorus at P < 1 GPa. *J Mater Sci*. **1992**,*27*,2677–81.

167. Daasch LW, Smith DC. Infrared Spectra of Phosphorus Compounds. *Anal Chem*. **1951**,*23*(*6*),853–68.

168. Wen-Bing Chang, Zhun-Zhi Jin, Xian-Wu Zou. Calculated infrared and Raman spectra of P2O5 glass. *Phys Lett A*. **1991**,*159*(*6–7*),361–4.

169. Gerding H, Decker HCJ DE. The Raman spectrum of phosphorus pentoxide. *Recl Trav Chim Pays-Bas*. **1945**,*64*(*7*).

170. Late DJ. Temperature Dependent Phonon Shifts in Few-Layer Black Phosphorus. *ACS Appl Mater Interfaces*. **2015**,*7*(*10*),5857–62.

171. Late DJ, Shirodkar SN, Waghmare U V., Dravid VP, Rao CNR. Thermal expansion, anharmonicity and temperature-dependent Raman spectra of single- and few-layer MoSe2 and WSe2. *ChemPhysChem*. **2014**,*15*(*8*),1592–8.

172. Gómez-Pérez J, Barna B, Tóth IY, Kónya Z, Kukovecz Á. Quantitative tracking of the oxidation of black phosphorus in the few- layers regime. *ACS Omega*. **2018**,*3*,12482–8.

173. Nakayama Y, Akita S, Shimada Y. Thermally Activated Electric Conduction in Carbon Nanotubes. *Jpn J Appl Phys*. **1995**,*34*(*2 (1A)*).

174. Asres GA, Dombovari A, Sipola T, Puskás R, Kukovecz A, Kónya Z, et al. A novel WS2 nanowire-nanoflake hybrid material synthesized from WO3 nanowires in sulfur vapor. *Sci Rep*. **2016**,*6*,25610.

175. Ovchinnikov D, Allain A, Huang YS, Dumcenco D, Kis A. Electrical transport properties of single-layer WS2. *ACS Nano*. **2014**,*8*(*8*),8174–81.

176. Yin H, Wang Y. Enhanced piezoelectricity of monolayer phosphorene oxides: a theoretical study. *Phys Chem Chem Phys*. **2017**,*19*,26–8.

177. Freitag M, Steiner M, Martin Y, Perebeinos V, Chen Z, Tsang JC, et al. Energy dissipation in graphene field-effect transistors. *Nano Lett*. **2009**,*9*(*5*),1883–8.